# Theory and Modelling of Electron Transport in Molecular-Scale Condensed Matter

Bashayr Khalaf Alanazi

Ph.D. Thesis in Physics

Department of Physics, Lancaster University, UK


2023

This Thesis is submitted in partial fulfillment of the requirements for the degree of Doctor of Philosophy

# Declaration

I hereby declare that the thesis is my own work and effort and has not been submitted in substantially the same form for the award of a higher degree elsewhere. Other sources of information have been used, and they have been acknowledged. This thesis documents work carried out between June 2020 and July 2023 at Lancaster University, UK, under the supervision of Prof. Colin J. Lambert and funded by the Ministry of Higher Education Saudi Arabia and Northern Border University, KSA.

*Bashayr Alanazi*

*2023*

## Acknowledgment

My great thanks to ALLAH for his mercy and blessing. I could not have achieved what I have done without ALLAH.

I would like to express my deepest gratitude to Prof. Colin John Lambert for his support, kindness, and his patience. Also, I am truly grateful for his tutorials, which provide me with a deep understanding of molecular electronics and would be really helpful for my future study and research.

I would also like to express my grateful admiration to Dr. Ali Ismael for his encouragement, and valuable guidance, insightful comments and suggestions, dedicated time through my PhD Journey. Also, many thanks to the Theory of molecular-Scale groups and the collaborating experimental groups. I would like to thank all my friends and colleagues in Colin's group.

Many thanks also go to the support I received during my PhD from the Ministry of higher education in Saudi Arabia and Northern Border University.

I owe thanks to my beloved parents who supported me all the way to pursue my dream. Also, I would like to express a deep sense of gratitude to my husband (Abdelrahman) for his patience, tolerance, care, and love for me. I am also grateful to my daughters (Hajar and Nibras). My gratitude to them is beyond words.

Finally, warm thanks go to my sisters and brothers and all members of my family for all of the love, support, encouragement, and prayers they have sent my way along this journey.

# Abstract

For nano- and molecular-scale applications, it is crucial to investigate and fully understand the electron transport properties of molecular junctions made up of a scattering region like a molecule coupled to metallic electrodes. The electrical properties of two different kinds of two terminal junctions are presented in the theoretical work contained in this thesis: one deals with gold electrodes, which form gold-molecule-gold structures and the other has single-layer graphene forming a gold-molecule-single-layer-graphene junction. In this thesis, the above investigations into the electrical and thermoelectric properties of molecular junctions utilize the theoretical techniques covered in chapters 2 and 3. Chapter 2 presents an introduction to the density functional theory (DFT). It is followed by an outline of transport theory in Chapter 3, based on Green's function formalism. Chapter4 represents a study of the electron transport properties of the single-molecule/bilayer molecular junctions, formed from Zinc Tetraphenyl Porphyrin (ZnTPP), small graphene-like molecules (Gr), three derivatives with pyridine backbones, and three alkyl-chain backbones terminated with asymmetric anchor groups: amine ($NH_2$ ), and a direct carbon ($CH_2$ ) bond. Chapter5 studied the same core molecules, junctions with asymmetric electrodes which are gold and a single-layer graphene sheet (SLG).

# List of Publications

1. 1. Wang, X., Ismael, A., **Alanazi, B**., Al-Jobory, A., Wang, J., & Lambert, C. J. (2023). High seebeck coefficient from isolated oligo-phenyl arrays on single layered graphene via stepwise assembly. Journal of Materials Chemistry C

2. **Alanazi, B**., Alajmi, A., Aljobory, A., Lambert, C., & Ismael, A. (2024). Tuning quantum interference through molecular junctions formed from cross-linked OPE-3 dimers. Journal of Materials Chemistry C

# Table of contents

# List of Figures

# List of Tables

# List of abbreviations

| | |
|---|---|
| ME | Molecular electronics |
| DFT | Density Functional Theory |
| LDA | Local Density Approximation |
| GGA | Generalized Gradient Approximation |
| SCF | Self-Consistent Field |
| vdW | Van der Waals |
| DZ | Double-ξ basis set |
| DZP | Double- ξ polarized basis set |
| SIESTA | Spanish Initiative for Electronic Simulations with Thousands of Atoms |
| LCAOB | Linear Combination of Atomic Orbital Basis |
| BSSE | Basis set superposition error |
| CP | Counterpoise correction |
| T(E) | Transmission coefficient |
| G(E) | Electrical conductance |
| S | Seebeck coefficient |
| STM | Scanning Tunnelling Microscopy |
| MCBJ | mechanically controlled break junction |
| EBJ | electromigration break junction |
| SAM | Self-Assembled Monolayer |
| SLG | single-layer graphene |

| | |
|---|---|
| ZnTPP | Zinc Tetraphenyl Porphyrin |
| HOMO | Highest Occupied Molecular Orbital |
| LUMO | Lowest Occupied Molecular Orbital |
| EGaIn | Gallium Indium alloy (EGaIn) |

# Chapter 1

## 1.1 Molecular Electronics and Thermopower

In 1965, Gordon Moore predicted a historical trend that states the size of electronic components like semiconductors decrease exponentially over time. Numerous studies have been undertaken to find methods to keep up with this historical pattern and are now getting close to the nano- or molecular scale [1]. Molecular electronics (ME) is known as the field of science that studies the electrical and thermal transport characteristics of circuits that use single molecules (or groups of them) as their fundamental building blocks [2]. Nanoscale electronic devices have numerous potential applications such as transistors [3-4], rectifiers [5-6], sensors [7-8], and switches [9]. The concept behind single-molecule electronics is building and designing molecules to create more complicated structures, active components, and connecting wires. Due to its potential for sub-10nm electronic switches and rectifiers and its capacity to offer sensitive platforms for single-molecule detection, molecular electronics has a lot of potential uses in nanoscale electronics [10]. A further appealing feature is a possibility for nanoscale self-assembly to use intermolecular interactions, which could lead to low-cost production. In addition, the diversity of molecular structures that can be created by chemists allows for the logical and methodical modification of a variety of molecular characteristics. Additionally, molecular junctions are excellent research platforms for determining the basic principles of electron transport processes [11-12]. In 1974, Aviram and Ratner made the first hypothesis with the molecular current rectifier, while Polymeropoulos and Sagiv studied molecular-based tunnel junctions (resistors) 30 years earlier [13]. Aviram and Ratner proposed a single molecule with sections for electron donors and acceptors as a typical example and placed it between two metal conductors. They showed that in electronic devices, a molecule linked to the electrodes either serves as an electrical current conduit or controls the electrodes' charge transport

characteristics [14]. Binnig and Heinrich Rohrer in the 1980s invented the scanning tunneling microscope (STM) based on a phenomenon in quantum mechanics called tunnelling. In 1990, a group of researchers manipulated STM techniques whereas can be obtained the atomic and molecular properties. [15-16]. These methods have been used and developed for a simple electrode-molecule-electrode system, contacting single molecules, graphene-based junctions [17], and silicone-based junctions [18]. In the past few decades, improvements in nanofabrication techniques and the quantum theory of electronic transport have made it possible to investigate and comprehend the core features of electrical circuits, in which molecules are used as fundamental components to study their electronic transport properties [19-20-21].

It is important to remember that developing single-molecule devices is not simple due to some difficulties and restrictions. A number of challenges that single-molecule electrical systems have to face are summed up as follows:

- Because of the molecule's small size, it is frequently difficult to directly manipulate the molecule into the nanogap. Instead, a molecule cannot be positioned in the gap between electrodes without molecular interaction between it and the electrode.
- It is more difficult to make sure that only one molecule is put inside each functional device because electrodes can often be significantly larger than the molecules.
- stability, uniformity, and scalability are other challenges.

Despite these difficulties and restrictions on theory and experiments, molecular electronics has made significant progress, offering a useful road plan for future electronics uses. This thesis discusses the basic ideas in the non-equilibrium Green's function formalism of transport theory, which is implemented in the Gollum code [22], and the density functional theory (DFT), which is implemented in the SIESTA code [23], in order to describe the fundamental properties of molecular junctions at the nanoscale. Furthermore, a lot of progress has been made in the

understanding of the thermoelectrical characteristics of single-molecule junctions [24], which was made possible by findings such as high Seebeck coefficients of order 161 for PEDOT: PSS organic films [25]. I investigate the essential features of enhancing the thermopower properties of molecular junctions. I will investigate the multicomponent graphene substrate via non-covalent interaction have demonstrated higher thermoelectric behavior. I will present a multi-component technique to create an aromatic molecular array on a graphene substrate. This technique split molecular backbones by big ZnTPP footprint, and it has demonstrated effective thermopower with a Seebeck value up to 51 uV/K. Also, it shall combine the links between theory and experimentation to produce and model (STM) devices.

**Porphyrin**

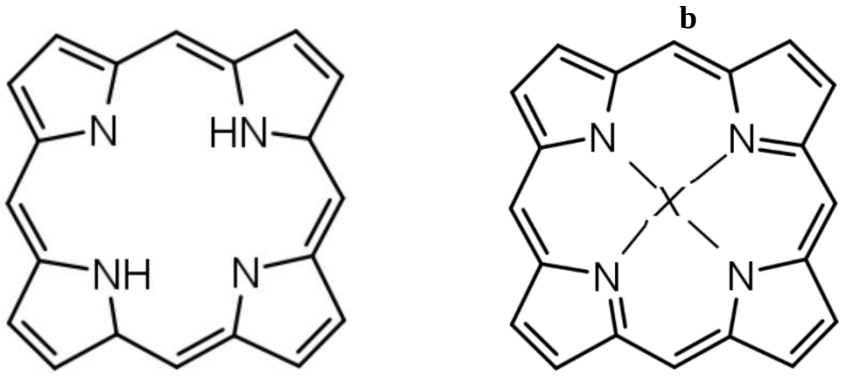


**Figure 1:** (**a** and **b**) illustrate the chemical structure of a metal-free porphyrin and metallo-porphyrin molecules, respectively. X is the incorporated metal

Porphyrins are an interesting class of organic compounds, which are desirable as molecular-scale device building blocks, because they are conjugated, rigid, chemically stable, and coordinate a variety of metallic ions to produce metallo-porphyrins [26-27]. The

metallo-porphyrin molecule has four pyrrole units with a metallic atom in the middle, as illustrated in Figure 1.1, whereas the porphyrin molecule has four pyrrole units (the inner ring

-system). Wires, switches, transistors, and photodiodes can all be made from porphyrin derivatives. [28-29].

The metal ions can be Zn, Fe, Ni, and Co [30-31]. In nature, metallo-porphyrins present in hemoglobin, myoglobin, chlorophyll, cytochromes, catalase, and peroxidases serve a number of significant biochemical functions [32]. Research on these compounds is not limited to the biological area, but also these substances are equally significant from a chemical, industrial, and technical point of view. Synthetic porphyrins have been extensively explored over the past three decades for a variety of uses in a wide range of chemical and biological fields [33].

## 1.2 Thesis Outline

This thesis will present theoretical simulations of nanoscale electron transport and molecular electronics. Chapter 2 gives a brief summary of one of the fundamental theoretical methods employed in this thesis density functional theory (DFT) to study and understand the electronic properties of single-molecule junctions. The single-particle transport theory is described in Chapter 3. This chapter covers the Landauer formula, Green's functions for various transport regimes based on scattering theory, and some examples of how to compute the transmission coefficient for various systems using the Hamiltonian and Green's functions.

After providing the fundamental background of nanoscale transport modelling techniques, I will describe theoretical studies of selected molecular junctions. In this work, I have two devoted chapters to investigate the electrical and thermal properties of the studied molecules. Chapter 4 focusses on the transport properties in gold- molecule-gold junctions, whereas chapter 5 studies the transport properties in gold-molecule- single-layer graphene (SLG) junctions. Chapter 6 presents some conclusions and suggestions for future work.

## 1.3 Bibliography


1. Leon, S. J., Bica, I. & Hohn, T. (1998). Linear algebra with applications (Vol. 6). Upper Saddle River, NJ: Prentice Hall
2. Cuevas, J. C., & Scheer, E. (2010). Molecular electronics. World Scientific Series in Nanoscience and Nanotechnology. doi:10.1142/7434
3. Martel, R., Schmidt, T., Shea, H. R., Hertel, T., & Avouris, Ph. (1998). Single- and multi-wall carbon nanotube field-effect transistors. Applied Physics Letters, 73(17), 2447–2449. doi:10.1063/1.122477
4. Perrin, M. L., Burzurí, E., & van der Zant, H. S. (2015). Single-Molecule Transistors. Chemical Society Reviews, 44(4), 902–919. doi:10.1039/c4cs00231h
5. Saha, M., & Maiti, S. K. (2017). High degree of current rectification at Nanoscale Level. Physica E: Low-Dimensional Systems and Nanostructures, 93, 275–278. doi:10.1016/j.physe.2017.06.023
6. Batra, A., Darancet, P., Chen, Q., Meisner, J. S., Widawsky, J. R., Neaton, J. B., … Venkataraman, L. (2013). Tuning rectification in single-molecular diodes. Nano Letters, 13(12), 6233–6237. doi:10.1021/nl403698m
7. Sadeghi, H., Bailey, S., & Lambert, C. J. (2014). Silicene-based DNA nucleobase sensing. Applied Physics Letters, 104(10). doi:10.1063/1.4868123
8. Sadeghi, H., Algaragholy, L., Pope, T., Bailey, S., Visontai, D., Manrique, D., … Lambert, C. J. (2014). Graphene sculpturene nanopores for DNA nucleobase sensing. The Journal of Physical Chemistry B, 118(24), 6908–6914. doi:10.1021/jp5034917
9. Jan van der Molen, S., & Liljeroth, P. (2010). Charge transport through molecular switches. Journal of Physics: Condensed Matter, 22(13), 133001. doi:10.1088/0953-8984/22/13/133001

10. Wilkinson, L. A., Bennett, T. L., Grace, I. M., Hamill, J., Wang, X., Au-Yong, S., … Long, N. J. (2022). Assembly, structure and thermoelectric properties of 1,1′-dialkynylferrocene ‘hinges.’ Chemical Science, 13(28), 8380–8387. doi:10.1039/d2sc00861k
11. Finch, C. M., Sirichantaropass, S., Bailey, S. W., Grace, I. M., García-Suárez, V. M., & Lambert, C. J. (2007). Conformation dependence of molecular conductance: Chemistry versus geometry. Journal of Physics: Condensed Matter, 20(2), 022203. doi:10.1088/0953-8984/20/02/022203
12. Ismael, A., Al-Jobory, A., Wang, X., Alshehab, A., Almutlg, A., Alshammari, M., … Lambert, C. (2020). Molecular-scale thermoelectricity: As simple as ‘ABC.’ *Nanoscale Advances*, *2*(11), 5329–5334. doi:10.1039/d0na00772b
13. Bovensiepen, U., Biermann, S., & Perfetti, L. (2012). The electronic structure of Solids. Dynamics at Solid State Surfaces and Interfaces, 1–25. doi:10.1002/9783527646463.ch1
14. Jayamurugan, G., Gowri, V., Hernández, D., Martin, S., González-Orive, A., Dengiz, C., Diederich, F. (2016). Design and synthesis of Aviram–Ratner-Type Dyads and rectification studies in Langmuir–Blodgett (lb) films. Chemistry – A European Journal, 22(30), 10539–10547. doi:10.1002/chem.201505216
15. Giessibl, F. J. (2003). Advances in atomic force microscopy. Reviews of Modern Physics, 75(3), 949–983. doi:10.1103/revmodphys.75.949
16. Zhang, J. L., Zhong, J. Q., Lin, J. D., Hu, W. P., Wu, K., Xu, G. Q., … Chen, W. (2015). Towards single molecule switches. Chemical Society Reviews, 44(10), 2998–3022. doi:10.1039/c4cs00377b

17. Sadeghi, H., Sangtarash, S., & Lambert, C. J. (2015). Enhancing the thermoelectric figure of merit in engineered graphene nanoribbons. Beilstein Journal of Nanotechnology, 6, 1176–1182. doi:10.3762/bjnano.6.119

18. Sadeghi, H., Bailey, S., & Lambert, C. J. (2014a). Silicene-based DNA nucleobase sensing. Applied Physics Letters, 104(10). doi:10.1063/1.4868123

19. Gonzalez, G. (2009). Electron transport in single molecule magnet transistors and optical transitions in the 15nitrogen-vacancy-center in diamond. University of Central Florida.

20. Wang, X., Ismael, A., Ning, S., Althobaiti, H., Al-Jobory, A., Girovsky, J., … Ford, C. J. (2022). Electrostatic Fermi level tuning in large-scale self-assembled monolayers of oligo(phenylene–ethynylene) derivatives. Nanoscale Horizons, 7(10), 1201–1209. doi:10.1039/d2nh00241h

21. Afsari, S., Li, Z., & Borguet, E. (2014). Orientation-controlled single-molecule junctions. Angewandte Chemie International Edition, 53(37), 9771–9774. doi:10.1002/anie.201402343

22. Soler, J. M., Artacho, E., Gale, J. D., García, A., Junquera, J., Ordejón, P., & Sánchez-Portal, D. (2002). The siesta method forab initioorder-nmaterials simulation. Journal of Physics: Condensed Matter, 14(11), 2745–2779. doi:10.1088/0953-8984/14/11/302

23. Ferrer, J., Lambert, C. J., García-Suárez, V. M., Manrique, D. Z., Visontai, D., Oroszlany, L., … Algharagholy, L. A. (2014). Gollum: A next-generation simulation tool for electron, thermal and Spin Transport. New Journal of Physics, 16(9), 093029. doi:10.1088/1367-2630/16/9/093029

24. Massonnet, N., Carella, A., Jaudouin, O., Rannou, P., Laval, G., Celle, C., & Simonato, J.-P. (2014). Improvement of the Seebeck coefficient of PEDOT:PSS by chemical reduction combined with a novel method for its transfer using free-standing thin films. J. Mater. Chem. C, 2(7), 1278–1283. doi:10.1039/c3tc31674b

25. Rincón-García, L., Ismael, A. K., Evangeli, C., Grace, I., Rubio-Bollinger, G., Porfyrakis, K., and Lambert, C. J. (2016). Molecular design and control of fullerenebased bi-thermoelectric materials. Nature materials, 15(3), 289-293.

26. Auwärter, W., Écija, D., Klappenberger, F., & Barth, J. V. (2015). Porphyrins at interfaces. Nature Chemistry, 7(2), 105–120. doi:10.1038/nchem.2159

27. Jurow, M., Schuckman, A. E., Batteas, J. D., & Drain, C. M. (2010). Porphyrins as molecular electronic components of functional devices. Coordination Chemistry Reviews, 254(19–20), 2297–2310. doi:10.1016/j.ccr.2010.05.014

28. Sedghi, G., Sawada, K., Esdaile, L. J., Hoffmann, M., Anderson, H. L., Bethell, D., … Nichols, R. J. (2008). Single Molecule conductance of porphyrin wires with Ultralow attenuation. Journal of the American Chemical Society, 130(27), 8582–8583. doi:10.1021/ja802281c

29. Cho, S., Yoon, M.-C., Kim, K. S., Kim, P., & Kim, D. (2011). Electron delocalization in various triply linked zinc(ii) porphyrin arrays: Role of antiaromatic junctions between aromatic porphyrins. Physical Chemistry Chemical Physics, 13(36), 16175. doi:10.1039/c1cp21737b

30. Hoard, J. L. (1971). Stereochemistry of hemes and other Metalloporphyrins. Science, 174(4016), 1295–1302. doi:10.1126/science.174.4016.1295

31. Noori, M., Sadeghi, H., Al-Galiby, Q., Bailey, S. W., & Lambert, C. J. (2017). High cross-plane thermoelectric performance of metallo-porphyrin molecular junctions. Physical Chemistry Chemical Physics, 19(26), 17356–17359. doi:10.1039/c7cp02229h

32. Smith, E. L. (1983). Principles of Biochemistry: General Aspects; McGraw-Hill; Vol. 1.

33. Mukundan, N. E., Petho, G., Dixon, D. W., & Marzilli, L. G. (1995). DNA-tentacle porphyrin interactions: At over GC selectivity exhibited by an outside binding self-stacking porphyrin. Inorganic Chemistry, 34(14), 3677–3687. doi:10.1021/ic00118a015

# Chapter2

**Density Functional Theory (DFT)**

The mathematical principles of DFT and the general concepts are employed in all the electronics structure's calculations in this thesis. To predict electron transport properties of a molecular junction, I first extract the Hamiltonian of the isolated molecule and then link this isolated molecule to electrodes to calculate the transport properties of molecular junctions, as discussed in the following section.

## 2.1 Introduction

Density functional theory is a successful method to calculate electronic properties in various interaction structures, such as atoms, molecules, and crystal. For more than 30 years theoretical condensed matter physicists have used it widely. More recently, theoretical, and computational chemists have started to use it frequently [1-2]. The fundamental goal of density functional theory is to explain an interacting many-particle system in terms of its density. The history of the DFT began in 1920s, where Llewellyn Thomas and Enrico Fermi established the fundamental steps to achieve the density functionals for total energy using the wave function [1-3-4]. Dirac, Hartree, Slater, and Fock added additional improvements for Thomas's work. Modern DFT is based on the Hohenberg-Kohn Theorem (1964) and the Kohn-Sham formulation. [3-4]. which calculates the ground state of organic molecules [1-6]. This introductory section provides a brief overview of the basic concepts of density functional theory. It begins with Schrödinger equation of a many-body system in three-dimensional space. It is then followed by the Born-Oppenheimer approximation of the nuclei, and the Hohenberg-Kohn theorem, and then expands to the Kohn-Sham theorem, which has become a powerful and reliable approach to describing ground state properties of a quantum system. In addition, an implementation of DFT SIESTA code (Spanish Initiative for Electronic Simulations with

Thousands of Atoms) [7] has been introduced which is used as a theoretical tool to perform calculations on molecular systems which are the subject of this research work.

**2.2 The Schrödinger Equation and Variational Principle**

Any many -body systems can be described by non-relativistic Schrödinger equation.

$$H\,\psi_i(\vec{r}_1, \vec{r}_2, \ldots, \vec{r}_N, \vec{R}_1, \vec{R}_2, \ldots\ldots, \vec{R}_M) = E_i\psi_i(\vec{r}_1, \vec{r}_2, \ldots, \vec{r}_N, \vec{R}_1, \vec{R}_2, \ldots\ldots, \vec{R}_M) \qquad (2.1)$$

where $\psi_i$ is the wavefunction of the state of the system and $E_i$ is the numerical value of the energy of the $i^{th}$ represented by $\psi_i$. H represents the Hamiltonian operator of a system consisting of N-electrons and M-nuclei that contains the interaction of particles with each other. Generally, the Hamiltonian operator (H) is written as:

$$H = -\frac{\hbar^2}{2m_e}\sum_i \nabla_i^2 - \frac{\hbar^2}{2m_I}\sum_I \nabla_I^2 + \frac{1}{8\pi\varepsilon_o}\sum_{i\neq j}\frac{e^2}{|r_i - r_j|} + \frac{1}{8\pi\varepsilon_o}\sum_{I\neq J}\frac{z_I z_J e^2}{|R_I - R_J|} - \frac{1}{4\pi\varepsilon_o}\sum_{iI}\frac{z_I e^2}{|r_i - R_I|} \qquad (2.2)$$

The Hamiltonian of the many-body system is divided into five terms: the first two terms represent the kinetic energy of electrons and nuclei respectively. Additionally, the last three terms are the potential energy of electron and nuclei, which defines the attractive electrostatic interaction between electrons and nuclei in the system. Here, $m_e$ and $m_I$ are the mass of electron and nucleus, respectively, $r_i$ and $R_I$ represent the position of electrons and nuclei, respectively,e and $z_I$ denote the electron and nuclear charge, and $i$ and $j$ represent the *N*-electrons while $I$ and $J$ represent a run over the *M*-nuclei in the system. However, the Schrodinger equation cannot be solved for many-body systems with a huge number of electrons thus, some approximations are employed to solve this issue such as those introduced by Max Born and J.Rober Oppenheimer in 1927 [8].

### 2.3 Born- Oppenheimer Approximation

The Born-Oppenheimer approximation is an approach typically used to reduce the problem of the Schrödinger equation (2.1), which cannot be solved for more than a few electrons. Because the mass of the nucleons is bigger than the electron mass [9-10] which lead significantly lower their velocities of motion, the kinetic energy of nuclei is neglected, and they are considered as a classical particle, which creates a fixed external potential. Therefore, we treat the electrons as quantum particles subject to this potential, with the assumption that the nucleon wavefunction is independent of the electron position. The electron degrees of freedom are obtained from this solution of the Schrödinger equation. Therefore, the Hamiltonian for the electron can be written as:

$$H = T_e + V_e + \sum_i V_{ext}(r_i) \tag{2.3}$$

where, $T_e = -\frac{\hbar^2}{2m_e}\sum_i \nabla_i^2$ which is the kinetic energy of all electrons, $V_e = \frac{1}{8\pi\varepsilon_o}\sum_{i\neq j}\frac{e^2}{|r_i - r_j|}$ that represents the interaction between electrons ,and $V_{ext}$ is s the external potential due to nuclei and electron interaction, in addition to any external field.

Then the Schrödinger Equation can be written as:

$$H\,\psi_i(\vec{r}_1, \vec{r}_2, \dots, \vec{r}_i..) = E_i\psi_i(\vec{r}_1, \vec{r}_2, \dots, \vec{r}_i..) \tag{2.4}$$

Even though this approximation has reduced the system's size, it is still challenging to solve the Schrodinger equation. Thus, density functional theory can resolve this issue by determining the physical quantities in terms of the ground-state density $\rho_o(\vec{r})$ [11]. The first approach would be the Hohenberg-Kohn theorem.

## 2.4 The Hohenberg- Kohn Theorem

The Hohenberg-Kohn theorem was discovered in 1964 [12]. It' is a backbone of DFT due to its capacity to determine properties of the ground-state density $\rho(\vec{r}\vec{\rightarrow})$ system. This can be used in many-electron system that interacts with an applied external potential V (r) and it corresponds to a minimum total energy functional where the density of the electron is considered as a ground state of the system. The HK theorem can best be proved using two powerful statements.

1: For any interacting systems in external potential $V_{ext}(\vec{r})$, This potential is only determined by the ground-state density [13-16].

2: The total energy of the system is minimized to the correct ground-state energy, which is a function of the electron density in the ground state.

The first theorem can be proved by assuming two different external potentials$V_{ext}(\vec{r})$) that have the same ground state density. These potentials have two distinct Hamiltonian s as well as different wave functions. Therefore, we have

$$\hat{H}_1\,\psi_1 = E_1\,\psi_1$$

$$\hat{H}_2\,\psi_2 = E_2\,\psi_2$$

where $\psi_2$ is not the ground state wavefunction of $\hat{H}_1$

$$E_1 = \langle\psi_1|\hat{H}_1|\psi_1\rangle < \langle\psi_2|\hat{H}_1|\psi_2\rangle \tag{2.5}$$

and similarly:

$$E_2 = \langle\psi_2|\hat{H}_2|\psi_2\rangle < \langle\psi_1|\hat{H}_2|\psi_1\rangle \tag{2.6}$$

Assuming non-degenerate [17-18] ground states, we can rewrite the equation (2.6)

$$\langle\psi_2|\hat{H}_1|\psi_2\rangle = \langle\psi_2|\hat{H}_2|\psi_2\rangle + \langle\psi_2|\hat{H}_1\text{-}\hat{H}_2|\psi_2\rangle$$

$$= E_2 + \langle\psi_2|V_1(\vec{r})\text{-}V_2(\vec{r})|\psi_2\rangle$$

$$= E_2 + \int dr\,[V_1(\vec{r})\text{-}V_2(\vec{r})]\,\rho_o(r) \quad (2.7)$$

Additionally, assuming that $|\psi_1\rangle$ has the same density $\rho_o(r)$ as $|\psi_2\rangle$

$$\langle\psi_1|\hat{H}_2|\psi_1\rangle = E_1 + \int dr\,[V_2(\vec{r})\text{-}V_1(\vec{r})]\,\rho_o(r) \quad (2.8)$$

Adding together the two equations (2.7) and (2.8) guide to a contradiction

$$E_1 + E_2 < E_1 + E_2 \quad (2.9)$$

Thus, it follows that the two differing external potentials cannot yield the same ground state density.

The second theorem is proved by minimization of the ground state functional which can be written as

$$E[\rho] = T[\rho] + E_{int}[\rho] + \int dr\,V_{ext}(r)\,\rho(r) \quad (2.10)$$

The kinetic term T and internal interaction of the electrons $E_{int}$ are rely on the charge density. Therefore, the exact ground state density $\rho_o(r)$is the density $\rho(r)$ that minimizes the functional.

**2.5 The Kohn-Sham Theorem**

HK theorems present the ground state density by calculating the ground state energy. However, the kinetic energy term, and the internal energy of the interacting particles which is the exact form of the functional shown in Eq. 2.10 is not known and generally cannot be expressed as a functional of the density.

In 1965 Kohn and Sham [19] has explored the solution by generating the same ground-state density for any given system of interacting particles as a self-consistent method [19-20]. According to Kohn and Sham, one can replace the original Hamiltonian of the system with an effective Hamiltonian of the non-interacting system in an effective external potential which same ground state density as the initial system. It is considered as an ansatz while there is no

obvious mechanism for doing the calculations, but it is not difficult to solve the non-interacting problem. the form of the ground state functional of the Kohn -Sham ansatz can be as:

$$E_{KS}\ (\rho) = T_{KS}\ (\rho) + \int dr\ V_{ext}\ (r)\ \rho(r) + E_H\ (\rho) + E_{xc}\ (\rho) \tag{2.11}$$

The terms for this equation are listed below.

$T_{ks}$ is the kinetic energy of the non-interacting system while T in Eq.2.10 is

the kinetic energy for the interacting system.

Additionally, the electron-electron interaction is represented by the Hartree functional, $E_H$ which has the following form using the Hatree-Fock method:

$$E_H\ [\rho(r)] = \frac{1}{2} \int \frac{\rho(r)\ \rho(\acute{r})}{|r\text{-}\acute{r}|}\ dr\ d\acute{r} \tag{2.12}$$

$E_{xc}$ exchange correlation functional which is referred to the differences between the exact and approximated solutions to both the kinetic energy term and the electron-electron interaction term it's defined:

$$E_{xc}\ [\rho(r)] = (E_{int}\ (\rho)\text{-}E_H\ (\rho)) + (\ T\ (\rho)\text{-}T_{KS}\ (\rho)) \tag{2.13}$$

A single particle Hamiltonian can be given by the effective single particle potential $V_{eff}$which is described by taking the functional derivatives of the last three terms of equation (2.11) as:

$$V_{eff}\ (r) = V_{ext}\ (r) + \frac{\partial}{\partial \rho}\ (E_H\ [\rho(r)] + E_{xc}\ [\rho(r)]) \tag{2.14}$$

Thus, the Hamiltonian can be written as:

$$H_{KS}\ = T_{ks}[\rho] + V_{eff} \tag{2.15}$$

Then, Kohn-Sham equation can be introduced by applying the single Hamiltonian which is given by:

$$H_{KS}\ \psi^{KS}\ = E\ \psi^{KS} \tag{2.16}$$

## 2.6 The Exchange Correlation Functional

In the literature, several modifications to the exchange and correlation energy have been reported. One of the most used approximations in density functional theory are LDA and GGA. The simplest form that depends on the density is a local functional lead to the Local Density Approximation (LDA) [21-22]. A more complex form that includes also the derivative of the density semi-local and known as the Generalized Gradient Approximation (GGA) [23-24].

The Local Density Approximation and the Generalized Gradient Approximation will each be discussed briefly in the following sections.

### 2.6.1 Local Density Approximation

The Local Density Approximation (LDA) is one of the first and simplest approximation which depends on the local density. For systems where the local density is generally smooth, this approximation is expected to produce good results. It is known to be accurate for graphene and carbon nanotubes as well as other materials where the electron density is not changing quickly. Also, it does not work for systems with which they are largely dominated by electron-electron interactions. LDA is a simple but effective functional for many systems.

### 2.6.2 Generalized Gradient Approximation

Since the electron density changes rapidly at point in a real inhomogeneous system, the LDA approximation is invalid for heavier atoms. Thus, it is necessary finding a different approximation that more accurately for the gradient of the electron density which is generalized gradient approximation GGA.

The GGA expands LDA by involving the density derivatives into the functional form of the exchange and correlation energies [25-26]. Even though the GGA approximation has a lack of a closed form for the exchange term of the functional it has been estimated along with the correlation contribution using numerical techniques.

## 2.7 SIESTA

SIESTA (The Spanish Initiative for Electronic Simulations with Thousands of Atoms) is a DFT-based computer tool to perform electronic structure calculations and molecular dynamics simulations of molecules and solids [27]. The DFT implementation in the SIESTA code, which is used to demonstrate the electronic characteristics of the relaxed structures, was used for all calculations provided in this thesis. It is made to carry out effective computations on massive systems made up of thousands of atoms.

### 2.7.1 The Pseudopotential Approximation

As was pointed out in the previous section, the Kohn-Sham approach simplifyies the many bodies interacting problem to a huge effective non-interacting problem. However, complicated, and massive calculations occur with a numerous number of atoms that involved in the system therefore, pseudopotentials have been introduced by Fermi in 1934 [28-29] to reduce the number of the core electrons in atoms. This method has evolved from creating not so realistic empirical pseudopotentials [30-31] to more realistic ab-initio pseudopotentials [32-33]. This approximate concept assumes that there are two different types of electrons in atoms, namely core and valence electrons, where core electrons exist in filled atomic shells and valence electrons existing in partially filled shells. When atoms are brought together, only valence electrons contribute to the formation of molecular orbitals due to the spatial localization of core electrons around the nucleus as well as the overlapping of the electronic states. As a result, pseudopotentials have been employed by replacing the electron's core, while maintaining the valence electrons still feel the same screened nucleon charge as if the core electrons were still present. Thus, the total number of electrons in a system is substantially decreased, which minimizes the time and memory that needs for computing the properties of molecules with many electrons.

### 2.7.2 Basis Sets

Basis sets are an important ingredient that SIESTA uses in the calculations. It is necessary to diagonalize the Hamiltonian in order to determine the wavefunctions. Generally, this process involves the inversion of a large matrix whose computational time increases as the number of non-zero elements increase. For this reason, it is crucial that the Hamiltonian be sparse with a large number of zeros to allow efficient calculations. SIESTA uses a linear combination of atomic orbitals (LCAOs) basis set, which are bound to be zero after some defined cut-off radius and are computed using the atom's orbitals [34-35]. It follows that the form of the Hamiltonian is generated sparingly when the overlap of the basic functions decreases. Therefore, a minimum-sized basis set can generate properties that are close to those of the studied systems. The numerical radial and a spherical harmonic are used as a component in the construction of the basis functions. which is followed by:

$$\psi_{nlm}(r) = \phi^{1}_{nl}(r)\, Y_{lm}(\varphi, \vartheta) \tag{2.16}$$

where $\phi^{1}_{nl}(r)$ is the radial wavefunction and, $Y_{lm}(\varphi, \vartheta)$ is a spherical harmonic wavefunction. Also, l is the orbital angular momentum, m is the magnetic quantum number, and n indicates that the same angular momentum numbers might have many orbitals. However, the simplest form of the atomic basis set for an atom is the single - ζ which correspond to one basis function, per electron orbital. Another type of basis set which considered as a high accuracy basis set is multipl- ζ so that can be represented by adding another radial wavefunctions for each atomic orbital. Further accuracy ((multiple- ζ polarised) can be obtained by including wavefunctions with different angular momenta corresponding to orbitals which are unoccupied in the atom [36].

### 2.7.3 Binding Energy Using the Counterpoise Method

As mentioned above, the ground-state energy for different system configurations is calculated utilizing the DFT approach, which is also used to calculate the binding energy between different parts of a system. However, performing such these calculations would not yield an accurate result, due to the localized nature of the LCOA basis sets, which are centered on the nuclei. When atoms are sufficiently close to each other, their basis functions are going to overlap. This effect, which is called the basis set superposition error (BSSE), increases as the atoms orientate themselves closer, thereby creating an effectively varying basis set against the interatomic distance.

One obvious solution to the BSSE is the use of extremely large basis sets. This is, however, hardly feasible for the of the chemically interesting systems. The second approach is termed the counterpoise correction (CP), which is an approximate method proposed by Boys and Bernardi [37]. Assuming two molecular systems are denoted **A** and **B,** the energy of the interaction can be expressed as:

$$\Delta E(AB) = E^{AB}\text{-}(E^{A} + E^{B}) \tag{2.17}$$

where $E^{AB}$ is the total energy for the dimer systems A and B, $E^{A}$ and $E^{B}$ are the energies of the isolated systems A and B. It is worth mentioning that to execute this correction in SIESTA, the ghost states (i.e., no nuclei and no electrons but empty basis set functions centered on them) have been used to evaluate the total energy of segregated systems A or B in dimer basis, with keeping the identical basis sets for three energies [38-39].

$$\Delta E(AB) = E_{AB}^{AB}\text{-}(E_{A}^{AB} + E_{B}^{AB}) \tag{2.18}$$

where the superscript AB means the whole basis set is used, and the subscripts denote the geometry. $E_{A}^{AB}$ and $E_{B}^{AB}$ are the energies of systems A and B are evaluated in the basis of the dimer. This approach is an important method to eliminate the BSSE and provide reliable and realistic results for different systems [40].

## 2.8 Conclusion

The underlying concepts of density functional theory has been illustrated in this chapter. beginning with the Schrodinger equation, followed by the Hobenberg-Kohn theorems, and the Khan-Sham formalism. Additionally, the functional forms of the exchange and correlation energy in the local density approximation and the generalized gradient approximation has been discussed, along with their implementation within SIESTA.

## 2.9 Bibliography


1. Argaman, N., & Makov, G. (2000). Density functional theory: An introduction. American Journal of Physics, 68(1), 69–79. doi:10.1119/1.19375
2. Dronskowski, R. (2005). Computational Chemistry of Solid State Materials. doi:10.1002/9783527612277
3. Parr, R. G., & Weitao, Y. (1995). Density-Functional Theory of Atoms and Molecules. doi:10.1093/oso/9780195092769.001.0001
4. Lieb, E. H. (1982). Erratum: Thomas-Fermi and related theories of atoms and molecules. Reviews of Modern Physics, 54(1), 311–311. doi:10.1103/revmodphys.54.311
5. Kumar, A. (2012). A Brief Introduction to Thomas-Fermi Model in Partial Differential Equations.
6. Kohn, W., & Sham, L. J. (1965). Self-consistent equations including exchange and correlation effects. Physical Review, 140(4A). doi:10.1103/physrev.140.a1133
7. Soler, J. M., Artacho, E., Gale, J. D., García, A., Junquera, J., Ordejón, P., & Sánchez-Portal, D. (2002a). The siesta method forab initioorder-nmaterials simulation. Journal of Physics: Condensed Matter, 14(11), 2745–2779. doi:10.1088/0953-8984/14/11/302
8. Hagedorn, G. A. (1980). A time dependent born-oppenheimer approximation. Communications in Mathematical Physics, 77(1), 1–19. doi:10.1007/bf01205036
9. M. Born., & J. R. Oppenheimer, (1927) “On the quantum theory of molecules,” Ann.Physik, vol. 84, no. 20, pp. 457–484.
10. Bartók-Pártay, A. (2010). Interatomic potentials. The Gaussian Approximation Potential, 33–49. doi:10.1007/978-3-642-14067-9_4

11. Sahni, V. (2004). The hohenberg-kohn theorems and kohn-sham density functional theory. Quantal Density Functional Theory, 99–123. doi:10.1007/978-3-662-09624-6_4
12. Hohenberg, P., & Kohn, W. (1964). Inhomogeneous Electron Gas. Physical Review, 136(3B). doi:10.1103/physrev.136.b864
13. Martin, R. M. (2004). Electronic Structure. doi:10.1017/cbo9780511805769
14. Kohn, W., Becke, A. D., & Parr, R. G. (1996). Density functional theory of electronic structure. The Journal of Physical Chemistry, 100(31), 12974–12980. doi:10.1021/jp960669l
15. Kohn, W. (1999). Nobel lecture: Electronic structure of matter—wave functions and density functionals. Reviews of Modern Physics, 71(5), 1253–1266. doi:10.1103/revmodphys.71.1253
16. Levy, M. (1979). Universal variational functionals of electron densities, first-order density matrices, and natural spin-orbitals and solution of the representability problem. Proceedings of the National Academy of Sciences, 76(12), 6062–6065. doi:10.1073/pnas.76.12.6062
17. Burke, K. (2012). Perspective on density functional theory. The Journal of Chemical Physics, 136(15). doi:10.1063/1.4704546
18. Kohn, W., & Sham, L. J. (1965a). Self-consistent equations including exchange and correlation effects. Physical Review, 140(4A). doi:10.1103/physrev.140.a1133
19. Parr, R. G. (1980). Density functional theory of atoms and molecules. Horizons of Quantum Chemistry, 5–15. doi:10.1007/978-94-009-9027-2_2
20. Ceperley, D. M., & Alder, B. J. (1980). Ground state of the electron gas by a stochastic method. Physical Review Letters, 45(7), 566–569. doi:10.1103/physrevlett.45.566

21. Langreth, D. C., & Perdew, J. P. (1977). Exchange-correlation energy of a metallic surface: Wave-vector analysis. Physical Review B, 15(6), 2884–2901. doi:10.1103/physrevb.15.2884
22. Becke, A. D. (1988). Density-functional exchange-energy approximation with correct asymptotic behavior. Physical Review A, 38(6), 3098–3100. doi:10.1103/physreva.38.3098
23. Perdew, J. P., & Wang, Y. (1992). Accurate and simple analytic representation of the electron-gas correlation energy. Physical Review B, 45(23), 13244–13249. doi:10.1103/physrevb.45.13244
24. Perdew, J. P., Burke, K., & Ernzerhof, M. (1996). Generalized gradient approximation made simple. Physical Review Letters, 77(18), 3865–3868. doi:10.1103/physrevlett.77.3865
25. Hammer, B., Hansen, L. B., & Nørskov, J. K. (1999). Improved adsorption energetics within density-functional theory using revised Perdew-Burke-Ernzerhof functionals. Physical Review B, 59(11), 7413–7421. doi:10.1103/physrevb.59.7413
26. Soler, J. M., Artacho, E., Gale, J. D., García, A., Junquera, J., Ordejón, P., & Sánchez-Portal, D. (2002a). The siesta method forab initioorder-nmaterials simulation. Journal of Physics: Condensed Matter, 14(11), 2745–2779. doi:10.1088/0953-8984/14/11/302
27. Fermi, E. (1934). Sopra lo spostamento per pressione delle Righe elevate delle Serie SPETTRALI. Il Nuovo Cimento, 11(3), 157–166. doi:10.1007/bf02959829
28. E. Fermi. (1936). Motion of neutrons in hydrogenous substances. Ricerca sci
29. Animalu, A. O. E., & Heine, V. (1965). The screened model potential for 25 elements. Philosophical Magazine, 12(120), 1249–1270. doi:10.1080/14786436508228674
30. Abarenkov, I. V., & Heine, V. (1965a). The model potential for positive ions. Philosophical Magazine, 12(117), 529–537. doi:10.1080/14786436508218898

31. Ashcroft, N. W. (1966). Electron-ion pseudopotentials in metals. Physics Letters, 23(1), 48–50. doi:10.1016/0031-9163(66)90251-4
32. Zunger, A., & Cohen, M. L. (1978). First-principles nonlocal-pseudopotential approach in the density-functional formalism: Development and application to atoms. Physical Review B, 18(10), 5449–5472. doi:10.1103/physrevb.18.5449
33. Bachelet, G. B., & Schlüter, M. (1982). Relativistic norm-conserving pseudopotentials. Physical Review B, 25(4), 2103–2108. doi:10.1103/physrevb.25.2103
34. Perdew, J. P., & Zunger, A. (1981). Self-interaction correction to density-functional approximations for many-electron systems. Physical Review B, 23(10), 5048–5079. doi:10.1103/physrevb.23.5048
35. Fernández-Seivane, F., Oliveira, M. A., Sanvito, S., & Ferrer, J. (2007). On-site approximation for spin–orbit coupling in linear combination of atomic orbitals density functional methods. Journal of Physics: Condensed Matter, 19(48), 489001. doi:10.1088/0953-8984/19/48/489001
36. Atomic Orbital Basis Sets.Webarchive.
37. Haynes, P. D., Skylaris, C.-K., Mostofi, A. A., & Payne, M. C. (2006). Elimination of basis set superposition error in linear-scaling density-functional calculations with local orbitals optimised in situ. Chemical Physics Letters, 422(4–6), 345–349. doi:10.1016/j.cplett.2006.02.086
38. Daza, M. C., Dobado, J. A., Molina, J. M., Salvador, P., Duran, M., & Villaveces, J. L. (1999). Basis set superposition error-counterpoise corrected potential energy surfaces. application to hydrogen peroxide···x (x=F−,cl−, br−,li+,na+) complexes. The Journal of Chemical Physics, 110(24), 11806–11813. doi:10.1063/1.479166
39. Sherrill, C. D. Counterpoise Correction and Basis Set Superposition Error.

40. van Duijneveldt, F. B., van Duijneveldt-van de Rijdt, J. G., & van Lenthe, J. H. (1994). State of the art in Counterpoise theory. Chemical Reviews, 94(7), 1873–1885. doi:10.1021/cr00031a007

# Chapter 3

## Transport Theory and Green's Function Methods

### 3.1 Introduction

A scattering theory and Green's function are techniques that can describe the electron transport and thermoelectric properties of organic molecule systems sandwiched between two gold electrodes. As explained earlier, the coupling strength between the leads and the molecule is usually small compared to the intra-electrode or intra-molecule bond strengths, which introduces a scattering process from the electrode to the molecule and from the molecule to the electrode. To describe these effects, Green's function and scattering theory are considered one of the greatest methods that are widely used in studying these systems. This thesis focuses mainly on Green's functions combined with the Landauer formalism, to describe electron transport properties and how they are related to the transmission coefficient for electrons moving between the two leads passing through the scattering region. The following section will discuss the scattering theory that calculates the transmission and reflection amplitudes. Afterwards, Green's functions are applied to different transport systems to compute the transmission coefficient T(E) of electrons of energy E passing through the molecule from one electrode to another. A brief overview of the thermoelectric coefficients, which describe the voltage difference $\Delta V$ generated due to the temperature difference $\Delta T$ of two electrodes, when they are connected to hot and cold reservoirs respectively will be presented in the last section of this chapter.

### 3.2 The Landauer Formula


**Figure 3.1**: A generic scattering region is connected to two ballistic leads with the chemical potentials $\mu_L$ and $\mu_R$ respectively, where $\boldsymbol{r}$ is the amplitude of the reflected wave due to an incoming wave from the left and $\boldsymbol{t}$ is the amplitude of the transmitted wave.

The Landauer formula [1-2-3] is a theoretical approach to investigate the transport properties in ballistic mesoscopic systems and it applies to phase-coherent systems, where the electrical flow can be described by a single wave function. It connects a mesoscopic sample's conductance to the electrons' transmission characteristics as they go through it. To clear that by supposing that we have a mesoscopic scatterer connected to two perfect ballistic leads that operate as electron reservoirs as shown in Figure 3.1.

The current passing of the electrodes is given by

$$I = \frac{2e}{h}\int_{-\infty}^{\infty} dE\, T(E)\left[f_{left}(E)-f_{right}(E)\right] \tag{3.1}$$

where:

T(E) is the transmission of the electron passing from left to the right leads through the molecule, e is the electron charge and, $f_{left}(E)$ , $f_{right}(E)$ are Fermi-Dirac distribution functions of the left and right reservoirs which is given by:

$$f_{left}(E) = \left[e^{\frac{(E-E_F^{left})}{K_B T}} + 1\right]^{-1}, \qquad f_{right}(E) = \left[e^{\frac{(E-E_F^{right})}{K_B T}} + 1\right]^{-1} \tag{3.2}$$

Here [T] is the temperature,$[K_B]$ is the Boltzmann constant, and [ $E_f^{left}, E_f^{right}$ ] are the Fermi energy [16] of the left and right reservoirs, respectively. The electrical conductance can be obtained in the limit of the zero voltage and a finite temperature, when the average of the T(E)

over an energy window of width eV that is centered on the Fermi energy. The electrical conductance is $\left(G=\frac{I}{V}\right)$ and at zero voltage and a finite temperature, takes the form:

$$G = G_o \int_{-\infty}^{\infty} dE\, T(E)\left(-\frac{df(E)}{dE}\right) \tag{3.3}$$

where $G_o$ is the quantum of conductance is equal to $\frac{2e^2}{h} = 77\ \mu s$

$-\frac{df(E)}{dE}$ is the probability distribution of width approximately$K_B T$. (3.4)

The electrical conductance proportional to the transmission coefficient at the limit of zero voltage and zero temperature followed by

$$G = G_o T(E_F) \tag{3.5}$$

### 3.3 Scattering Matrix

It is crucial to calculate the scattering matrix to understand the transmission coefficient appearing in the formulae above. It is defined as the relationship between the incoming waves and outgoing waves and how they depend on the energy E of the electron. To determine this, we look at the solution of the time-independent Schrödinger equation for an electron in the left and right electrodes in one dimension.

The eigenstate of the electron in the left electrode can be written as:

$$\psi_j = \frac{A}{\sqrt{vl}} e^{ikj} + \frac{B}{\sqrt{vl}} Be^{-ikj} \tag{3.6}$$

Here, $vl$ is the group velocity in the left electrode and, $A$ and $B$ are the amplitudes of the ingoing and outgoing waves travelling from the left to the right, the current per unit energy of the eigenstate is as follows:

$$I_{left} = |A^2| - |B^2| \tag{3.7}$$

Now, the same for the right electrode which the eigenstate of the electron in the right electrode can be written as:

$$\psi_j = \frac{C}{\sqrt{v_r}} e^{ik_r j} + \frac{D}{\sqrt{v_r}} B e^{-ik_r j} \quad (3.8)$$

And the current per unit energy is given by:

$$I_{right} = |C^2| - |D^2| \quad (3.9)$$

where C and D are the amplitudes of the two ingoing and outgoing waves travelling to the right and left, respectively.

Since the currents satisfy the relationship between $I_{left} = I_{right}$

$$|A| - |B| = |C| - |D| \quad (3.10)$$

Hence,

$$|A^2| + |B^2| = |C^2| + |D^2| \quad (3.11)$$

Due to the incoming current is equal to outgoing current, the wave functions for both electrodes respectively are related to each other.

$$\psi_j = Ae^{ikj} + Be^{-ikj} \quad (3.12)$$

$$\phi_j = Ce^{ikj} + De^{-ikj} \quad (3.13)$$

Since the scattering matrix can be defined as the relationship between the incoming waves and outgoing coefficients and satisfies

$$\begin{pmatrix} B \\ C \end{pmatrix} \begin{pmatrix} S_{11} & S_{12} \\ S_{21} & S_{22} \end{pmatrix} \begin{pmatrix} A \\ D \end{pmatrix} \quad (3.14)$$

$$B = S_{11} A + S_{12} D \quad (3.15)$$

$$C = S_{21} A + S_{22} D \quad (3.16)$$

where B and C are the amplitudes of incoming plan waves that carry the electrons passing through the scatterer while A and D are the amplitudes of outgoing waves. To gain insight into the elements of scattering matrix, two cases would be considered. The first one is A=1 and D=0, then B= r, and C=t where is the amplitude of the reflected wave due to an incoming wave from the left and $t$ is the amplitude of the transmitted wave hence,

$$\begin{pmatrix} B \\ C \end{pmatrix} \begin{pmatrix} S_{11} \\ S_{21} \end{pmatrix} \quad (3.17)$$

where $S_{11}$ and $S_{21}$ are the reflection ($r$) and the transmission ($t$) respectively, associated with an incident wave from the left. And the second case is A=0 and D=1, then

$$\begin{pmatrix} B \\ C \end{pmatrix} \begin{pmatrix} S_{12} \\ S_{22} \end{pmatrix} \tag{3.18}$$

where $S_{12}$ and $S_{22}$ are the reflection ($r$) and the transmission ($t$) respectively, associated with an incident wave from the right. To sum up, the transmission and reflection coefficients are represented as the scattering matrix which given by:

$$S = \begin{pmatrix} r_E & t'_E \\ t_E & t'_E \end{pmatrix} \tag{3.19}$$

Note that, the matrix S is a unitary matrix satisfying

$$ss^{-1} = ss^{\dagger} = 1 \tag{3.20}$$

That means the current carried by incoming waves is equal to the current carried by outgoing waves. Following that

, the sum of transmission and reflection probabilities is unity.

$$\begin{gathered} |t|^2 + |r|^2 = 1 \\ T(E) + R(E) = 1 \end{gathered} \tag{3.21}$$

where $t$ is the amplitude of transmitted wave functions, $r$ is amplitude of reflected waves, T(E) is the transmission coefficient and R(E) is the reflection coefficient.

### 3.4 Green's Functions

Green's functions are a crucial tool for determining the transmission and reflection coefficients of various nanoscale structures. This section will provide a detailed explanation of the methods employed, beginning with Green's functions for various nanoscale systems. Thus, the form of the Green's function for a simple one-dimensional discretised lattice will be discussed first and then, use Dyson's equation to demonstrate how to connect Green's functions of these separable lattices to construct the Green's function of the entire system.

#### 3.4.1 Green's Function of a Doubly Infinite Chain

The form of the Green's function of a doubly infinite chain, with on-site energies $\varepsilon_o$ and hopping parameters -γ is illustrated in Figure3.2.

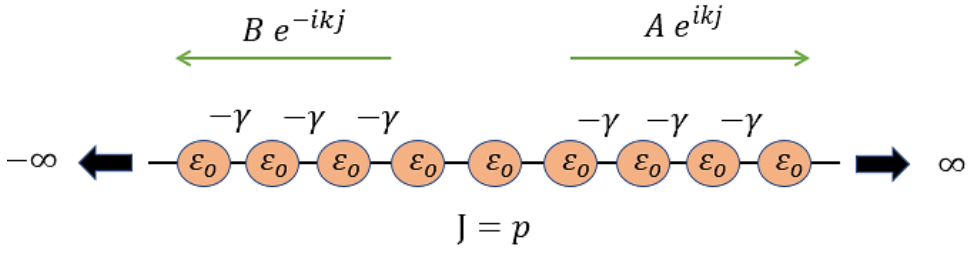


**Figure 3.2:** Representation of tight binding model of one-dimensional infinite chain with on-site energies $\varepsilon_o$ and couplings -γ.

The Green's function G(E) that described by the Hamiltonian H is:

$$(EI\text{-}H)G(E) = I \tag{3.22}$$

Since I is the unit matrix. For a finite system we can write the solution of equation (3.22) as

$$G(E) = (E\text{-}H)^{-1} \tag{3.23}$$

where $G_{jp}$ can be chosen to be the retarded Green's function [4], which describes the system response at point *j* to source p . It is useful to use the following notation to emphasise how Green's functions and wavefunctions (due to a source) relate to one another.

$$G_{jl} = \psi_j^{(p)} \tag{3.24}$$

where $G_{jp}$ is Green's matrix element which belong to the $p^{th}$ column and $j^{th}$row, $\psi_j^{(p)}$ is the amplitude of column vector $\psi^{(p)}$ on site j .

In general, equation (3.23) can be written as

$$\sum_l^{\infty}(EI\text{-}H)_{jl}G_{jp}(E) = \delta_{jp} \tag{3.25}$$

or equivalently

$$\sum_{l=-\infty}^{\infty} H_{jl}\, G_{jp}(E) = EG_{jp}(E)\text{-}\delta_{jp} \tag{3.26}$$

where $\delta_{jp}$ is Kronecker delta which satisfies.

$$\delta_{jl} = 1 \text{ if } j = p \text{ and } \delta_{jp} = 0 \text{ if } j \neq p \tag{3.27}$$

Now, we can substitute equation (3.23) into equation (3.26) we get

$$\sum_{l=-\infty}^{\infty} H_{jl}\ \psi_l^{(p)} = E\psi_j^{(p)}\text{-}\delta_{jp} \tag{3.28}$$

This is nearly similar to the Schrodinger equation with the exception of the Kronecker delta on the right side. Therefore, equation (3.28) can be written as:

$$\varepsilon_o\, \psi_j^{(p)}\text{-}\gamma\psi_{j-1}^{(p)}\text{-}\gamma\psi_{j+1}^{(p)} = E\psi_j^{(p)}\text{-}\delta_{jp} \tag{3.29}$$

The solution of the equation (3.29) can be presented as:

$$\psi_j^{(p)} = \phi_j = A\, e^{ikj} \text{ for } j > p \tag{3.30}$$

$$\psi_j^{(p)} = f_j = B\, e^{-ikj} \text{ for } j < p \tag{3.31}$$

For $j = p + 1$, equations (3.29) and (3.30) yield

$$\varepsilon_o\, \phi_{p+1}\text{-}\gamma\psi_p^{(p)}\text{-}\gamma\phi_{p+2} = E\phi_{p+1} \tag{3.32}$$

Since $\phi_j$ satisfies equation (3.28) for all values of j, we can obtain

$$\varepsilon_o \phi_{p+1} - \gamma \phi_p - \gamma \phi_{p+2} = E\phi_{p+1} \tag{3.33}$$

By comparing equations (3.32) and (3.33), we get

$$\psi_p^{(p)} = \phi_p \tag{3.34}$$

The same procedure is used for $j = p-1$, which results in

$$\psi_p^{(p)} = f_p \tag{3.35}$$

therefore, equations (3.34) and (3.35) yield the following:

$$\psi_p^{(p)} = \phi_p = f_p \tag{3.36}$$

$A\, e^{ikp} = B\, e^{-ikp}$ where $A = C\, e^{-ikp}$ and $B = C\, e^{ikp}$, hence

$$\phi_j = Ce^{ik(j-p)} \text{ and } f_j = Ce^{-ik(j-p)} \tag{3.37}$$

where C is a constant. By combining these with equations (3.30) and (3.31) one obtains

$$\psi_j^{(p)} = Ce^{ik|j-p|} \tag{3.38}$$

$$\text{Where } C = \frac{1}{2i\gamma \sin k} = \frac{1}{i\hbar v(E)} \tag{3.39}$$

where $v(E)$ is the group velocity. Thus, the retarded Green's function, which describes the two outgoing waves from the source p, is given by:

$$G_{jp}(E) = \psi_j^{(p)} = \frac{e^{ik|j-p|}}{i\hbar v(E)} \tag{3.40}$$

Therefore, the most general solution is:

$$G_{jp}(E) = \psi_j^{(p)} = \frac{e^{ik|j-p|}}{i\hbar v(E)} + Ae^{ikj} + Be^{-ikj} \tag{3.41}$$

where A and B are arbitrary constants, choosing $A = -\frac{e^{ik(j-p)}}{i\hbar v}$ and $B = -\frac{e^{-ik(j-p)}}{i\hbar v}$, the Green's function is obtained, which is called advanced Green's function (the complex conjugate of the retarded Green's function).

$$G_{jp}(E) = \psi_j^{(p)} = -\frac{e^{-ik(E)|j-p|}}{i\hbar v(E)} \tag{3.42}$$

### 3.4.2 Green's Functions of a Semi-Infinite Linear Chain

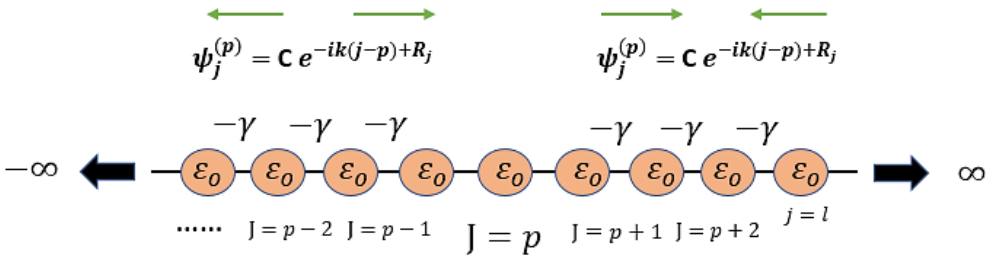


**Figure 3.3:** Representation of tight binding model of semi-infinite linear chain with site energies $\varepsilon_o$ and hopping elements -γ**,** which terminates at site j = l.

Consider the semi-infinite chain with site energies $\varepsilon_o$ and hopping elements -γ, as shown in Figure.3.3, in which the chain terminates at site j = l , where l ≥ p. This leads to the following boundary condition

$$\psi_{l+1}^{(p)} = 0 \tag{3.43}$$

Fig. 3.3 shows the reflected plane wave $e^{-ikj}$ will be created due to the hitting of the incoming plane wave $e^{ikj}$ to the end of the chain. Therefore, the reflected wave will be added to the retarded Green's function

$$G_{jp}(E) = \frac{e^{ik|j-p|}}{i\hbar v(E)} + B\, e^{-ikj} \tag{3.44}$$

where $$B = -\frac{e^{ik(2l+2-p)}}{i\hbar v(E)}$$

Hence, the retarded Green's function takes the form as follow:

$$G_{jp}(E) = \psi_j^{(p)} = \frac{e^{ik|j-p|} - e^{-ik(j+p-2l-2)}}{i\hbar v(E)} \tag{3.45}$$

On the other hand, if the chain terminates at site l ≤ p, the boundary condition becomes

$$\psi_{l-1}^{(p)} = 0$$

Thus, the Green's function is:

$$G_{jp}(E) = \psi_j^{(p)} = \frac{e^{ik|j-p|} - e^{ik(j+p-2l+2)}}{i\hbar v(E)} \tag{3.46}$$

The Green's function on the terminal site $j = l$ due to the source at site $p = l$ is:

$$G_{ll}(E) = -\frac{e^{ik(E)}}{\gamma} \tag{3.47}$$

which is called the surface Green's function.

### 3.5 Transport Through an Arbitrary Scattering Region

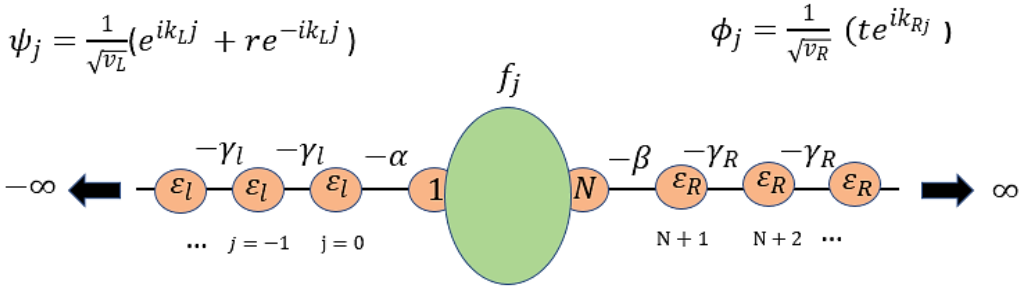


**Figure 3.4:** Tight-binding representation of an arbitrary scattering region attached to (1-D) leads.

To find the most general formula for the transmission coefficient of an arbitrary scattering region, I consider the structure shown in Fig. 3.4, which consists of two semi-infinite chains, in which the site energies and hopping elements in the left (right) lead are $\varepsilon_l(\varepsilon_R)$ and $-\gamma_l(-\gamma_R)$, respectively. The leads are connected to the scattering region at sites 1 and N by coupling $-\alpha$ and $-\beta$.

Our aim is to solve the Schrodinger equation

$$\sum_{l=-\infty}^{\infty} H_{jl}\psi_l = E\psi_j$$

The eigenvector amplitudes $\psi_j$ for the left lead, $\phi_j$ for the right lead and $f_j$ for the scattering region, in which the plane waves are normalized to unit current:

$$\psi_j = \frac{1}{\sqrt{v_L}} \left[ e^{ik_L j} + re^{-ik_L j} \right] \tag{3.48}$$

$$\phi_j = \frac{1}{\sqrt{v_R}} \left[ te^{ik_R j} \right] \tag{3.49}$$

The Schrodinger equation takes the following form:

$$\varepsilon_L \psi_j - \gamma_L \psi_{j-1} - \gamma_L \psi_{j+1} = E\psi_j \qquad \text{for } j < 0 \tag{3.50}$$

$$\varepsilon_L \psi_o - \gamma_L \psi_{-1} - \alpha f_1 = E\psi_o \qquad \text{for } j = 0 \tag{3.51}$$

$$\sum_{l=1}^{N} H_{jl} f_l - \alpha\psi_o \delta_{j1} - \beta\phi_{N+1} \delta_{jN} = E f_j \qquad \text{for } 1 \le j \le N \tag{3.52}$$

$$\varepsilon_R \phi_{N+1} - \gamma_R \phi_{N+2} - \beta f_N = E\phi_{N+1} \qquad \text{for } j = N+1 \tag{3.53}$$

$$\varepsilon_R \phi_j - \gamma_R \phi_{j+1} - \gamma_R \phi_{j-1} = E\phi_j \qquad \text{for } j > N+1 \tag{3.54}$$

Equation (3.52) could be re-written as:

$$|f\rangle = g|s\rangle \tag{3.55}$$

where,

$$g = (EI - H)^{-1}$$

g is the Green's function of an isolated scatterer. $|s\rangle$ is the source which is a zero vector with non-zero elements in the connection points only (at site j=1 and j = N).

$$|f\rangle = \begin{pmatrix} f_1 \\ f_2 \\ . \\ . \\ f_N \end{pmatrix} \qquad |s\rangle = \begin{pmatrix} -\alpha\psi_o \\ o \\ o \\ o \\ -\beta\phi_{N+1} \end{pmatrix}$$

For the junction shown in Fig. 3.4, $|f\rangle$ has only two non-zero elements due to the source. Therefore, equation (3.55) can be written as:

$$\begin{pmatrix} f_1 \\ f_N \end{pmatrix} = \begin{pmatrix} g_{11} & g_{1N} \\ g_{N1} & g_{NN} \end{pmatrix} \begin{pmatrix} -\alpha\psi_o \\ -\beta\phi_{N+1} \end{pmatrix} \tag{3.56}$$

$$\tilde{g}^{-1} \begin{pmatrix} f_1 \\ f_N \end{pmatrix} = \begin{pmatrix} -\alpha\psi_o \\ -\beta\phi_{N+1} \end{pmatrix} \tag{3.57}$$

where, $\tilde{g}^{-1}$ is the inverse of the $2 \times 2$ sub matrix of Green's function.

By using the recurrence relation, we obtain the following:

$$\gamma_L \psi_1 = \alpha f_1$$

$$\gamma_R \phi_N = \beta f_N$$

From equations (3.48) and (3.49), we find

$$\phi_{N+1} = \phi_N e^{ik_R} \tag{3.58}$$

$$\psi_1 = \frac{1}{\sqrt{v_L}}[2i \sin k_L] + \psi_o e^{-ik_L} \tag{3.59}$$

Hence,

$$\begin{pmatrix} -\alpha\psi_o \\ -\beta\phi_{N+1} \end{pmatrix} = \Sigma \begin{pmatrix} f_1 \\ f_N \end{pmatrix} + \begin{pmatrix} \frac{\alpha e^{ik_L}}{\sqrt{v_L}}[2i \sin k_L] \\ 0 \end{pmatrix} \tag{3.60}$$

where

$$\Sigma = \begin{pmatrix} \Sigma_L & 0 \\ 0 & \Sigma_R \end{pmatrix}$$

$\Sigma_L = \frac{-\alpha^2 e^{ik_L}}{\gamma_L}$ , $\Sigma_R = \frac{-\beta^2 e^{ik_R}}{\gamma_R}$ are the self-energies associated with the left and right leads, respectively. Substituting equation (3.60) into equation (3.57) yields

$$((\tilde{g})^{-1} - \Sigma) \begin{pmatrix} f_1 \\ f_N \end{pmatrix} = \begin{pmatrix} \frac{\alpha e^{ik_L}}{\sqrt{v_L}}[2i \sin k_L] \\ 0 \end{pmatrix} \tag{3.61}$$

Thus,

$$\begin{pmatrix} f_1 \\ f_N \end{pmatrix} = G \begin{pmatrix} \frac{\alpha e^{ik_L}}{\sqrt{v_L}}[2i \sin k_L] \\ 0 \end{pmatrix} \tag{3.62}$$

where

$$G = ((\tilde{g})^{-1} - \Sigma)^{-1} = \begin{pmatrix} G_{11} & G_{12} \\ G_{N1} & G_{NN} \end{pmatrix} \tag{3.63}$$

From equation (3.62),

$$f_N = G_{N1} \frac{\alpha e^{ik_L}}{\sqrt{v_L}} [2i \sin k_L] = \frac{\gamma_R}{\beta} \phi_N \tag{3.64}$$

Since $\emptyset_N = \frac{1}{\sqrt{v_R}} \left[te^{ik_R N}\right]$, $\hbar v_R = 2\gamma_R \sin k_R$ and $\hbar v_L = 2\gamma_L \sin k_L$, I get the following:

$$t = iG_{N1}\alpha\,\beta e^{ik_L}\sqrt{\frac{2\sin k_L}{\gamma_L}}\quad\sqrt{\frac{2\sin k_R}{\gamma_R}}\quad e^{-ik_R N} \tag{3.65}$$

$$T(E) = |t|^2 = 4\left[\frac{\alpha^2\sin k_L}{\gamma_L}\right]\left[\frac{\beta^2\sin k_R}{\gamma_R}\right]\ |G_{N1}|^2 \tag{3.66}$$

Since $$|G_{N1}|^2 = \left|\frac{g_{N1}}{\Delta}\right|^2$$

where $$\Delta = 1-g_{11}\,\Sigma_L - g_{NN}\,\Sigma_R + \Sigma_L\,\Sigma_R[g_{11}\,g_{NN}-g_{1N}\,g_{N1}]$$

Thus, the most general formula that used to calculate the transmission probability of any scattering region that is connected to different one-dimensional leads [4] as follow:

$$T(E) = |t|^2 = 4\left[\frac{\alpha^2\sin k_L}{\gamma_L}\right]\left[\frac{\beta^2\sin k_R}{\gamma_R}\right]\ \left|\frac{g_{N1}}{\Delta}\right|^2 \tag{3.67}$$

### 3.6 Breit-Wigner Resonances

Development of transport resonances and anti-resonances related to quantum interference [5-6] is the primary characteristic of electron transport via single molecules and phase-coherent nanostructures. It will be helpful to discuss a Breit-Wigner resonance [4-7] to get a general knowledge of the features of these resonances. This illustrates how, transmission function resonances or anti-resonances are caused by quantum interference between several electron channels. The Breit-Wigner formula (the Lorentzian function), which can be used to express the constructive interference of electrons travelling through a single molecular orbital takes the form:

$$T(E) = \frac{4\,\Gamma_L\,\Gamma_R}{(E-\varepsilon_n)^2+(\Gamma_L+\Gamma_R)^2} \tag{3.68}$$

where $T(E)$ is the transmission coefficient of the electrons, $\Gamma_L$ and $\Gamma_R$ describe the coupling of the molecular orbital to the electrodes. It is essential to mention that $\Gamma$ determines the resonance

width, therefore if the couplings to the electrodes α and β are weak, the resonance will become very narrow.

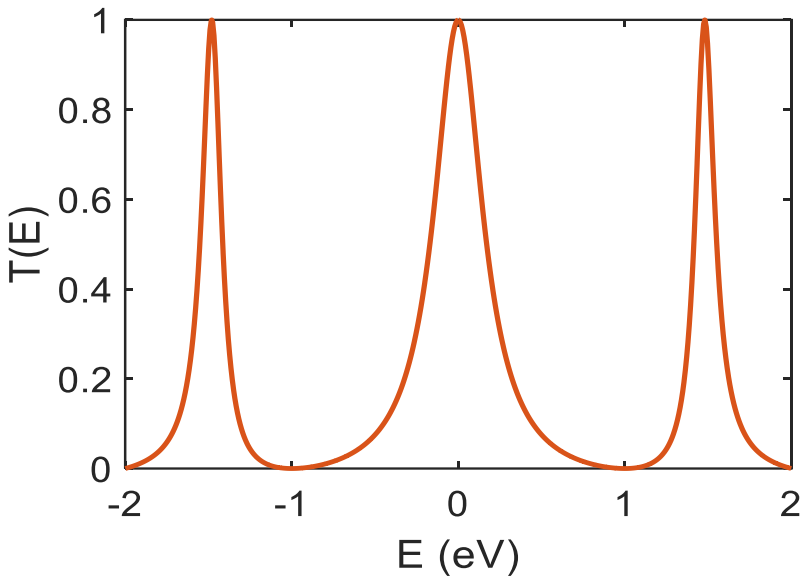


**Figure3.5**: The transmission coefficient for a symmetric molecule attached symmetrically to identical leads ($\Gamma_1 = \Gamma_2$).

As illustrated in Figure 3.5 the transmission coefficient T(E) reaches its greatest value $T(E) = 1$ at $E = \varepsilon_n$ when a symmetric molecule is symmetrically connected to identical electrodes $\Gamma_L = \Gamma_R$. On the other hand, the transmission function has the value $T(\varepsilon_n) = \frac{4\Gamma_R}{\Gamma_L}$ when the junction is asymmetric and $\Gamma_L \gg \Gamma_R$ ). Therefore, asymmetric junctions have a lower on-resonance transmission coefficient than symmetric junctions. is important to note that this formula is valid when the electron's energy is close to an eigenvalue of the isolated molecule and when the molecule's energy level spacing is greater than the resonance's width [4].

### 3 .5 Thermoelectric Coefficients

The link between heat, current, temperature, and voltage was discovered by Seebeck, Peltier, and Thompson in the 19th century [4]. The Thompson and Peltier effects describe how a current-carrying conductor cools or heats as a consequence of a temperature difference, whereas the Seebeck effect explains how electrical voltage is produced as a result of a temperature difference. A more complex process that results in heat and charge variations is one where the system's theoretical value of $\Delta V$ drops and the difference in temperature is $\Delta T$. The Landauer-Büttiker [8] formulas can be generalised to determine the thermoelectric coefficients of a device with two terminals. The system is made up of two leads and two electron reservoirs, as well as a scattering zone that is connected to each of them. These reservoirs are constructed using the chemical potentials $\mu_L$ and $\mu_R$, temperatures $T_L$and $T_R$, and the Fermi distribution function [9]:

$$f_L(E) = \left(1 + e^{\frac{E-\mu_i}{K_B T_L}}\right)^{-1} \tag{3.69}$$

The number of electrons per unit length, the Fermi distribution, the group velocity, and the transmission coefficient of the scattering zone may all be used to represent the right moving charge current of a certain k-state issuing from the left reservoir.

$$I_k^+ = nev_g(E(k))T(E(k))f_L(E(k)) \tag{3.70}$$

the total charge from right moving states can be found by adding up all positive k states and then integrating them into an integral form where $n = 1/L$ for the electron density and $\frac{1}{\check{h}}\frac{dE(k)}{dk}$

$$I_k^+ = \sum_k e\,\frac{1}{L}\frac{1}{\check{h}}\frac{dE(k)}{dk}\,T(E(k))f_L(E(k)) = \int_{-\infty}^{+\infty}\frac{2e}{\check{h}}T(E)f_L(E)dE \tag{3.71}$$

Similar results are obtained for the left moving states as follows:

$$I_k^- = \int_{-\infty}^{+\infty}\frac{2e}{\check{h}}T(E)f_R(E)dE \tag{3.72}$$

As a result, the whole right-moving current which is denoted by the Landauer-Bttiker formula. may be expressed as

$$I = I^{+} - I^{-} = \frac{2e}{\check{h}} \int_{-\infty}^{+\infty} T(E) f_L(E) - f_R(E) dE \quad (3.73)$$

By starting with the relation $\varrho = En v_g$ rather than $= nev_g$ an analogous derivation for the heat current (or energy current) of the same system may be supplied which is the result can be obtained as follows

$$\varrho = \varrho^{+} - \varrho^{-} = \frac{2e}{\check{h}} \int_{-\infty}^{+\infty} T(E) (E - \mu_L) f_L(E) - (E - \mu_R) f_R(E) dE \quad (3.74)$$

In the linear response regime, Buttiker, Imry, Landauer, et al. [10–11] connect the electric current I and heat current (Q) passing through a system to the voltage difference and temperature difference. Thus, currents, temperature, and potential differences are all connected by the thermoelectric coefficients $G, L, M,$ and $K$ [4 and 12-13]

$$\begin{pmatrix} I \\ Q \end{pmatrix} = \begin{pmatrix} G & L \\ M & K \end{pmatrix} \begin{pmatrix} \Delta V \\ \Delta T \end{pmatrix} \quad (3.75)$$

The Onsager relation describes how the thermoelectric coefficients$L$ and $M$ are related when there is no magnetic field.

$$M = -L T \quad (3.76)$$

where T is the temperature. Tthe current relations can be expressed in the rearranging of these equations using the measurable thermoelectric coefficients, electrical resistance $R = 1/G$ ,thermopower $S = \Delta V/\Delta T$ , Peltier coefficient, and the thermal constant which takes the following form:

$$\begin{pmatrix}\Delta V\\ \dot{Q}\end{pmatrix} = \begin{pmatrix}\frac{1}{G} & -\frac{L}{G}\\ \frac{M}{G} & K-\frac{LM}{G}\end{pmatrix}\begin{pmatrix}1\\ \Delta T\end{pmatrix} = \begin{pmatrix}R & S\\ \Pi & -K\end{pmatrix}\begin{pmatrix}1\\ \Delta T\end{pmatrix} \quad (3.77)$$

The thermopower is defined as the potential reduction brought on by a temperature difference in the absence of an electrical current:

$$S = \left(\frac{-\Delta V}{\Delta T}\right)_{I=0} = \frac{L}{G} \quad (3.78)$$

The Peltier coefficient is defined as the heat transmitted entirely owing to the charge current in the absence of a temperature differential:

$$\Pi = \left(\frac{\dot{Q}}{I}\right)_{\Delta T=0} = \frac{M}{G} = -S\,T \quad (3.79)$$

Finally, thermal conductance k is defined as the heat current resulting from a temperature drop in the absence of an electric current:

$$k = -\left(\frac{\dot{Q}}{\Delta T}\right)_{I=0} = -\left(1 + \frac{S^2GT}{k}\right) \quad (3.80)$$

Determining S or Π provides insight on how effectively the device will function as a current-driven cooling or heat-driven current generator.

Additionally, these measurable thermoelectric coefficients may be used to define the thermoelectric figure of merit ZT as follows: [14-15]

$$ZT = \frac{S^2GT}{k} \quad (3.81)$$

In classical electronics ZT can be presented by calculating the greatest induced temperature differential brought on by an electrical current when Joule heating is present, by taking a current-carrying conductor is positioned between two heat baths, $T_L$and $T_R$ and two electrical potentials $V_L$ and $V_R$ respectively.

The thermoelectric figure of merit can be computed by determining the conductor's highest induced temperature difference caused by an electrical current. By defining $\dot{Q}$ as the heat gain from the bath L to R, thus, we can get from equation (3.74)

$$\dot{Q} = \Pi I - k\Delta T \quad (3.82)$$

As a result of this heat transfer, the right bath will heat up, while the left bath cools as well as ΔT will be increasing. It is possible to determine the total amount of Joule heating by using the formula $\dot{Q}_J = RI^2$ which is proportional to electrical resistance and current squared. Additionally, this Joule heating influences the temperature differential produced by heat transfer thus, in the steady state case:

$$\Pi\, I - k\Delta T = \frac{RI^2}{2} \tag{3.83}$$

where $\frac{R}{2}$ is defined as the sum of two parallel resistances (internal and external resistance) hence, the temperature difference can be written as:

$$\Delta T = \frac{1}{k}\left(\Pi\, I - \frac{RI^2}{2}\right) \tag{3.84}$$

This formula demonstrates how the current affects the temperature difference. The derivative of equation (3.83) with respect to the electric current is used to determine the greatest temperature difference:

$$\frac{\partial \Delta T}{\partial I} = \frac{\Pi - I\,R}{k} = 0 \tag{3.85}$$

The maximum temperature difference is obtained by entering $I = \Pi / R$ and substituting equation (3.78) into (3.84) which is giving a dimensionless number that can be used to describe a molecular device's 'efficiency as follows:

$$(\Delta T)_{max} = \frac{\Pi^2}{2kR} = \frac{S^2 T^2\, G}{2k} \tag{3.86}$$

$$\frac{(\Delta T)_{max}}{T} = \frac{S^2 T^2\, G}{2k} = \frac{1}{2} Z \tag{3.87}$$

### 3.6 Conclusion

In conclusion, a single particle transport theory was described, providing the primary numerical tool for researching charge transfer across molecules. There was a description of the theoretical foundations for computing electronic transport, including the investigation of one-dimensional scattering theory and Green's functions for various transport regimes. Additionally, a simple derivation of the Landauer formula was provided.

It explained how to compute the transmission coefficient in a molecular junction for electrons moving between two electrodes. Finally, formulae for thermoelectric coefficients were presented.

## 3.7 Bibliography


1. Li, C., Pobelov, I., Wandlowski, T., Bagrets, A., Arnold, A., & Evers, F. (2007). Charge transport in single au | alkanedithiol | AU junctions: coordination geometries and conformational degrees of freedom. Journal of the American Chemical Society, 130(1), 318–326. doi:10.1021/ja0762386
2. David Visontai. (2011). Quantum and Classical Dynamics of Molecule Size Systems. PhD thesis, Lancaster University.
3. Landauer, R. (1957). Spatial variation of currents and fields due to localized scatterers in metallic conduction. IBM Journal of Research and Development, 1(3), 223–231. doi:10.1147/rd.13.0223
4. Lambert, C. J. (2021). Introduction to molecular-scale electronics. Quantum Transport in Nanostructures and Molecules: An Introduction to Molecular Electronics. doi:10.1088/978-0-7503-3639-0ch1
5. Gantenbein, M., Wang, L., Al-jobory, A. A., Ismael, A. K., Lambert, C. J., Hong, W., & Bryce, M. R. (2017). Quantum interference and heteroaromaticity of para- and meta-linked bridged biphenyl units in single molecular conductance measurements. Scientific Reports, 7(1). doi:10.1038/s41598-017-01903-0
6. Naghibi, S., Ismael, A. K., Vezzoli, A., Al-Khaykanee, M. K., Zheng, X., Grace, I. M., … Nichols, R. J. (2019). Synthetic control of quantum interference by regulating charge on a single atom in heteroaromatic molecular junctions. The Journal of Physical Chemistry Letters, 10(20), 6419–6424. doi:10.1021/acs.jpclett.9b02319
7. Breit, G., & Wigner, E. (1936). Capture of slow neutrons. Physical Review, 49(7), 519–531. doi:10.1103/physrev.49.519

8. Büttiker, M., Imry, Y., Landauer, R., & Pinhas, S. (1985). Generalized many-channel conductance formula with application to small rings. Physical Review B, 31(10), 6207–6215. doi:10.1103/physrevb.31.6207
9. Finch, C. M. (2008). An understanding of the electrical characteristics of organic molecular devices (Doctoral dissertation, Lancaster University).
10. Büttiker, M., Imry, Y., Landauer, R., & Pinhas, S. (1985a). Generalized many-channel conductance formula with application to small rings. Physical Review B, 31(10), 6207–6215. doi:10.1103/physrevb.31.6207
11. Claughton, N. R., & Lambert, C. J. (1996). Thermoelectric properties of mesoscopic superconductors. Physical Review B, 53(10), 6605–6612. doi:10.1103/physrevb.53.6605
12. Sivan, U., & Imry, Y. (1986). Multichannel Landauer formula for thermoelectric transport with application to thermopower near the Mobility Edge. Physical Review B, 33(1), 551–558. doi:10.1103/physrevb.33.551
13. Hicks, L. D., & Dresselhaus, M. S. (1993). Effect of quantum-well structures on the thermoelectric figure of merit. Physical Review B, 47(19), 12727–12731. doi:10.1103/physrevb.47.12727
14. Goldsmid, H. J. (1964). Thermoelectric Refrigeration Plenum. New York.
15. Athanasopoulos, S. (2005). Electronic properties of hybrid carbon nanotubes(Doctoral dissertation, Lancaster University).
16. Cuevas, J. C., & Scheer, E. (2010a). Molecular electronics. World Scientific Series in Nanoscience and Nanotechnology. doi:10.1142/7434

# Chapter 4

## Transport and Thermoelectric Properties of Multicomponent Single Molecules in Gold-Gold Junctions

This chapter provides in-depth theoretical analyses of several multicomponent single molecules using the theoretical techniques that are described in chapters 2 and 3. The aim of this chapter is to demonstrate a strategy for utilizing a multi-component method to fabricate a conjugated molecular backbone on gold and graphene substrates separated with equal distance, using ZnTPP as a footprint and compare it with the amine-based non-conjugated junctions with similar tunneling lengths. Additionally, this chapter examines the change in transport properties when a molecular monolayer or molecule/ZnTPP bilayer is inserted into gold-gold (Au-Au) and gold-graphene (Gr-Au) junctions for eight different mono or bilayers.

The monolayer and bilayer molecules have different anchor groups including direct carbon contact (C) and a pyridyl (Py) contact. To investigate these molecular systems, first I am going to explore their transport properties in Au-Au junctions and then in chapter 5, I shall repeat the same simulations in Au-Gr junctions and finally make a comparison between the two junctions.

### 4.1 Introduction

Molecular electronics, using molecules as building blocks in integrated circuits [1], promise to deliver new generation transistors [2-3], sensors [4], memories [5] and thermoelectric energy harvesters [6-7], due to their nanometre scale and special functionality. Electric and thermoelectric properties molecular junction, either in single molecules [8-9] or self-assembled monolayers (SAMs) scale [10-11], have been intensively studied in the past few years. Most

studies were performed on noble metallic substrates such as Au, Ag, Pt, … etc. Organic molecular backbones terminated with designed anchor groups, include thiolate [12-13], pyridine [14-15], fullerene [16], large π systems [17-18], etc. spontaneously form metal/molecule junctions on the substrate. The coupling strength between anchor groups and the substrate significantly determines the quantum transport property of the junction [6-11-19]. Therefore, studies of heat and charge transfer in such single-molecule junctions are fundamentally very important, because they shed more light on the relationship between junction structure and their transport properties. It is important to note that single-molecule-junction thermoelectric qualities can be adjusted by modifying their transport characteristics, such as lengthening the molecule [4-6] and modifying the molecule-electrode coupling shape.

**4.2 Studied Molecules.**

In this chapter, I will investigate 8 different molecules terminated with asymmetric anchor groups as shown in figure 4.1 and will consider both monolayer and bilayer junctions. For the monolayer junctions, I consider two cases.: Case-1 (panel a), which involves three alkyl chains terminated with asymmetric anchor groups: amine ($NH_2$) , and direct carbon contact ($CH_2$). These are molecule **1**($C_8$ ), molecule **2** ($C_{12}$ ), and molecule **3** ($C_{18}$) ,which are differentiated by their number of $CH_2$ units. Case -2 (panel b) comprises a zinc tetraphenyl porphyrin (ZnTPP) molecule **4**, a small graphene -like molecule (Gr) **5,** and pyridine-terminated molecules **6**, **7** and **8** (molecule **6** consists of 2 pyridine rings, molecule **7** contains two pyridine rings and one phenyl ring, and molecule **8** which has 2 phenyl rings and two pyridine rings). While for the bilayer junctions shown in Figure 4.3, I shall choose zinc tetraphenyl porphyrin (ZnTPP) combined with pyridyl backbone derivatives **6, 7**, and **8** were attached to the ZnTPP layer via a zinc-pyridine coordinative bond). The pyridyl-terminated backbones stand perpendicular to the plane of the ZnTPP and the substrate, because of the pyridyl lone pair coordinates with the Zn, as shown in Figure 4.3.

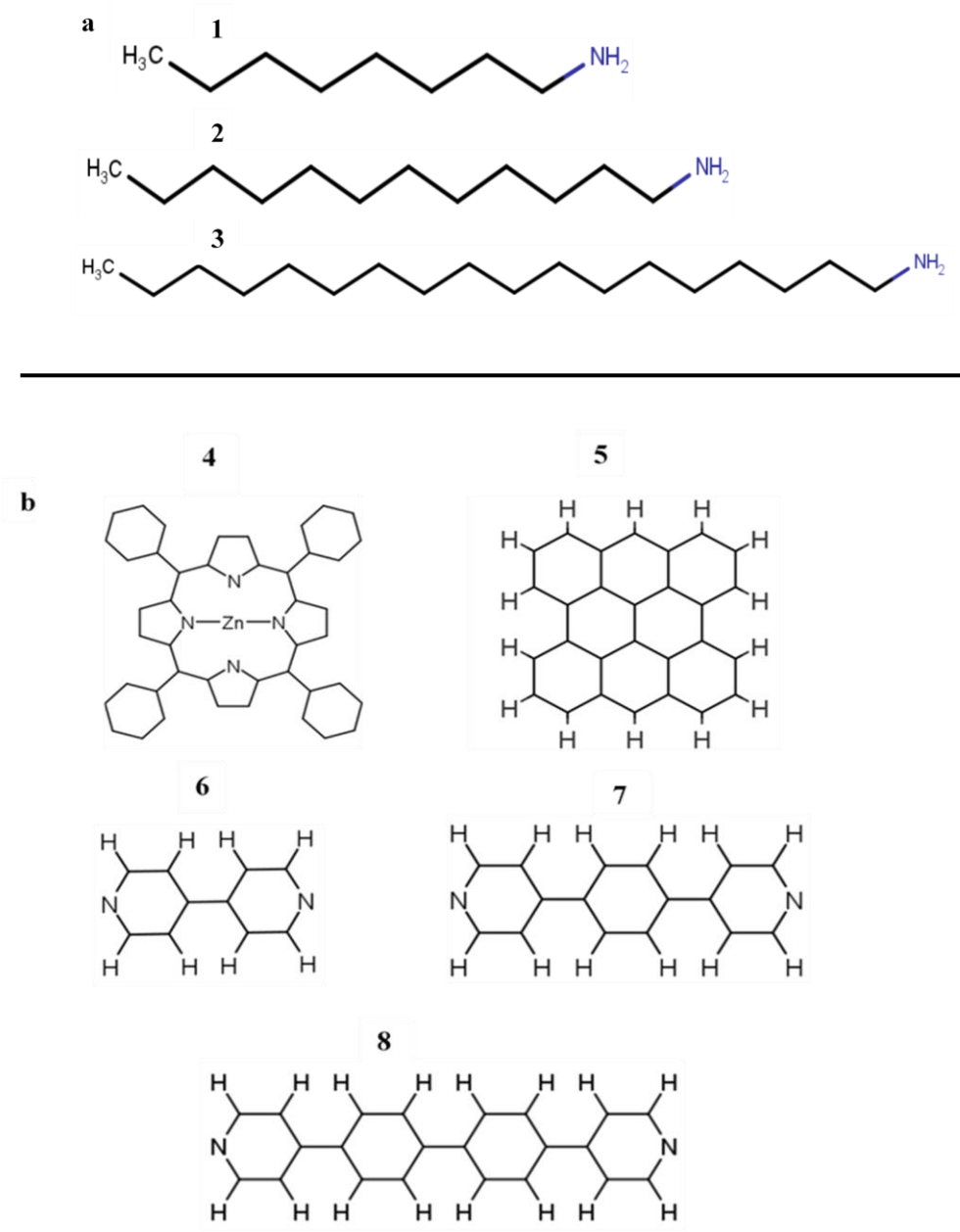


**Figure 4.1:** Chemical structures of studied monolayer molecules. (a): 1($C_8$), 2 ( $C_{12}$ ), and 3 ($C_{18}$ ) are alkyl chains terminated with different anchor groups involving amine and direct carbon, while (b): 4 is a Zinc Tetraphenyl Porphyrin (ZnTPP), 5 is a graphene sheet-based molecule, and 6,7, and 8 are pyridine backbone with pyridine anchors from both ends (molecule 6 which consists of 2 pyridine rings, molecule 7 contains pyridine rings and one benzene and molecule 8 has 2 benzene rings and two pyridine rings.

### 4.3 Optimised DFT Structures of Isolated Molecular-Scale Structures

The optimised geometry and ground state Hamiltonian of each structure in this chapter were obtained using the density functional code SIESTA [21], which has been presented in detail in chapter 2. The optimum geometries of the isolated molecules **1-8** are shown in Figure 4.2 and bilayers **4/6**, **4/7** and **4/8** are shown in Figure 4.3 and were obtained by relaxing the molecules until all forces on the atoms were less than 0.01 eV / Å.[22-23] A double-zeta plus polarization orbital basis set, norm-conserving pseudopotentials, and an energy cut-off of 250 Rydbergs defining the real space grid were used and the generalised gradient approximation (GGA) [22-24] was chosen as the exchange-correlation functional.

### 4.3. Relaxed structures of isolated Molecules

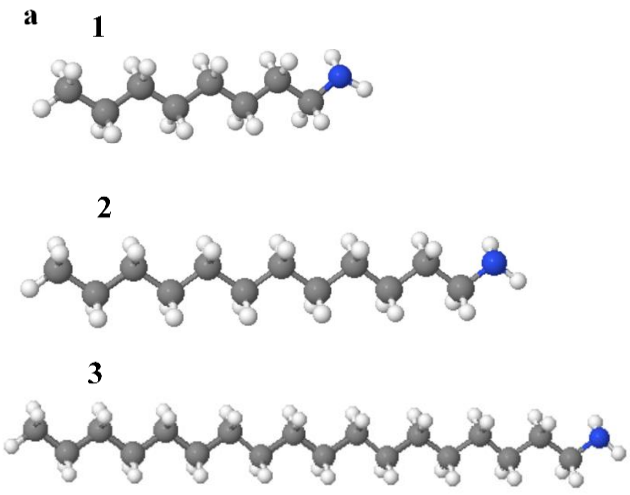

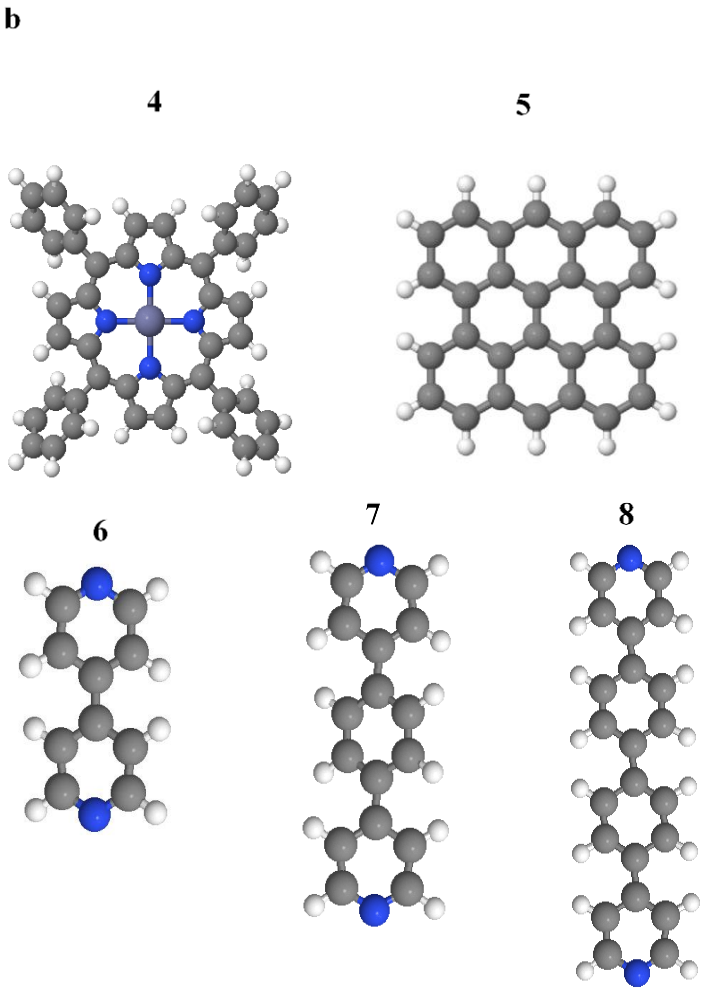


**Figure 4.2**: Fully relaxed isolated monolayer molecules. (a): 1-3 are monolayer molecules that consist of asymmetric alkyl chains of different lengths 8-18 carbon atoms with different anchor groups involving ($NH_2$) and ($CH_2$). (b): 4 Zinc Tetraphenyl Porphyrin (ZnTPP), 5 graphene sheet-based molecules (Gr), and 6,7, and 8 are pyridine backbones with pyridine anchors both end which are component bilayer.

### 4.3.2 Relaxed structures of bilayer Compounds

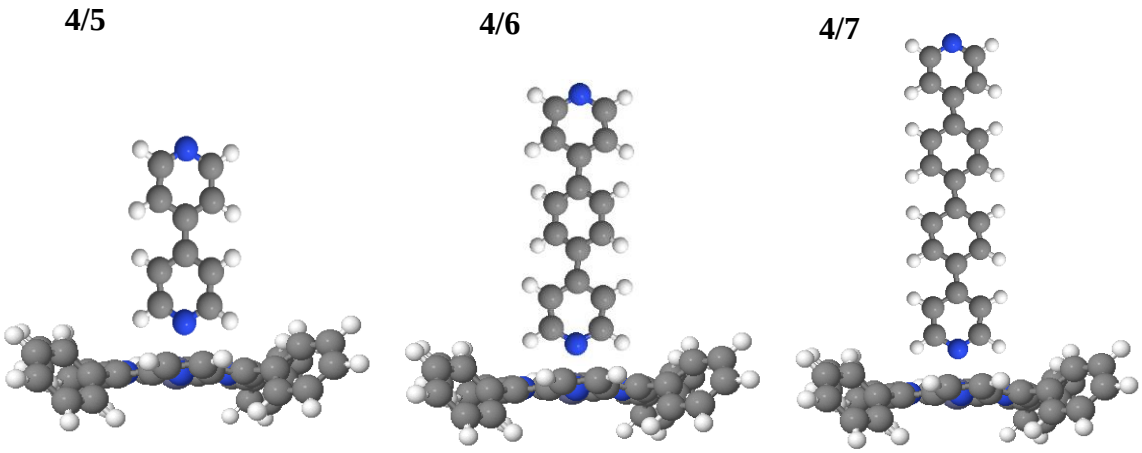


**Figure 4.3: 4/6, 4/7**, and **4/8** are molecular structures assembled by combining the ZnTPP with **6**, **7**and **8** (Fig. 4.2 (b)), and then allowing the system to become fully relaxed to form bilayers.

### 4.4 Frontier Molecular Orbitals

As a first step of understanding the electronic properties of the structures shown in Figures 4.1 and 4.2, the methods introduced in Chapter 2 have been employed. First, the frontier orbitals were investigated for all the gas-phase molecules. Their highest occupied molecular orbitals (HOMO) and lowest unoccupied orbitals (LUMO), in addition to (HOMO+1), and (LUMO-1), along with their energies are investigated. For the molecules **1-8** (see Figure 4.2) and the bilayers **4/6, 4/7,** and **4/8** (see Figure 4.3) , these are shown in Figures 4.4-4.14, where blue and red colours represent the positive and negative orbital amplitudes. Note that, the alkane chains are localized on the amine anchor group as well as bilayers **4/6**, **4/7**, and **4/8** are localized on the (ZnTPP) core. A localized wave function means that the probability of finding the electron outside of that specific location or region of space is essentially zero. While the pyridine backbone molecule **8** is delocalized across the structure. A delocalized wave function means that there is a non-zero probability of finding the electron in a wide range of locations, rather than just in a single, well-defined location.

#### 4.4.1.1 Molecule 1

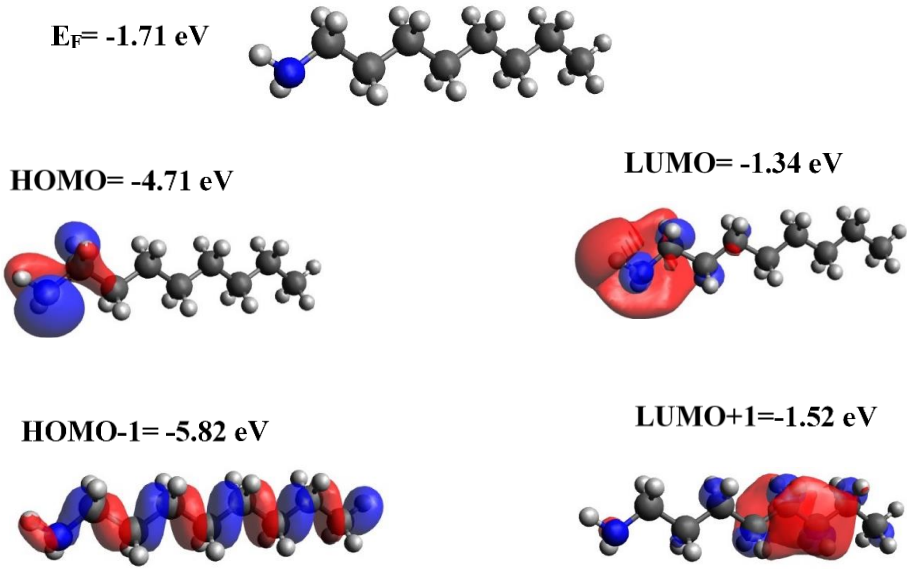


**Figure 4.4:** Wave function for monolayer **1** ($C_8$). **Top panel**: fully optimised geometry of **1.** **Lower panel**: HOMO, LUMO, HOMO-1, LUMO+1 levels of monolayer **1**, along with their energies.

#### 4.4.1.2 Molecule 2

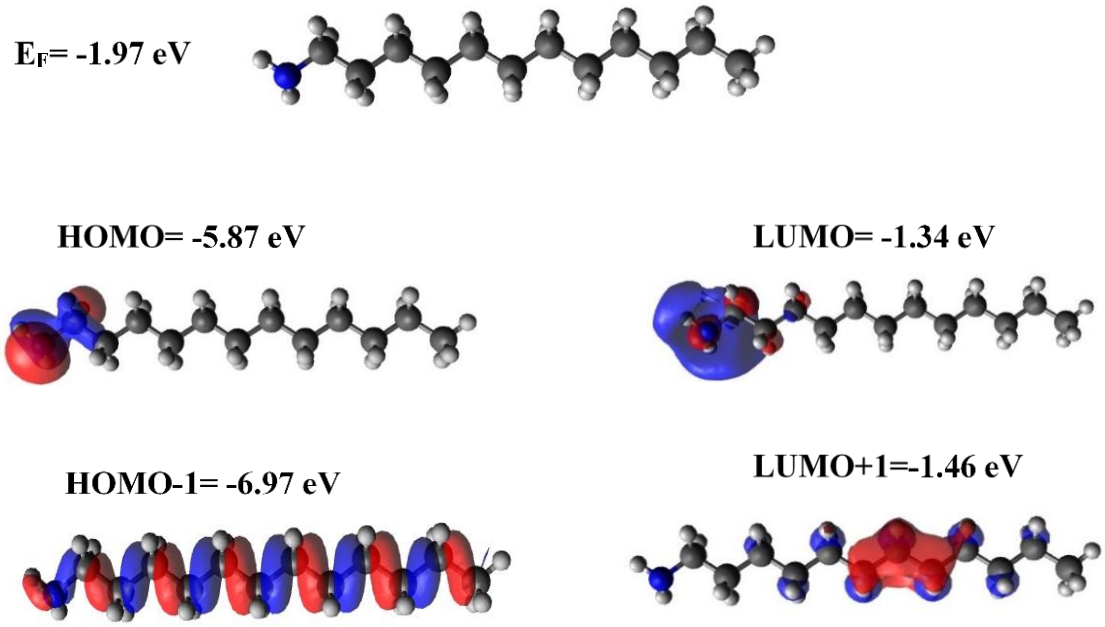


**Figure 4.5**: Wave function for monolayer **2** ($C_{12}$). **Top panel**: fully optimised geometry of **2**. **Lower panel**: HOMO, LUMO, HOMO-1, LUMO+1 levels of monolayer **2**, along with their energies.

#### 4.4.1.3 Molecule 3

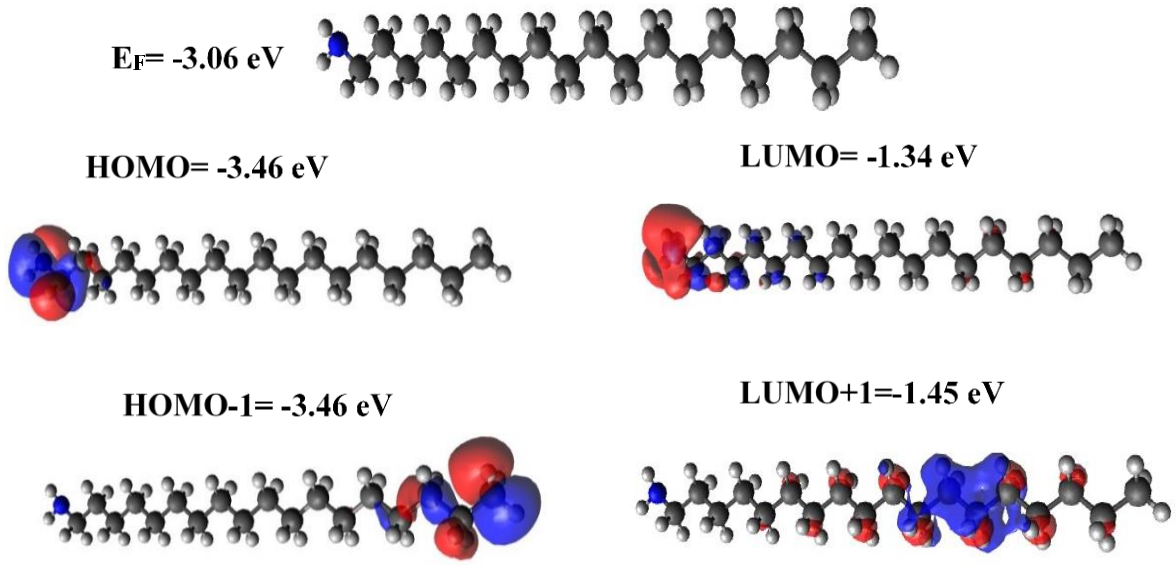


**Figure 4.6**: Wave function for monolayer **3** ($C_{18}$). **Top panel**: fully optimised geometry of **3**. **Lower panel**: HOMO, LUMO, HOMO-1, LUMO+1 levels of monolayer **3**, along with their energies.

#### 4.4.1.4 Molecule 4

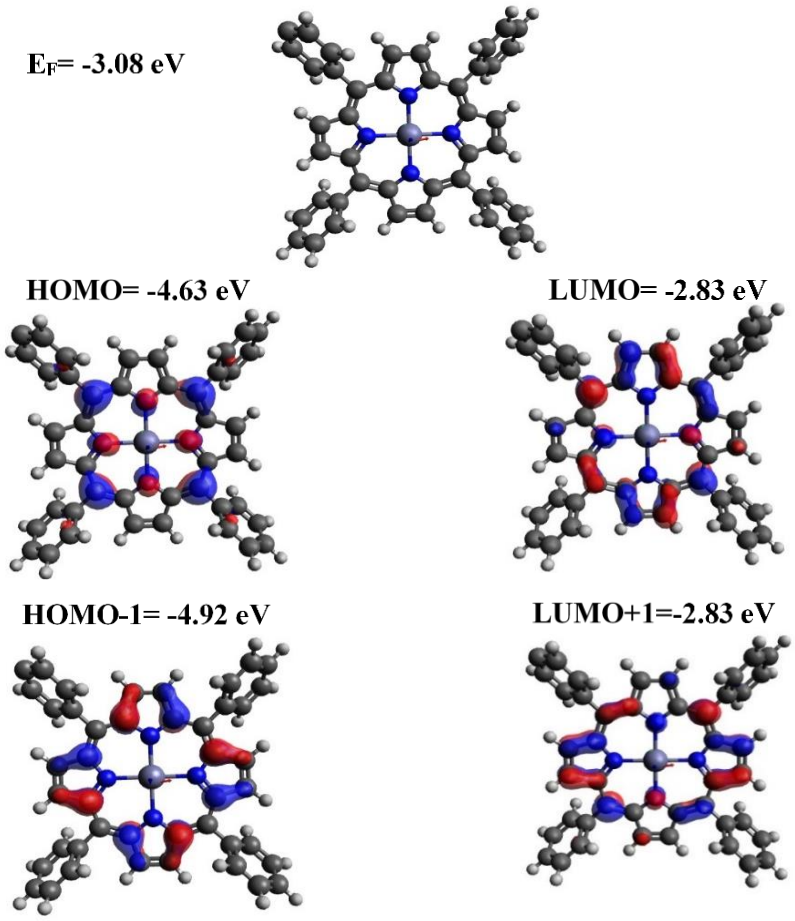


**Figure 4.7**: Wave function for monolayer **4** (ZnTPP). **Top panel**: fully optimised geometry of **4**. **Lower panel:** HOMO, LUMO, HOMO-1, LUMO+1 levels of monolayer **4,** along with their energies.

#### 4.4.1.5 Molecule 5

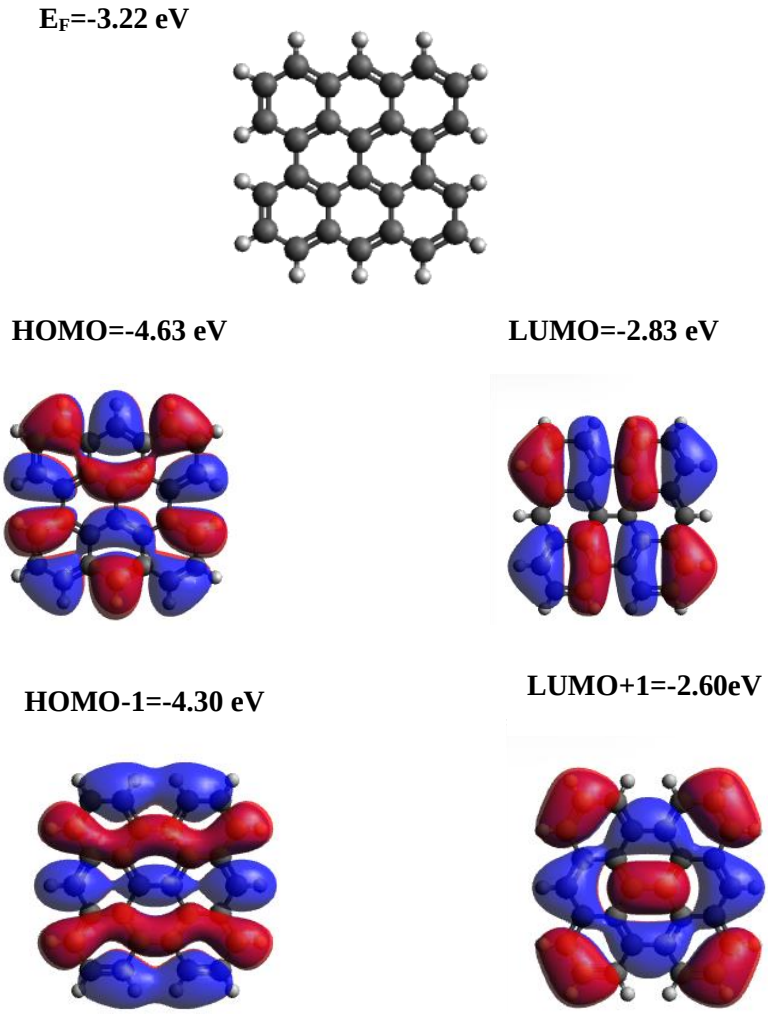


**Figure 4.8**: Wave function for monolayer **5. Top panel**: fully optimised geometry of **5**. **Lower panel**: HOMO, LUMO, HOMO-1, LUMO+1 levels of monolayer **5**, along with their energies.

#### 4.4.1.6 Molecule 6

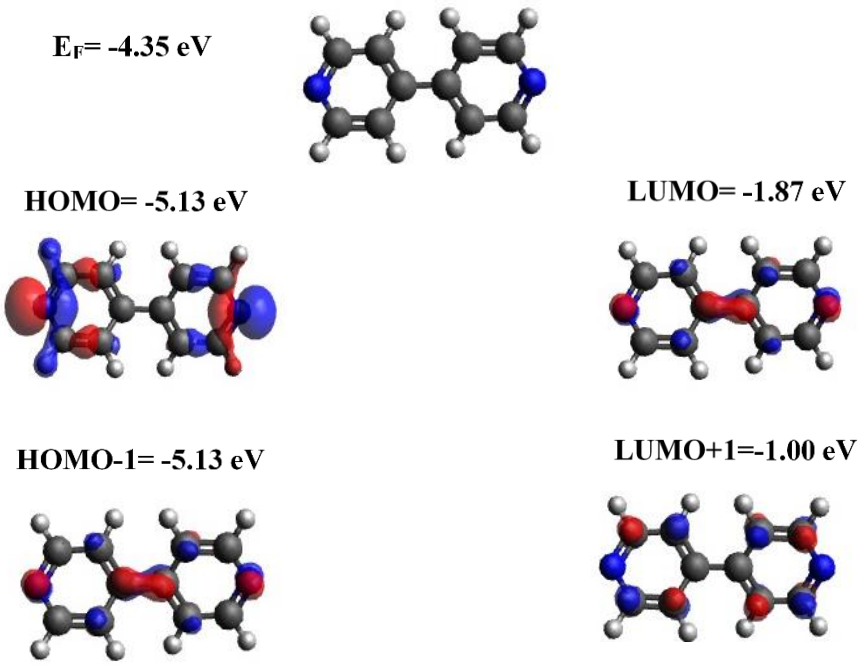


**Figure 4.9**: Wave function for monolayer **6. Top panel**: fully optimised geometry of **6**. **Lower panel**: HOMO, LUMO, HOMO-1, LUMO+1 levels of monolayer **6**, along with their energies.

#### 4.4.1.7 Molecule 7

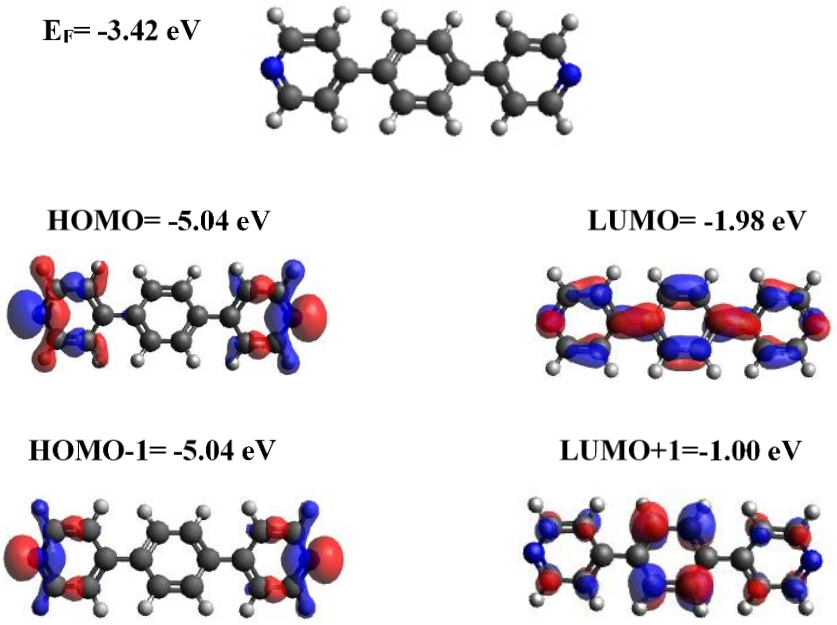


**Figure 4.10**: Wave function for monolayer **7. Top panel**: fully optimised geometry of **7**. **Lower panel**: HOMO, LUMO, HOMO-1, LUMO+1 levels of monolayer **7**, along with their energies.

#### 4.4.1.8 Molecule 8

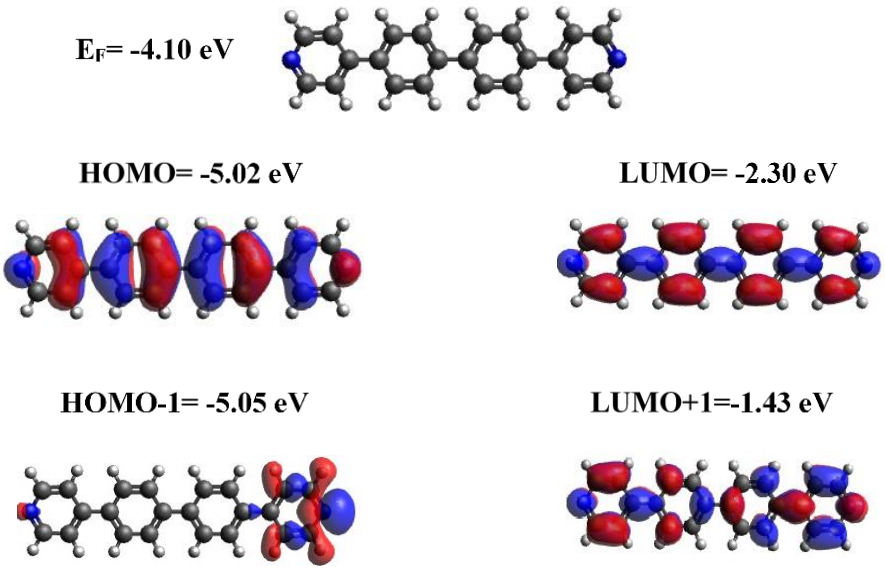


**Figure 4.11**: Wave function for monolayer **8. Top panel**: fully optimised geometry of **8**. **Lower panel**: HOMO, LUMO, HOMO-1, LUMO+1 levels of monolayer **8**, along with their energies.

### 4.4.2 Bilayer Compounds

The next step is to calculate the wave functions of the bilayers, which are formed from two molecules, mainly ZnTTP (**4**) combined with **6, 7,** and **8**, as follows:

#### 4.4.2.1 Bilayer 1

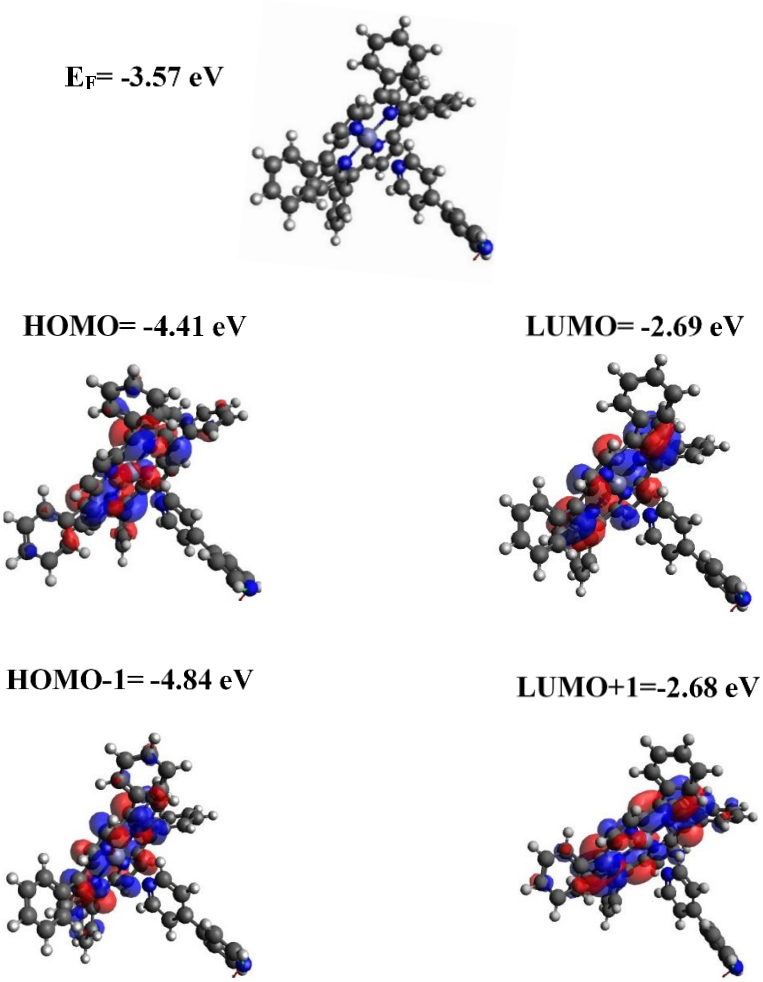


**Figure 4.12**: Wave function for bilayer **4/6. Top panel**: fully optimised geometry of **4/6**. **Lower panel**: HOMO, LUMO, HOMO-1, LUMO+1 levels of bilayer **4/6**, along with their energies.

#### 4.4.2.2 Bilayer 2

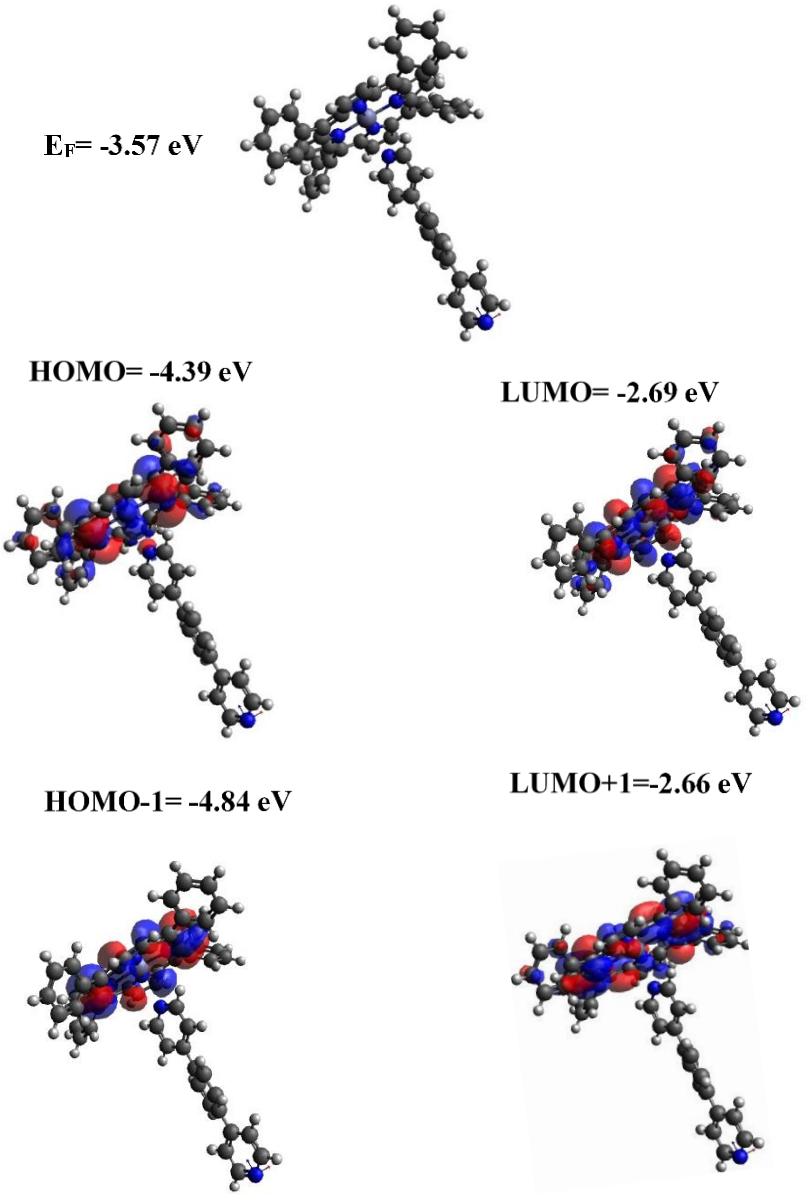


**Figure 4.13**: Wave function for bilayer **4/7. Top panel**: fully optimised geometry of **4/7**. **Lower panel**: HOMO, LUMO, HOMO-1, LUMO+1 levels of bilayer **4/7**, along with their energies.

#### 4.4.2.3 Bilayer 3

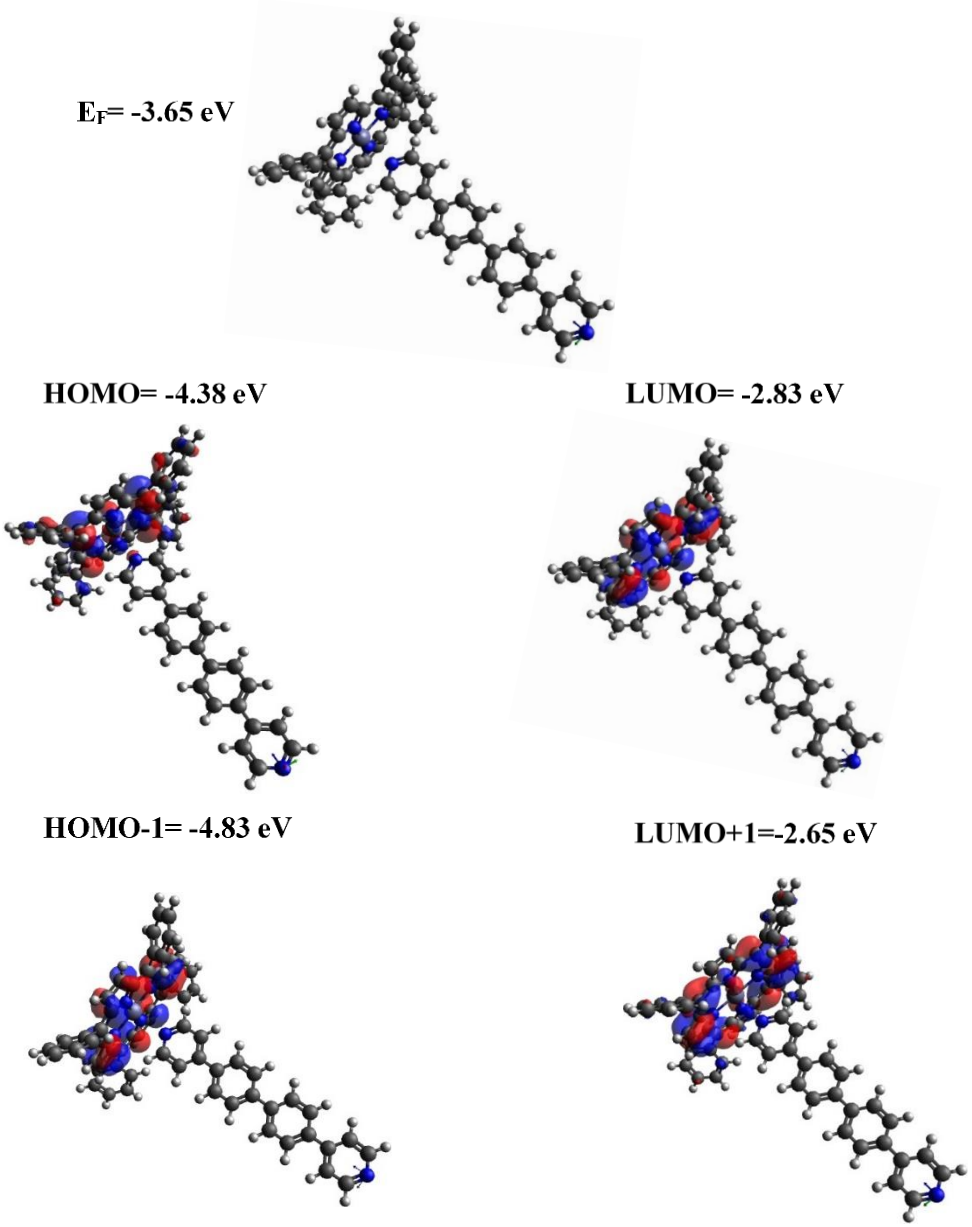


**Figure 4.14**: Wave function for bilayer **4/8**. **Top panel**: fully optimised geometry of **4/8**. **Lower panel**: HOMO, LUMO, HOMO-1, LUMO+1 levels of bilayer **4/8**, along with their energies.

### 4.5. Binding Energies using the Counterpoise Method

As mentioned in chapter 2, when computing binding energies as a function of some parameter, such as the distance between two components of a junction, a major problem is the interaction energies in neighboring atoms due to the overlap of their basic functions. This effect, which is called the basis set superposition error (BSSE) [25-26], increases as the atoms orientate themselves closer, thereby creating an effectively varying basis set as the parameter changes. These errors can be removed by applying the counterpoise correction as it is described in section 2.7.3 of chapter 2. If A and B are two-components of a junction, their binding energy is described as follows,

$$\Delta E(AB) = E^{AB} - (E^{A} + E^{B}) \tag{4.1}$$

where $E^{AB}$is the total energy for the dimer systems A and B, $E^{A}$ and $E^{B}$ are the energies of the isolated systems A and B. To remove errors, the same total basis set is used in each of the three calculations by including 'ghost' states; (basis set functions that have no electrons or protons). The following equation captures this technique:

$$\Delta E(AB) = E_{AB}^{AB} - (E_{A}^{AB} + E_{B}^{AB}) \tag{4.2}$$

Where $E_{A}^{AB}$ and $E_{B}^{AB}$ are the energies of systems $A$ and $B$ evaluated using the same basis of the dimer *AB*.

### 4.5.1 Binding Energies of Bilayer Compounds

In this section, the binding energies of bilayer structures are computed to find the optimum distance between the molecular components. Figure 4.15 shows the binding energy of the bilayer molecule ZnTTP (Py -ZnTPP), as a function of the separation between the two molecular components. The optimum distance corresponds to the binding-energy minimum and is found to be 2.3 Å, at approximately 0.5 eV. It should be noted that bilayers **4/6**, **4/7** and **4/8** all have approximately the same optimum binding energy and distance as in all case the pyridyl binds to Zn atom.

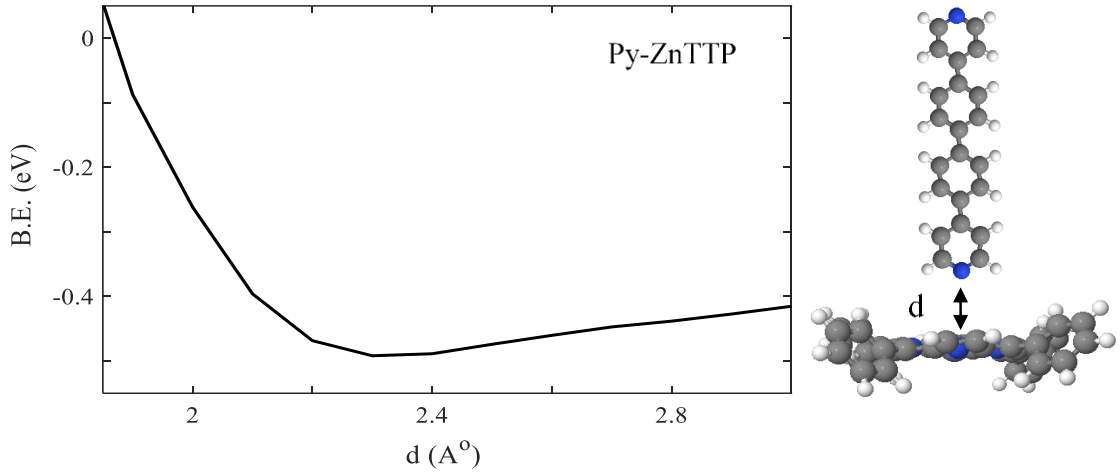


**Figure 4.15: Right panel**: represents pyridyl-based molecule with 2Py anchors and (Zn-TPP). **Left panel**: Binding energy versus distance plot of (Py-Zn-TTP). The equilibrium distance (i.e. the minimum of the binding energy curve) is found to be approximately 2.3 Å, for py-Zn. Key: C = grey, H = white, N = blue, Zn = light blue.

### 4.5.2 Binding Energies on a Gold Surface

In this section, the optimum distances between the Au electrode and three different molecules shown in Figures 4.16-4.18 were calculated. Figure 4.16 shows that the optimum distance between the Au electrode and $CH_2$ terminated molecule **2** is found to be about 2.3 Å, at approximately -1.0 eV. The $CH_2$ anchor possesses a strong bond to the under-coordinated gold electrode compared to other anchors such as an amine. Figure 4.17 indicates that the optimum distance between the Au electrode and pyridyl-terminated molecule **8** is found to be about 2.3 Å, at approximately -0.4 eV. The Py anchor possesses a weaker bond to an under-coordinated gold-electrode atom compared to other anchors, such as direct carbon. Figure 4.18 demonstrates the optimum distance between the ZnTTP molecule **4** and an under-coordinated gold atom to be around 2.9 Å, at approximately -0.5 eV.

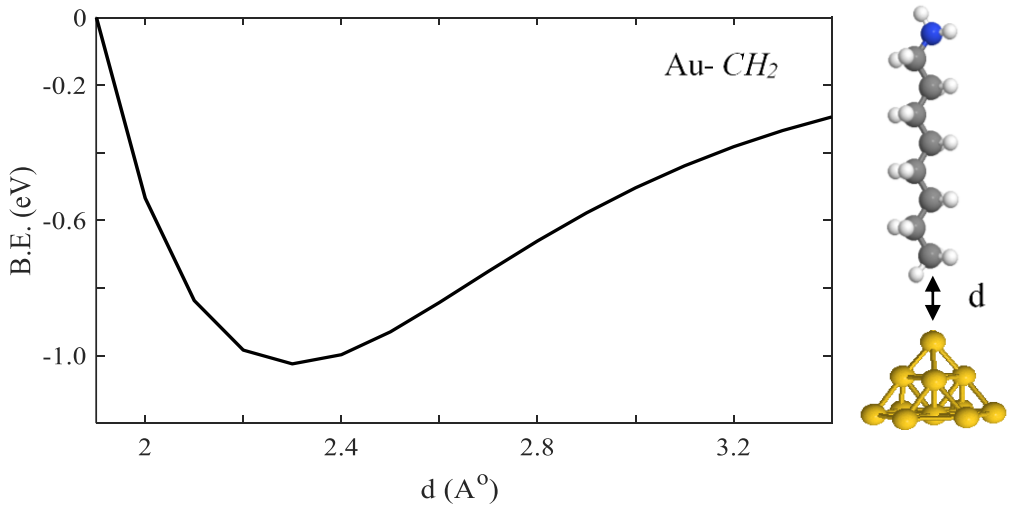


**Figure 4.16: Right panel**: representation a molecule **2** terminated with a direct carbon anchor on a gold tip. **Left panel**: Binding energy of C8 alkyl chain molecule to gold as a function of molecule-contact distance. The equilibrium distance (i.e. the minimum of the binding energy curve) is found to be approximately 2.3 Å, for Au-direct carbon. Key: C = grey, H = white, N = blue, Au = dark yellow.

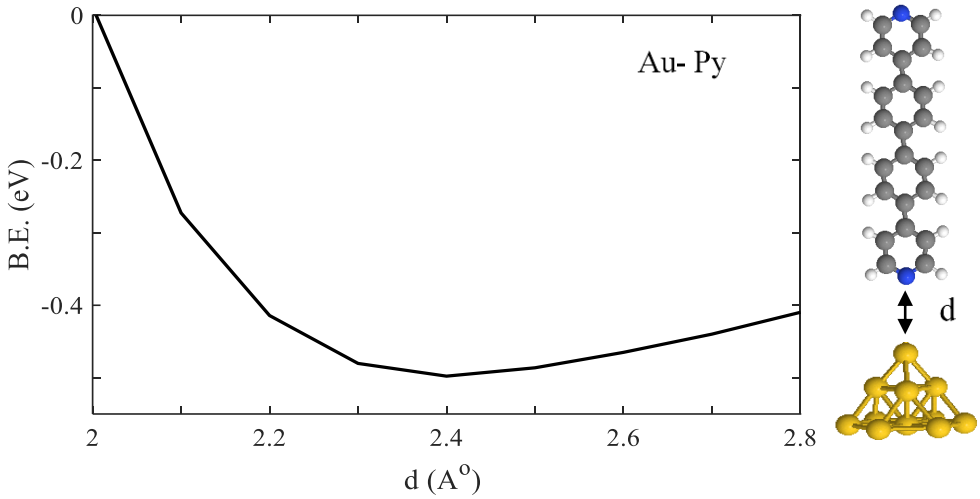


**Figure 4.17**: **Right panel**: represents molecule **8** binding to a gold ad-atom. **Left panel**: Binding energy of molecule **8** to gold as a function of molecule-contact distance. The equilibrium distance (i.e. the minimum of the binding energy curve) is found to be approximately 2.3 Å, for Au-Py. (Key: C = grey, H = white, N = blue, Au = dark yellow.

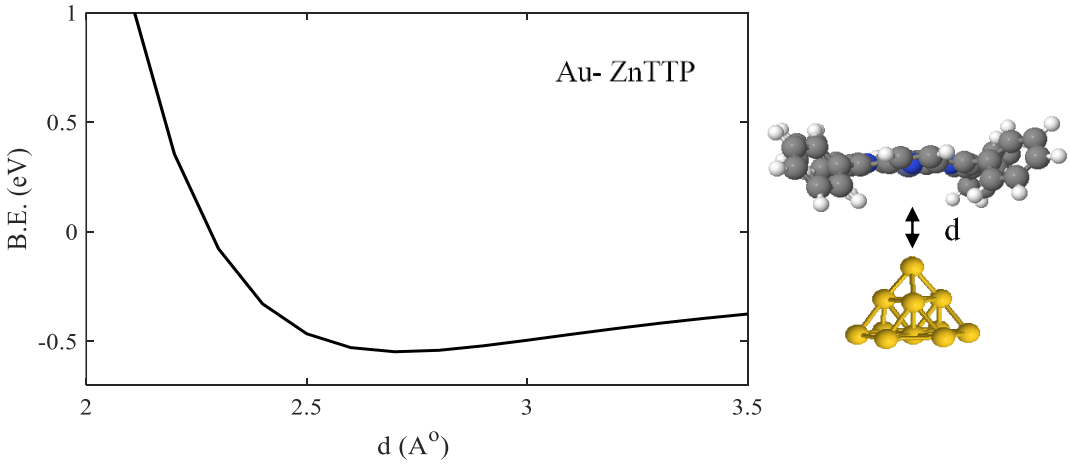


**Figure 4.18: Right panel**: represents molecule **4** binding to gold ad-atom. **Left panel**: Binding energy of molecule **4** to gold as a function of molecule-contact distance. The equilibrium distance (i.e. the minimum of the binding energy curve) is found to be approximately 2.9 Å, for Au-Zn. Key: C = grey, H = white, N = blue, Zn = light blue, Au = dark yellow.

Table 4.1 summaries the optimum separation distances d and binding energies (B.E.) of 4 different structures. The rows labelled Au-$CH_2$, Au-Py, and Au-ZnTTP show the optimum separation distances and their corresponding binding energies of the monolayer/ bilayers bound to an Au substrate, while the row labelled Py-ZnTTP shows the optimum separation distance and its corresponding binding energy of the bilayer in the absence of a Au surface. Based on these calculations, the $CH_2$ anchor possesses the stronger bond to the under-coordinated gold electrode compared to other anchors, while the Py anchor has the weakest bond.

**Table 4.1:** Summarizes binding energies (B.E), and optimum distances ($d$), calculations for mono/bilayers that bind to under-coordinated gold electrode with different anchor groups.

| Anchor groups | $d$ (Å) | B.E (eV) |
|---|---|---|
| Au-$CH_2$ | 2.3 | 1.00 |
| Au-Py | 2.3 | 0.40 |
| Au-ZnTTP | 2.9 | 0.50 |
| ZnTTP-Py | 2.3 | 0.50 |

### 4.6 Optimised DFT Structures of Molecular Junctions

Using the optimized structures and geometries for the compounds obtained as described above, I again employed the SIESTA code (for more detail see section 2.7 in chapter 2) to calculate self-consistent optimized geometries, ground state Hamiltonians and overlap matrix elements for the gold-molecule-gold junction. After relaxation, I calculated the electrical conductance and Seebeck coefficient. for alkyl chains **1-3** and phenyl ring derivatives **6-8** with different anchor groups including pyridyl, $CH_2$ , $NH_2$ and large anchors such as ZnTTP. These single-molecules or bilayer molecules are sandwiched between two gold electrodes first, then between gold and single-layer graphene sheet (SLG), which I will discuss thoroughly in chapter 5.

#### 4.6.1 Simulations of Au-single-molecule-Au junctions.

In this section, gold-optimised molecule-gold junctions involving **1, 2, 3** (see panel **A**), and **4, 5** (panel **B**) are shown in Figure 4.19.

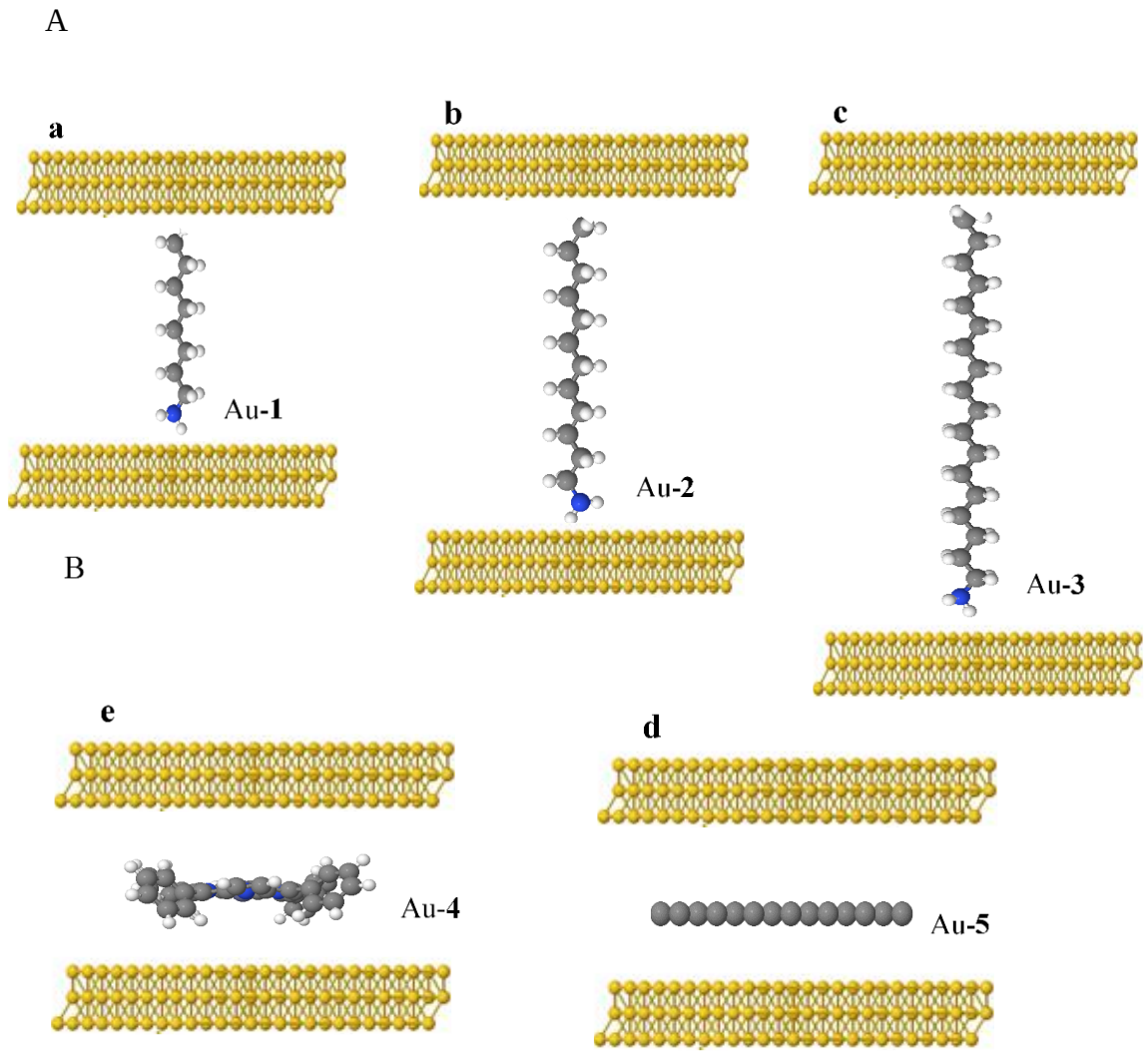


**Figure 4.19**: A schematic figure of the Au-**mono**-Au junctions. Both contacts are Au electrodes. A: **a-c** are alkyl chains Au-**1-3**-Au monolayer junctions. While B: **d-e** are ZnTPP and Gr involving Au-**4**-Au, and A-**5**-Au respectively.

### 4.6.2 Simulations of Au-single-molecule-Au junctions.

In this section optimized gold-bilayer-gold junctions formed from the **4/6**, **4/7,** and **4/8** bilayers are shown in f-h of Figure 4.20.

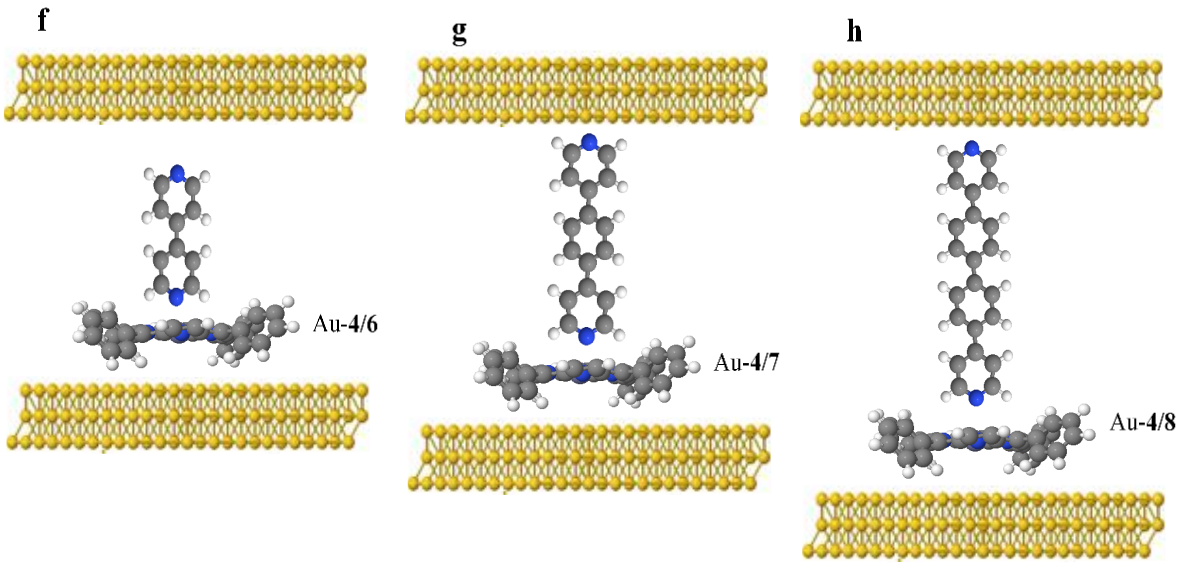


**Figure 4.20**: A schematic figure of the Au-bilayer-Au junctions. Both contacts are Au electrodes. **f**: Au-**4/6**-Au, **g**: Au-**4/7**-Au, **h**: Au-**4/8**-Au junctions.

### 4.7 Electric Transport Simulations

As a first step in carrying out transport calculations, the ground state Hamiltonian and optimized geometry of each compound were obtained using SIESTA. The generalised gradient approximation (GGA) exchange-correlation functional was used along with double zeta polarized (DZP) basis sets and the norm-conserving pseudopotentials. The real space grid was defined by a plane wave cut-off of 250 Ry. The geometry optimization was carried out to a force tolerance of 0.01 eV/Å. This process was repeated for a unit cell with the molecule placed between two electrodes, using the optimized distances between electrodes and the anchor groups shown in Table 4.1. From the ground state Hamiltonian, the transmission coefficient $T(E)$, and the room temperature electrical conductance $G$ were obtained, as described in the sections below.

#### 4.7.1.1Transport Simulations of Alkyl Chains Monolayers Au-1-3-Au

The transmission coefficient curves $T(E)$ were calculated for the single-molecule junctions using the Gollum transport code [27]. For alkyl chains in Au-**1-3**-Au junctions, Figure 4.21 demonstrates the relationship between the transmission coefficient and the length of alkane chains. As expected, the conductance decreases exponentially with increasing chain length from 8 to 18 - $CH_2$ units. The amount of the decrease in the conductance value is approximately constant and as follows $\log_{10}\frac{G}{G_0}$ = -4, -6, and -8. The transmission coefficients for the alkyl chains are shown in Figure 4.21.

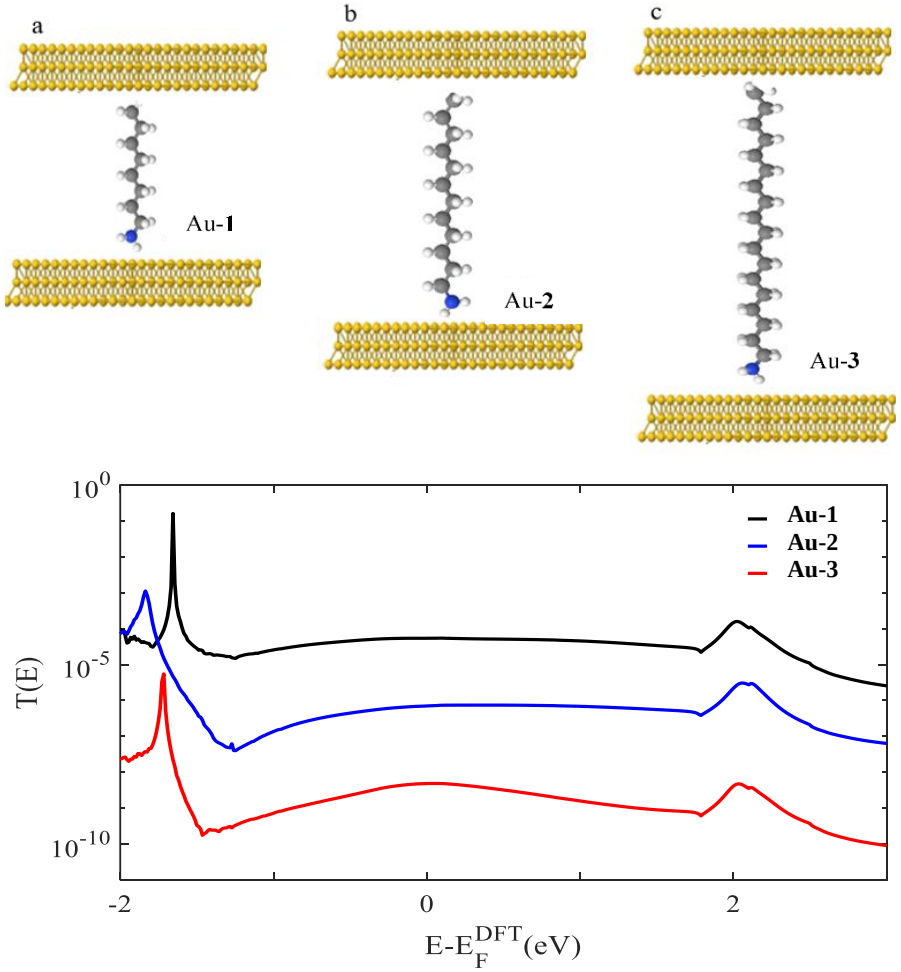


**Figure 4.21**: **Top panel**: represents alkyl chains monolayer junctions. **Bottom panel**: transmission coefficients *T(E)* curves of Au-**1-3**-Au junctions against electron energy E. Monolayers **1-3,** black, blue, and red curves respectively.

To test my theoretical simulations, I shall compare the DFT calculation against the experiment STM measurements. I managed to find two different experimental measurements of the alkyl chain $C_8$ and $C_{12}$ as shown in table 4.2. I refer to them as STM-1 [29], STM-2 [30]. I could not find STM measurements for alkyl chain $C_{18}$.

Table 4.2 shows how DFT simulations predict the conductance trends of these alkane chains. Additionally, it also demonstrates how the experimental measurements vary from one STM device to another due to many parameters, for instance, solvent, temperature and so on.

**Table 4.2**. Conductance of two STM measurements and my DFT simulations of linear alkyl chains. Simulations are taken at the DFT-predicted Fermi energy.

| Alkyl chain | DFT conductance $log(G/G°)$ | STM-1 conductance $log(G/G°)$ [29] | STM-2 conductance $log(G/G°)$ [39] |
|---|---|---|---|
| $C_8$ | -4.0 [this work] | -4.0 [29] | -5.0 [30] |
| $C_{12}$ | -6.0 [this work] | -5.0 [29] | -6.0 [30] |
| $C_{18}$ | -8.0 [this work] | - | - |

#### 4.8.1.2 Transport Simulation of a graphene-like molecule in an Au-Au Junction

In this section, I shall calculate the transmission coefficient of Au-**5**-Au which is a graphene-like molecule attached to the gold electrodes on both sides as shown in the top panel of Figure 4.22. The Fermi energy is considered approximately near the HOMO resonance thus, the charge transfer in the graphene sheet molecule is HOMO dominated. The value of the conductance is about $\log_{10}\frac{G}{G_0}$ =0.3 for the Au-**5**-Au

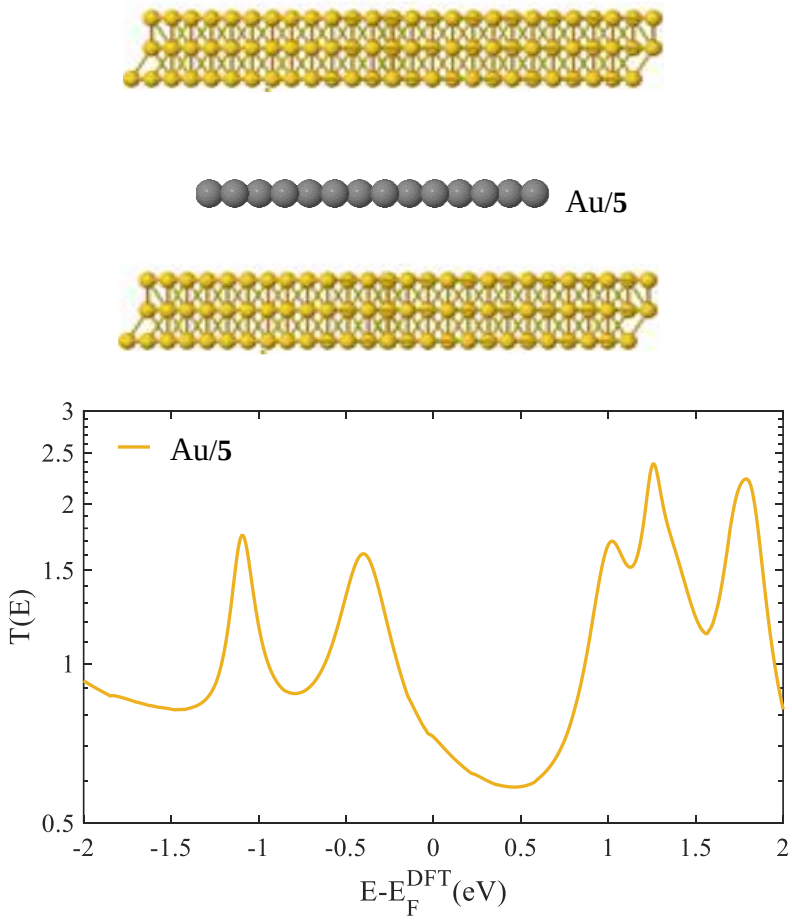


**Figure 4.22**: **Top panel:** Schematic illustrations of molecular junction for **Au-5-Au. Bottom panel**: transmission coefficient $T(E)$ of molecule **5** as a function of energy.

### 4.7.2 Spin-dependent Transport Calculations of single-molecule/bilayer Molecular Junctions

Spin-polarised calculations based on the density functional theory play a critical role in studying the structure-property relation in these metallic-molecular junctions based on their electronic structure [31]. Typically, the electron spin and the electronic orbital current are usually linked when an external magnetic field is applied to an electronic system [32]. Additionally, examining the effects of electron-vibration interactions on the spin-selective transport in dsDNA and enhancing the spin polarization to introduce a number of unique spin-splitting transmission modes in the HOMO-LUMO gap [33]. Here, I shall first calculate the spin-polarised transport for the monolayer Zinc tetraphenyl porphyrin (ZnTPP), molecule **4.** Then I shall connect the Porphyrin (ZnTPP**)**, to the pyridine-based molecules **6, 7, 8** and finally I shall I connected them to gold (111) electrodes, as shown in the top panel of Figures 4.23-4.26. The generalised gradient approximation (GGA) was combined with the transport code Gollum for these simulations. For all these junctions the LUMO resonance is located near the Fermi energy, which reveals these charge transport to be LUMO dominated as expected owing to the transmission of charge from the metal atom to the other molecules in the junctions. Spin up and spin down for these junctions are completely identical. The conductance values are $\log_{10}\frac{G}{G_0}$ = -3.0, -5.0, -6.0, and -7.0 respectively as illustrated in the bottom panels of Figures 4.23-4.26.

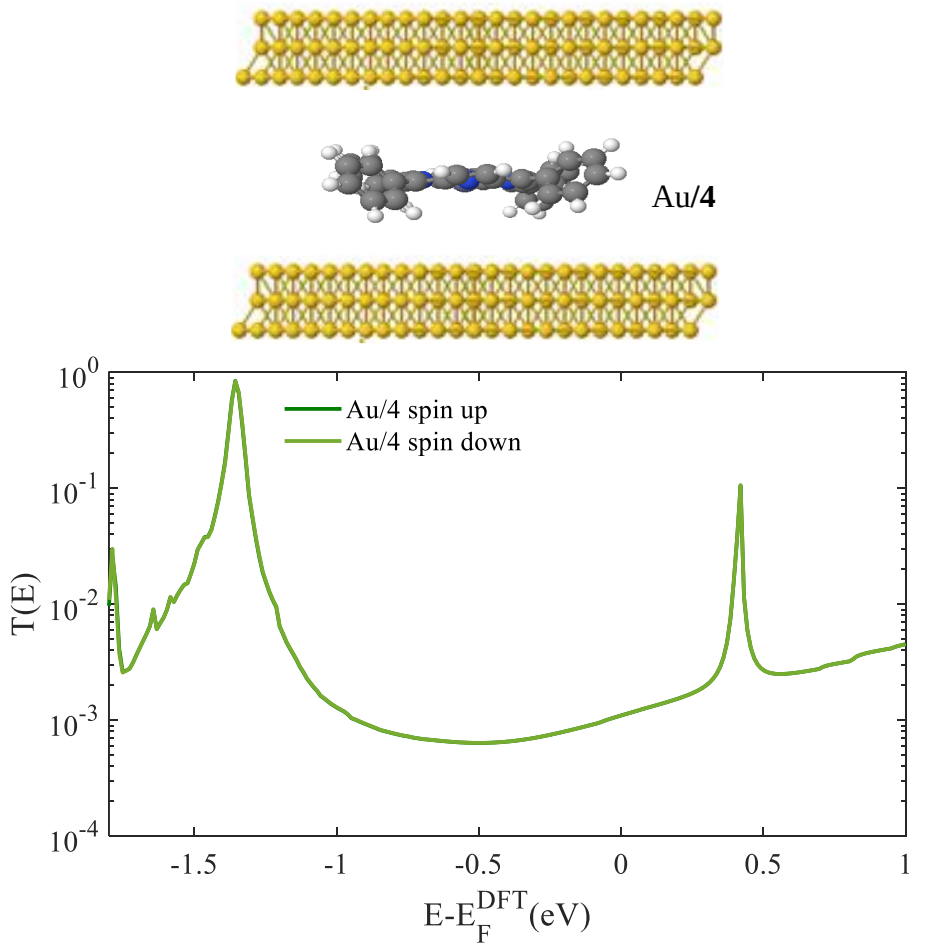


**Figure 4.23: Top panel:** Schematic illustrations of monolayer molecular junction for Au/**4**/Au. **Bottom panel:** Spin-polarised transmission coefficients, $T(E) = \frac{T_{up}(E)+T_{down}(E)}{2}$, of Au/**4**/Au junctions against electron energy E. Monolayer **4,** dark and light green curves represent spin up and down respectively.

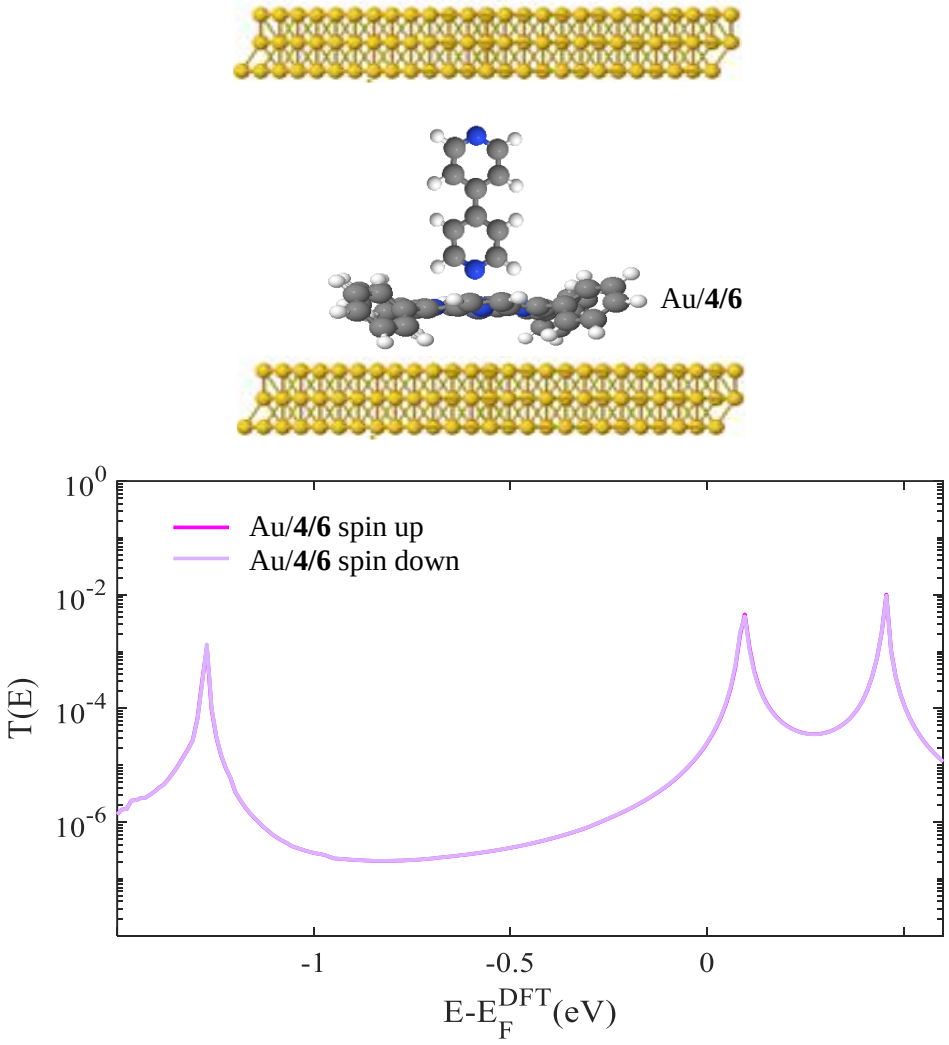


**Figure 4.24**: **Top panel:** Schematic illustrations of bilayer molecular junction for Au-**4/6**-Au. **Bottom panel**: Spin-polarised transmission coefficients, $T(E) = \frac{T_{up}(E)+T_{down}(E)}{2}$, of Au-**4/6**-Au junctions against electron energy E. bilayer **1,** dark and light purple curves represent spin up and down respectively.

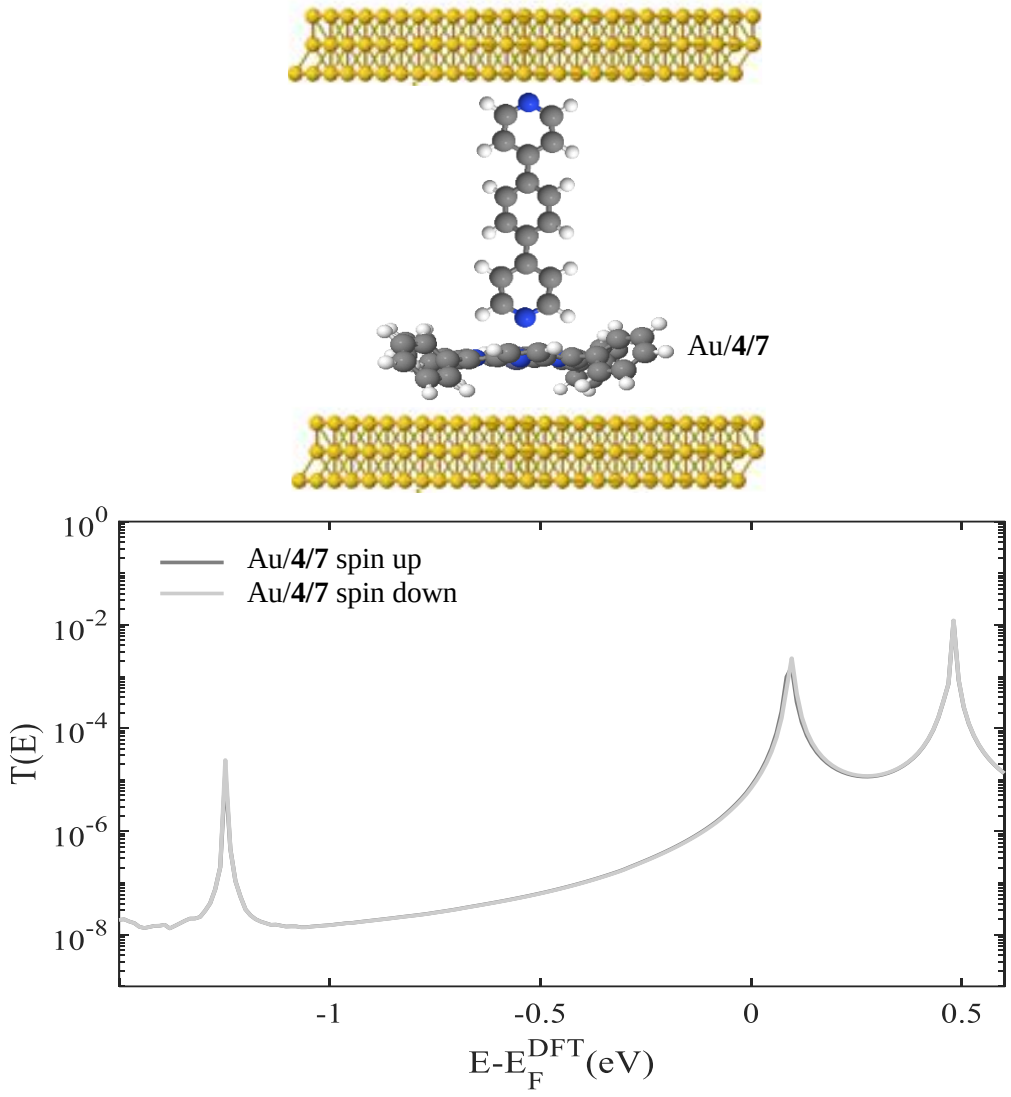


**Figure 4.25**: **Top panel**: Schematic illustrations of bilayer molecular junction for Au-**4/7**-Au. **Bottom panel** Spin-polarised transmission coefficients, $T(E) = \frac{T_{up}(E)+T_{down}(E)}{2}$, of Au-**4/7**-Au junctions against electron energy E. bilayer **2,** dark and light grey curves represent spin up and down respectively.

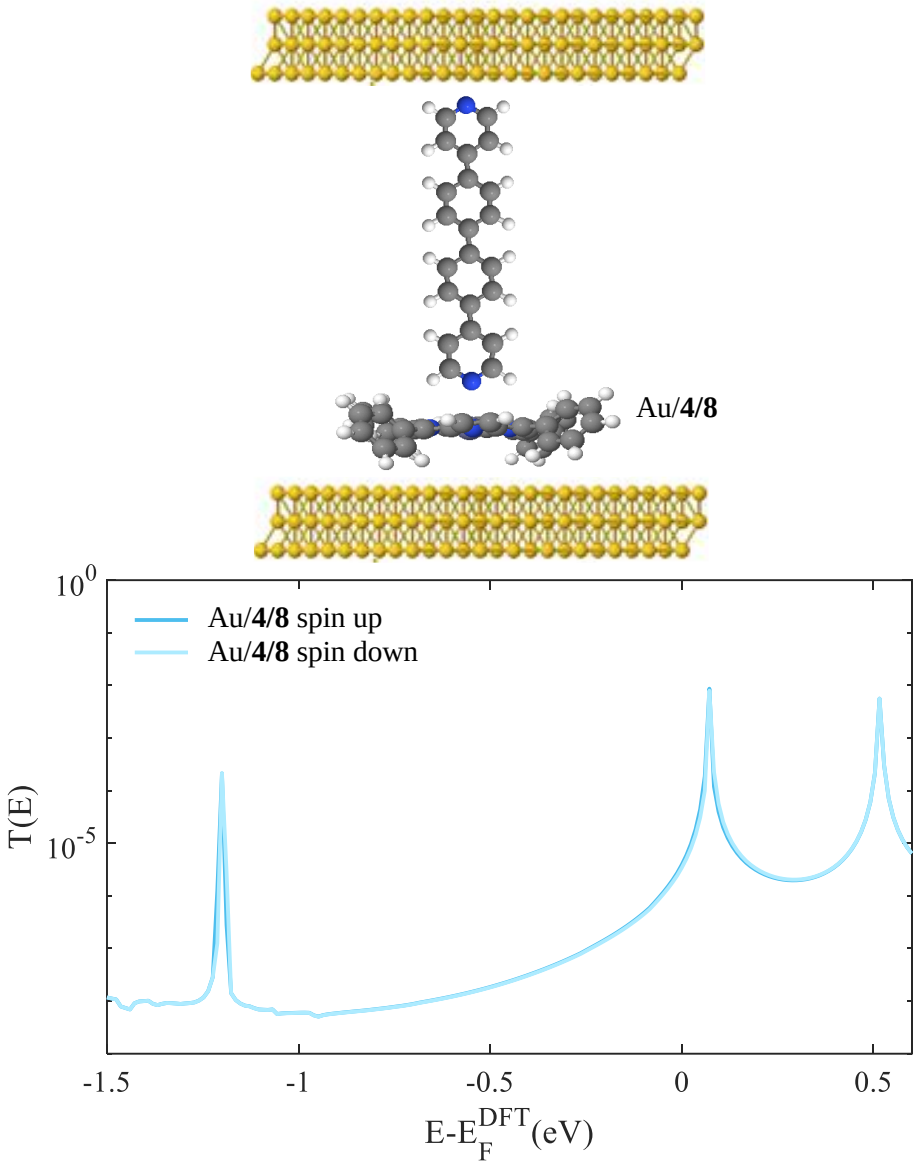


**Figure 4.26: Top panel**: Schematic illustrations of bilayer molecular junction for Au-**4/8**-Au. **Bottom panel**: Spin-polarised transmission coefficients, $T(E) = \frac{T_{up}(E)+T_{down}(E)}{2}$, of Au-**4/8**-Au junctions against electron energy E. bilayer **3,** dark and light blue curves represent spin up and down respectively.

### 4.8 Thermopower Calculations

After computing the electronic transmission coefficient for the single molecule/bilayer junctions, I now compute their Seebeck coefficients $S$ as described in chapter 3. To calculate the thermopower of the studied molecular junctions, it is useful to introduce the non-normalized probability distribution $P(E)$ defined by

$$P(E) = -T(E)\frac{df(E)}{dE} \tag{4.2}$$

where $f(E)$ is the Fermi-Dirac function and $T(E)$ is the transmission coefficients and whose moments $L_i$ are denoted as follows

$$L_i = \int dEP(E)(E - E_F)^i \tag{4.3}$$

where $E_F$ is the Fermi energy. The Seebeck coefficient, $S$, is then given by

$$S(T) = -\frac{1}{eT}\frac{L_1}{L_0} \tag{4.4}$$

where $e$ is the electronic charge.

The formula evaluated by Gollum code is

$$S^e(T) = \frac{-1}{eT}\frac{L_1}{\mathrm{L_0}} \tag{4.5}$$

where $L_i = \int dEP(E)(E - E_F)^i$

and $P(E) = -T(E)\frac{df(E)}{dE}$

For bilayers, 1 use expression, $T(E) = \frac{T_{up}(E)+T_{down}(E)}{2}$, where $T_{up}(E)$ and $T_{down}(E)$ are transmission coefficients for the separate spin channels and it is assumed that there is no spin-flip scattering. This equation describes the linear response regime and is consistent with

Onsager reciprocal relations. It is apparent that the Seebeck coefficient is proportional to the slope of the logarithm of the transmission coefficient at the Fermi level. Therefore, by raising the slope of $logT(E)$ near $E = E_F$ S is improved. In general, depending on the direction of the slope of the transmission function at the Fermi energy $E_F$ , the value of S can either be positive or negative. This originates from the structure of the charge carriers: *S* is positive for transport that is hole-dominated and negative for transport that is electron-dominated [34-35]. To calculate the Seebeck coefficient for the single molecule/bilayer junctions as shown in Figures 4.27-4.32 I used DFT combined with the quantum transport code Gollum. I shall calculate the Seebeck coefficient in two different junctions including Au-Au and then, SLG-Au which will be investigated in chapter 5.

#### 4.8.1.1 Thermopower Simulations for Monolayer alkyl Chains in Au-Au Junctions

As previously mentioned, the sign and value of the Seebeck coefficient $S$ are determined by the slope of the transmission coefficient *T(E)*. Figure 4.27 shows the Seebeck coefficients *S* of single alkyl chains evaluated at room temperature involving **1, 2, 3**, where $E_F$ is placed at approximately the middle of the HOMO-LUMO gap. The sign of $S$ is found to be a negative for the Au-**1**-Au, Au-**2**-Au. And Au-**3**-Au junctions are -.0.5, -3.0, and -1.6 $\mu V/K$ respectively as shown in Figure 4.27.

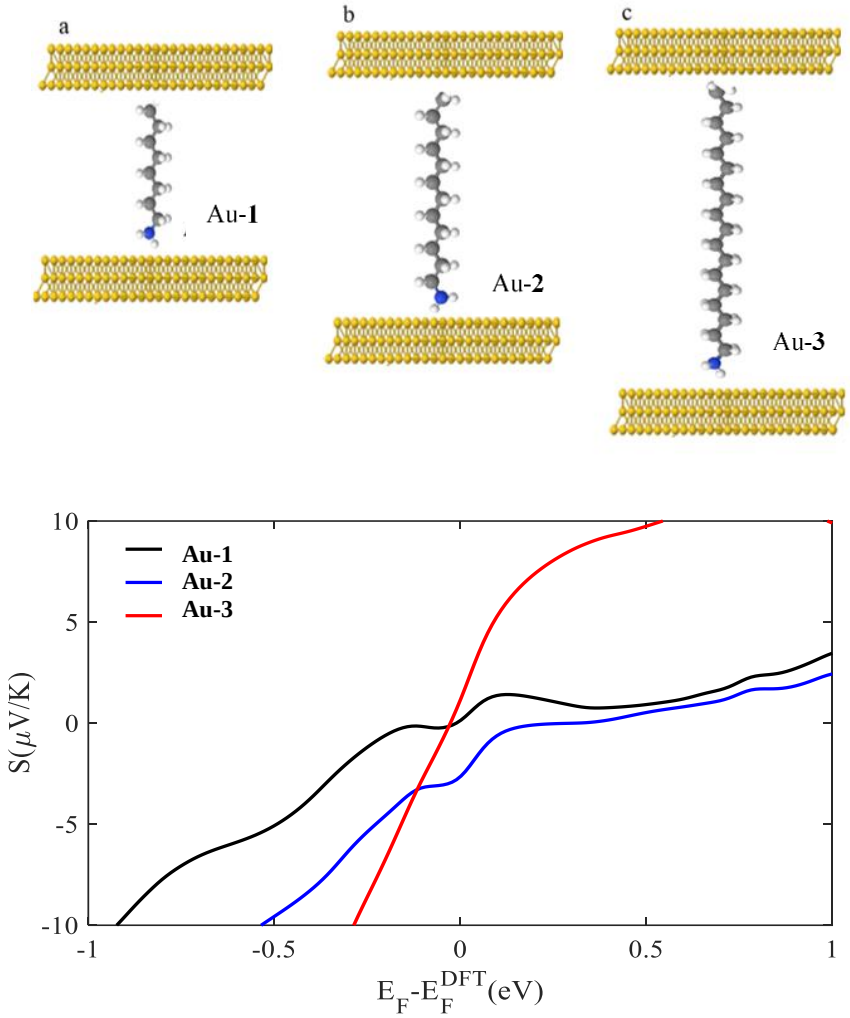


**Figure 4.27**: **Top panel**: Schematic illustrations of monolayer molecular junctions for the alkyl chains Au-**1**-Au, Au-**2**-Au, and Au-**3**-Au**. Bottom panel**: Seebeck coefficient *S* as a function of Fermi energy of three alkyl chain. Seebeck coefficients of monolayers **1, 2** and **3,** black, blue and red curves respectively.

### 4.8.1.2 Thermopower Simulations for Graphene-like molecule in a Au-Au Junction

Figure 4.28 illustrates the Au-**5**-Au graphene-like molecule sandwiched between two gold electrodes. Due to the fact that this junction yields a transmission coefficient that is a HOMO-dominated, the Seebeck sign is positive at the DFT-predicted Fermi $E\text{-}E_F^{DFT}$=0 eV

The value of $S$ for the Au-**5**-Au is found to be 4.0 μV/K.

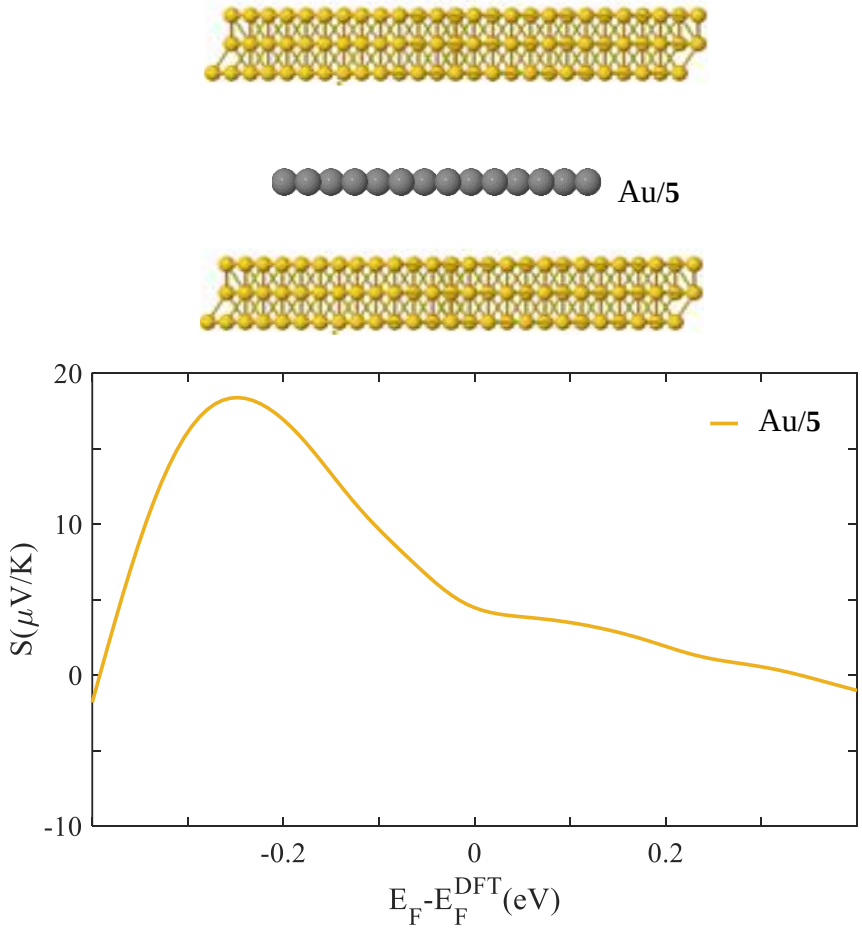


**Figure 4.28**: **Top panel**: Schematic illustrations of Gr molecular junction Au-**5**-Au. **Bottom panel**: Seebeck coefficient S as a function of Fermi energy of graphene sheet. Seebeck coefficient of monolayer **5** (Gr), orange curve.

### 4.8.2 Spin-polarised Thermopower Calculations of mono/bilayer Molecular Junctions

In this section, spin polarised calculations were carried out, due to the presence of a metal atom in the porphyrin molecule. Since these molecules are LUMO-dominated, the Seebeck coefficient for mono/bilayer molecules **4, 4/6, 4/7,** and **4/8** is discovered to be negative at the DFT-predicted Fermi E-$E_F^{DFT}$=0 eV as shown in figures 4.29-4.32. The values of $S$ are – (8.0) $\mu V/K$ for Au-**4**-Au, while for the Au-**4/6**-Au, Au-**4/7**-Au, and Au-**4/8**-Au junctions, they are – (225+227) , – (233+247) and – (236+238)( $\mu V/K$)

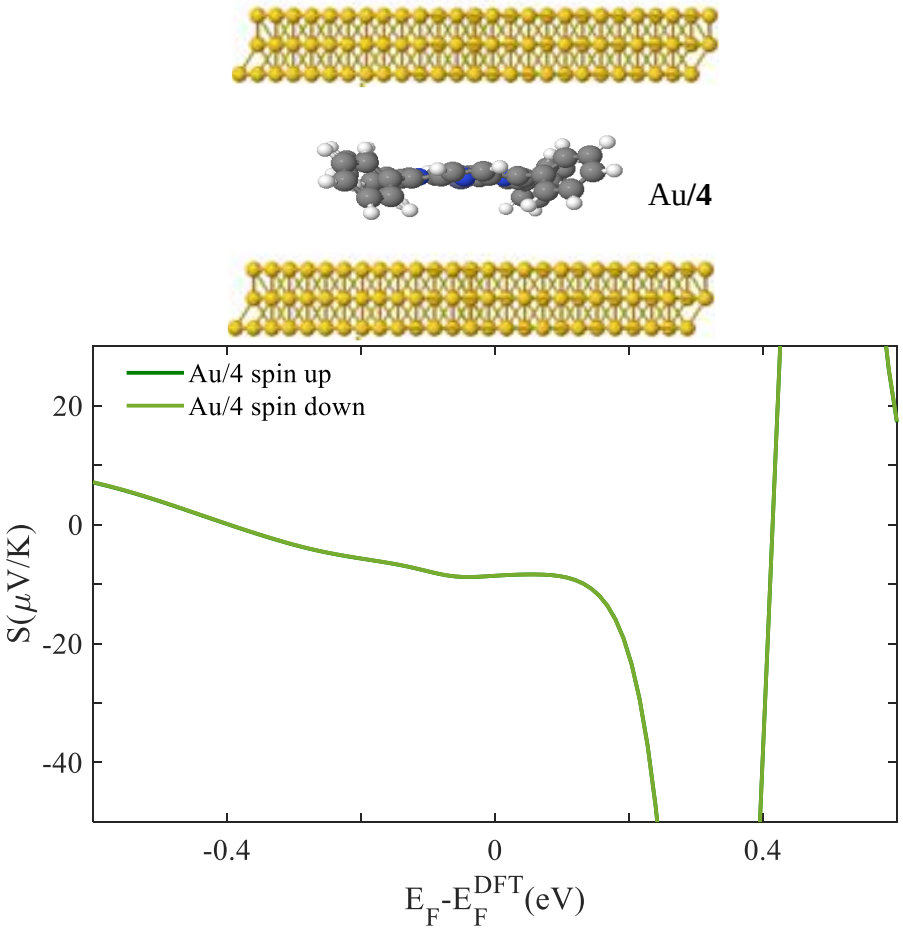


**Figure 4.29**: **Top panel**: Schematic illustrations of monolayer molecular junction for the Au/**4**/Au. **Bottom panel**: Seebeck coefficient S as a function of Fermi energy of ZnTTP. Seebeck coefficients of monolayer **4,** dark and light green curves represent the spin up and down curves.

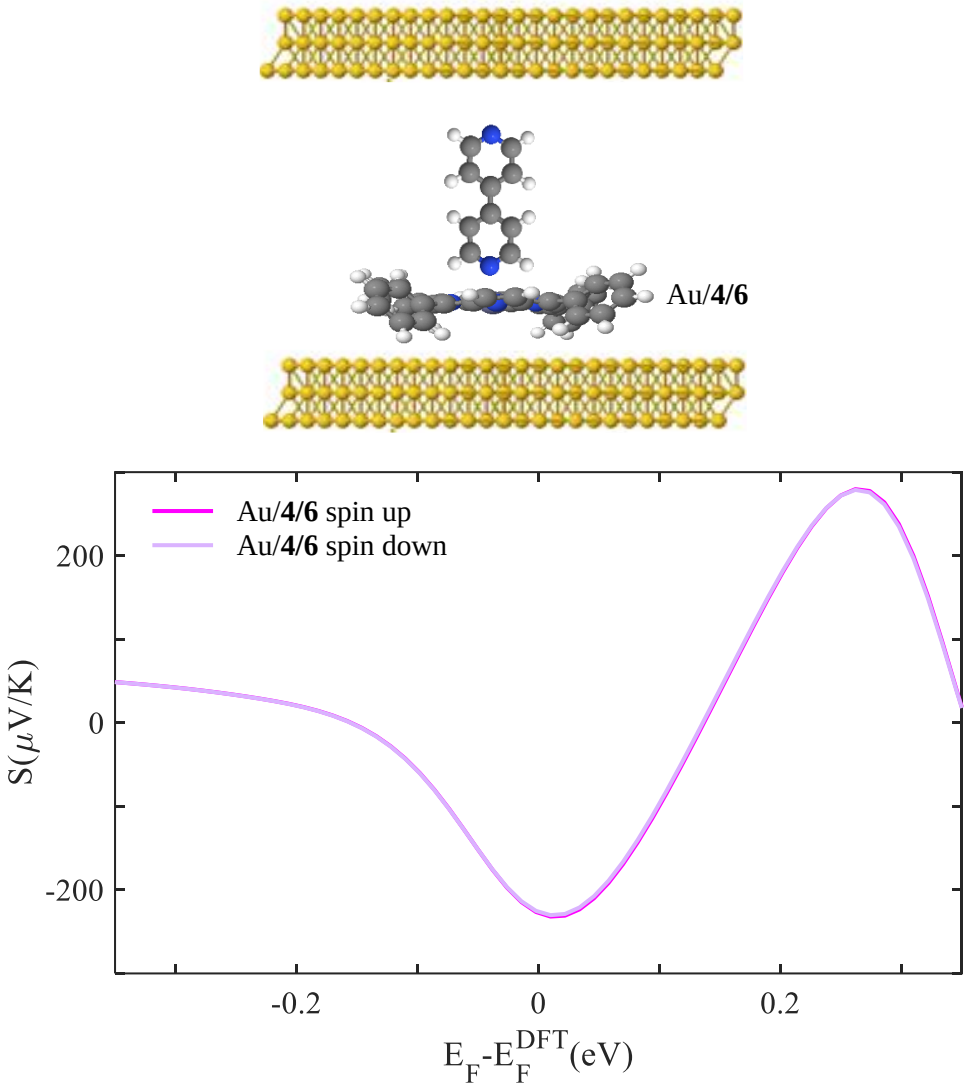


**Figure 4.30: Top panel**: Schematic illustrations of bilayer molecular junction for the Au-**4/6-**Au. **Bottom panel** Seebeck coefficient S as a function of Fermi energy of bilayer **1**. Seebeck coefficients of bilayer **4/6,** dark and light purple curves represent the spin up and down curves.

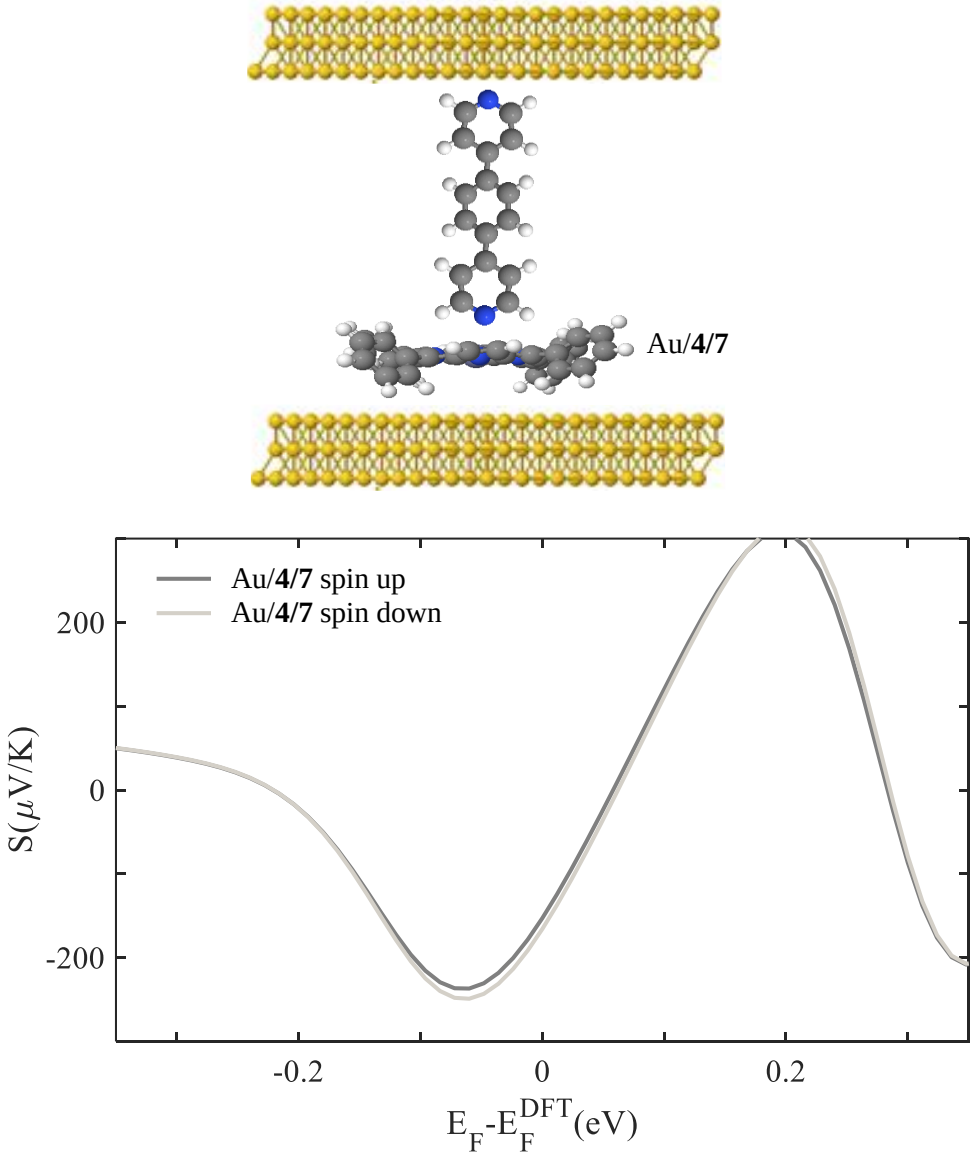


**Figure 4.31**: **Top panel**: Schematic illustrations of bilayer molecular junction for the Au-**4/7**-Au. **Bottom panel** Seebeck coefficient S as a function of Fermi energy of bilayer **2**. Seebeck coefficients of bilayer **4/7,** dark and light grey curves represent the spin up and down.

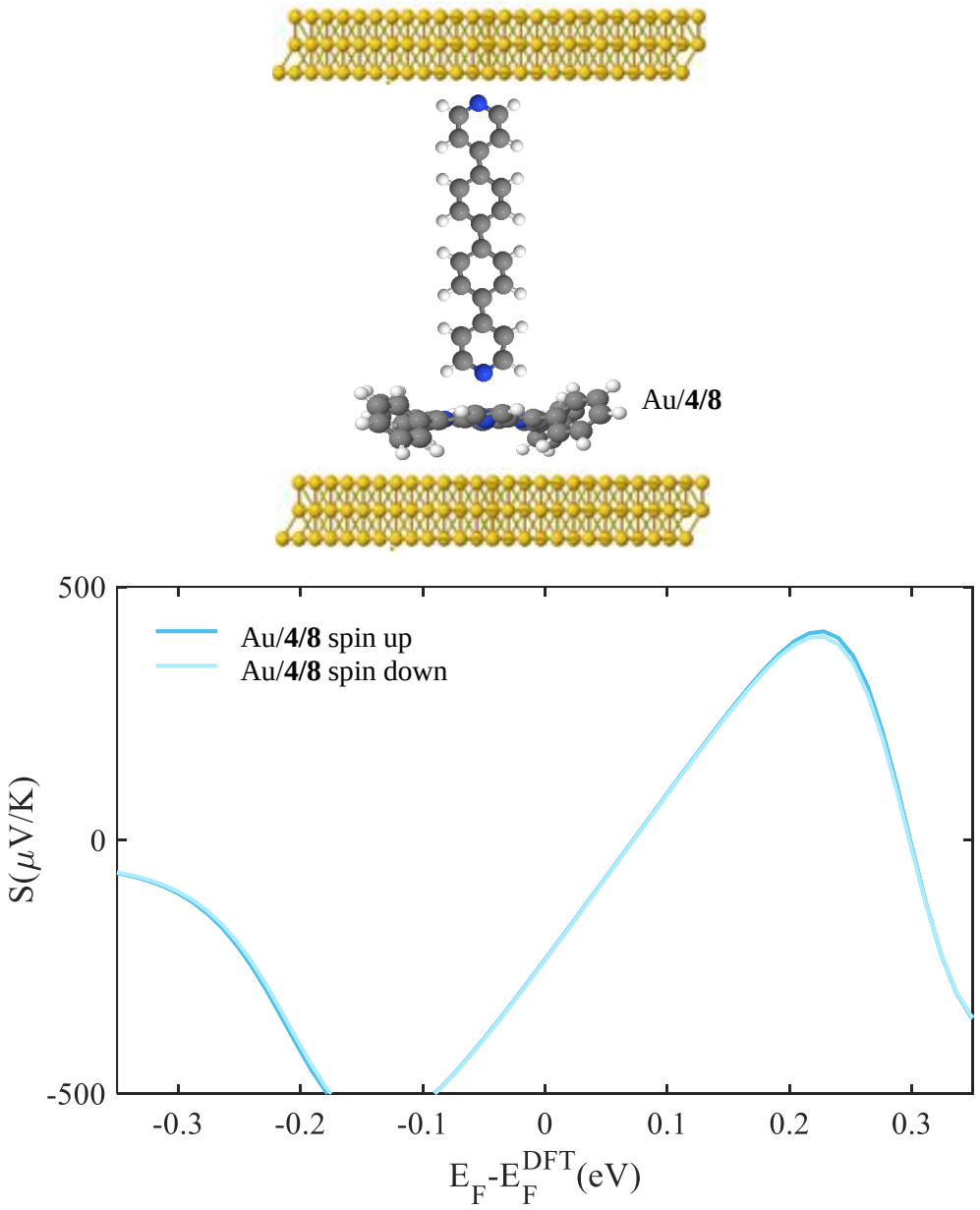


**Figure 4.32**: **Top panel**: Schematic illustrations of bilayer molecular junction for the Au-**4/8**-Au. **Bottom panel** Seebeck coefficient S as a function of Fermi energy of bilayer **3**. Seebeck coefficients of bilayer **4/8,** dark and light blue curves represent the spin up and down.

To summarise the above Seebeck coefficient calculations are collected in table 4.3. The alkyl chains Au-**1**-Au, Au-**2**-Au, and Au-**3**-Au have negative sign because the transport is LUMO dominated. Molecule **4** has negative sign of Seebeck coefficients sign of Seebeck coefficients is negative due to the Fermi level being closer to LUMO than to the HOMO.

**Table 4.3**: DFT simulations of Seebeck coefficient $S$ at DFT-predicted Fermi E-$E_F^{DFT}$=0 eV for both mono/bilayer structures in Au – Au junctions.

| Mono/bilayer junctions | $S\ (\mu V/K)$ | Polarization state |
|---|---|---|
| Au-**1**-Au | -0.5 | == |
| Au-**2**-Au | -3.0 | == |
| Au-**3**-Au | -1.6 | == |
| Au-**4**-Au | -8.0 | == |
| Au-**5**-Au | 4.0 | == |
| Au-**4/6**-Au | -(225, 227) | up and down |
| Au-**4/7**-Au | -(233, 247) | up and down |
| Au-**4/8**-Au | -(236, 238) | up and down |

## 4.9. Conclusion

The investigations in this chapter modelled the thermoelectric proprieties of the single-molecule and bilayer junctions by employing density functional theory. As a first step I studied the frontier orbitals for both single-molecule and bilayer structures involving 4 different anchors such as direct carbon, amine, pyridine, and Zn-contact**.**

The isolated surface plots of the 4 different anchor groups illustrate different behaviors of localized and delocalized weights on the HOMO and LUMO orbitals. The binding energy of the 4 different anchor groups, which bind to the gold electrode have been also investigated. The DFT results show that the direct carbon has the strongest binding among the 4 anchors. Secondly, the charge transport simulations for single-molecule and bilayer structures that bind to gold electrodes have been explored. The theoretical results demonstrate that for the 3-alkyl chains, the Fermi energy ($E-E_F^{DFT}=0$ eV) is placed approximately in the mid-gap between the HOMO and LUMO resonances. While for the bilayers, the transmission coefficient is LUMO dominated at Fermi energy ($E-E_F^{DFT}=0$ eV). Finally, I simulated the thermopower calculations of the single-molecule and bilayer structures in Au-Au junctions. The Seebeck coefficients show different behavior for these junctions, and I shall discuss them in more detail in chapter 5.

## 4.11 Bibliography


1. Aviram, A. (1989). Molecular electronics—science and technology. Angewandte Chemie International Edition in English, 28(4), 520–521. doi:10.1002/anie.198905201
2. Das, S., Lee, B. H., Linstadt, R. T., Cunha, K., Li, Y., Kaufman, Y., … Ahn, B. K. (2016). Molecularly smooth self-assembled monolayer for high-mobility organic field-effect transistors. Nano Letters, 16(10), 6709–6715. doi: 10.1021/acs.nanolett.6b03860
3. Wang, X., Ismael, A., Ning, S., Althobaiti, H., Al-Jobory, A., Girovsky, J., … Ford, C. J. (2022a). Electrostatic Fermi level tuning in large-scale self-assembled monolayers of oligo(phenylene–ethynylene) derivatives. Nanoscale Horizons, 7(10), 1201–1209. doi:10.1039/d2nh00241h
4. Kang, B., Lee, S. K., Jung, J., Joe, M., Lee, S. B., Kim, J., … Cho, K. (2018). Nanopatched graphene with molecular self-assembly toward graphene–Organic HybridSoftElectronics. Advanced Materials, 30(25). doi:10.1002/adma.201706480
5. Arcadia, C. E., Kennedy, E., Geiser, J., Dombroski, A., Oakley, K., Chen, S.-L., … Rosenstein, J. K. (2020). Multicomponent molecular memory. Nature Communications, 11(1). doi:10.1038/s41467-020-14455-1
6. Wang, X., Bennett, T. L., Ismael, A., Wilkinson, L. A., Hamill, J., White, A. J., … Lambert, C. J. (2020). Scale-up of room-temperature constructive quantum interference from single molecules to self-assembled molecular-electronic films. Journal of the American Chemical Society, 142(19), 8555–8560. doi:10.1021/jacs.9b13578

7. Miao, R., Xu, H., Skripnik, M., Cui, L., Wang, K., Pedersen, K. G., … Linke, H. (2018). Influence of quantum interference on the thermoelectric properties of molecular junctions. Nano Letters, 18(9), 5666–5672. doi:10.1021/acs.nanolett.8b02207

8. Nichols, R. J., & Higgins, S. J. (2016). Single Molecule Nano electrochemistry in electrical junctions. Accounts of Chemical Research, 49(11), 2640–2648. doi:10.1021/acs.accounts.6b00373

9. Almughathawi, R., Hou, S., Wu, Q., Liu, Z., Hong, W., & Lambert, C. (2020). Conformation and quantum-interference-enhanced thermoelectric properties of diphenyl diketopyrrolopyrrole derivatives. ACS Sensors, 6(2), 470–476. doi:10.1021/acssensors.0c02043

10. Bennett, T. L., Alshammari, M., Au-Yong, S., Almutlg, A., Wang, X., Wilkinson, L. A., … Long, N. J. (2022). Multi-component self-assembled molecular-electronic films: Towards new high-performance thermoelectric systems. Chemical Science, 13(18), 5176–5185. doi:10.1039/d2sc00078d

11. Ismael, A., Al-Jobory, A., Wang, X., Alshehab, A., Almutlg, A., Alshammari, M., … Lambert, C. (2020a). Molecular-scale thermoelectricity: As simple as ‘ABC.’ Nanoscale Advances, 2(11), 5329–5334. doi:10.1039/d0na00772b

12. Han, B., Li, Y., Ji, X., Song, X., Ding, S., Li, B., … Hu, W. (2020). Systematic modulation of charge transport in molecular devices through facile control of molecule–electrode coupling using a double self-assembled monolayer nanowire junction. Journal of the American Chemical Society. doi:10.1021/jacs.0c02215

13. Ramachandran, R., Li, H. B., Lo, W.-Y., Neshchadin, A., Yu, L., & Hihath, J. (2018). An electromechanical approach to understanding binding configurations in single-molecule devices. Nano Letters, 18(10), 6638–6644. doi:10.1021/acs.nanolett.8b03415

14. Escorihuela, E., Cea, P., Bock, S., Milan, D. C., Naghibi, S., Osorio, H. M., … Martin, S. (2020). Towards the design of effective multipodal contacts for use in the construction of Langmuir–Blodgett Films and molecular junctions. Journal of Materials Chemistry C, 8(2), 672–682. doi:10.1039/c9tc04710g

15. Yu, Z., Xu, Y., Su, J., Radjenovic, P. M., Wang, Y., Zheng, J., … Li, J. (2021). Probing interfacial electronic effects on single-molecule adsorption geometry and electron transport at atomically flat surfaces. Angewandte Chemie International Edition, 60(28), 15452–15458. doi:10.1002/anie.202102587

16. Qiu, X., Ivasyshyn, V., Qiu, L., Enache, M., Dong, J., Rousseva, S., … Chiechi, R. C. (2020). Thiol-free self-assembled oligoethylene glycols enable robust air-stable molecular electronics. Nature Materials, 19(3), 330–337. doi:10.1038/s41563-019-0587-x

17. Aradhya, S. V., Frei, M., Hybertsen, M. S., & Venkataraman, L. (2012). Van der waals interactions at metal/organic interfaces at the single-molecule level. Nature Materials, 11(10), 872–876. doi:10.1038/nmat3403

18. Wang, X., Sangtarash, S., Lamantia, A., Dekkiche, H., Forcieri, L., Kolosov, O. V., Robinson, B. J. (2022). Thermoelectric properties of organic thin films enhanced by π–π stacking. Journal of Physics: Energy, 4(2), 024002. doi:10.1088/2515-7655/ac55a3

19. Solano, M. V., Della Pia, E. A., Jevric, M., Schubert, C., Wang, X., van der Pol, C., Jeppesen, J. O. (2014). Mono- and bis(pyrrolo)tetrathiafulvalene derivatives tethered to C60: Synthesis, photophysical studies, and self-assembled monolayers. Chemistry–A European Journal, 20(32), 9918–9929. doi:10.1002/chem.201402623

20. Zhao, S., Chen, H., Qian, Q., Zhang, H., Yang, Y., & Hong, W. (2021). Non-covalent interaction-based molecular electronics with graphene electrodes. Nano Research, 16(4), 5436–5446. doi:10.1007/s12274-021-3687-2

21. Xiang, D., Wang, X., Jia, C., Lee, T., & Guo, X. (2016). Molecular-scale electronics: From concept to function. Chemical Reviews, 116(7), 4318–4440. doi:10.1021/acs.chemrev.5b00680

22. Wu, Q., Sadeghi, H., García-Suárez, V. M., Ferrer, J., & Lambert, C. J. (2017). Thermoelectricity in vertical graphene-C60-graphene architectures. Scientific Reports, 7(1). doi:10.1038/s41598-017-10938-2

23. Ismael, A. K., & Lambert, C. J. (2019). Single-molecule conductance oscillations in alkane rings. Journal of Materials Chemistry C, 7(22), 6578–6581. doi:10.1039/c8tc05565c

24. Herrer, I. L., Ismael, A. K., Milán, D. C., Vezzoli, A., Martín, S., González-Orive, A., Cea, P. (2018). Unconventional single-molecule conductance behavior for a new heterocyclic anchoring group: Pyrazolyl. The Journal of Physical Chemistry Letters, 9(18), 5364–5372. doi:10.1021/acs.jpclett.8b02051

25. Ismael, A., Wang, X., Bennett, T. L., Wilkinson, L. A., Robinson, B. J., Long, N. J., … Lambert, C. J. (2020). Tuning the thermoelectrical properties of anthracene-based self-assembled monolayers. Chemical Science, 11(26), 6836–6841. doi:10.1039/d0sc02193h

26. Ismael, A. K., Grace, I., & Lambert, C. J. (2017). Connectivity dependence of fano resonances in single molecules. Physical Chemistry Chemical Physics, 19(9), 6416–6421. doi:10.1039/c7cp00126f

27. Davidson, R. J., Milan, D. C., Al-Owaedi, O. A., Ismael, A. K., Nichols, R. J., Higgins, S. J., … Beeby, A. (2018). Conductance of 'bare-bones' tripodal molecular wires. RSC Advances, 8(42), 23585–23590. doi:10.1039/c8ra01257a

28. González, M. T., Ismael, A. K., García-Iglesias, M., Leary, E., Rubio-Bollinger, G., Grace, I., … Agraït, N. (2021). Interference controls conductance in phthalocyanine molecular junctions. The Journal of Physical Chemistry C, 125(27), 15035–15043. doi:10.1021/acs.jpcc.1c03290

29. Mokrousov, Y., Bihlmayer, G., & Blügel, S. (2005). Full-potential linearized augmented plane-wave method for one-dimensional systems: Gold nanowire and Iron Monowires in a gold tube. Physical Review B, 72(4). doi:10.1103/physrevb.72.045402

30. Zeller, R. (2006). Spin-polarized dft calculations and magnetism. Computational Nanoscience: Do It Yourself, 31, 419-445.

31. Du, G.-F., Fu, H.-H., and Wu, R. (2020). Vibration-enhanced spin-selective transport of electrons in the DNA double helix. Physical Review B, 102(3), 035431.

32. Sadeghi, H. (2019). Discriminating Seebeck sensing of molecules. Physical Chemistry Chemical Physics, 21(5), 2378–2381. doi:10.1039/c8cp05991h

33. Al-Khaykanee, M. K., Ismael, A. K., Grace, I., & Lambert, C. J. (2018). Oscillating seebeck coefficients in π-stacked molecular junctions. RSC Advances, 8(44), 24711–24715. doi:10.1039/c8ra04698k

# Chapter 5

### High Performance Thermoelectricity of Multicomponent Junctions

Organic thin films composed of highly ordered molecular arrays have great prospects in thermoelectric energy harvesting. Molecular arrays bound to graphene substrates via non-covalent interaction have shown better thermoelectric behavior compare with typical covalently bonded metal-thiolate arrays. Recently, thermoelectric properties of non-conjugated junctions, using graphene as a substrate, have been reported. However, conjugated oligo-aromatic molecules with small HOMO-LUMO gap is more attractive for energy-harvesting purposes.

In this work, my collaborators at Cavendish Laboratory, University of Cambridge and Dalian Maritime University demonstrate a method to fabricate an aromatic molecular array on a graphene substrate via multi-component method. They first immobilize zinc -cantered porphyrin on a graphene substrate by π-π stacking [1-2], and then modify it by attaching a conjugated pyridine backbone to the ZnTPP via a coordination bond as shown in figure 1(b). This stepwise building method separates the molecular backbones due to the large ZnTPP foot print and shows good thermopower with Seebeck coefficient up to ~51 μV/K. This value is higher than most of the reported Seebeck coefficients for molecular junctions and suggests a new route for approaching high-efficiency thermo-electric materials.

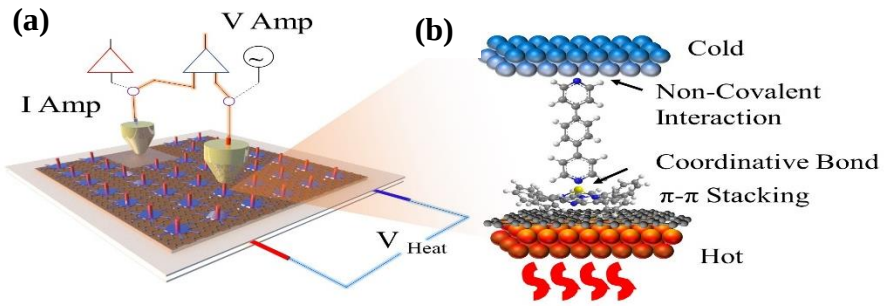


**Figure 5.1: (a)** Scheme of measurement system used in experiment work, **(b)** an example of multi-component structure in EGaIn junction [42].

## 5.1 Introduction

In molecular devices and thermoelectric energy harvesters, weak anchor-substrate coupling is desirable, because weak coupling can effectively suppress interfacial phonon transport [3] and molecular functional properties preserved, whereas they can be quenched due to strong interfacial coupling [4-5].

Although metallic substrates can form weak coupling junctions with molecules via noncovalent interactions, such junctions can be unstable at room temperature due to the high mobility of metal atoms [6-7]. To avoid this problem, graphene was recently used as a novel substrate for building-up non-covalent molecular junctions, and using pyrene[8-9] or amine[10-11] as an anchor group. Compared with their metal-thiolate derivatives, such junctions show a number of enhancements in performance, for example, they behave as a better electrical barrier [10], and exhibit better thermo-electric behavior [12]. Most of the recently published graphene/molecule junctions use alkyl chains as the backbone, but this type of backbone was not favored in device applications, because its large HOMO-LUMO gap suppresses the electron transport [13-14] and thermopower [15]. Molecules with large conjugation systems, such as oligo-phenyl structures, are therefore, more attractive for molecular electronic studies [16-17]. The past decades show that electrode material, which may be metallic or non-metallic,

has an important effect. The most frequently used conducting materials are Au [18], Ag [19], Pd, and Pt [20] as examples. Gold has been the most used electrode substance due to its qualities as a precious metal, including excellent chemical stability, high conductivity, and easy-to-clean surfaces and tips. However, there are several issues with gold electrodes, including the movement of surface ions at room temperatures brought by thermal fluctuations and instabilities [21]. Therefore, creating non-metallic electrodes such as carbon-based materials [22--23], graphene [24-25] and silicon [26] have inspired researchers to investigate the potential for producing accurate single-molecule electrical and thermal measurements with these types of electrodes. These display a variety of interesting features, such as high charge mobility, stability, mechanical strength, and flexibility of their - conjugated structure [22-23].

In this work, I present a new direction of research, where I can control the sign of the Seebeck coefficient by changing one of the electrode types to form asymmetric junction (i.e., Au-molecule-Gr). I find that the Seebeck coefficient changes sign for some, but not all junctions, depending on the organic components that are used in the junction [27].

## 5.2 Binding Energies

As explained in chapter 4 section 4.5, the counterpoise technique and DFT companion are used to compute binding energies and the optimum binding distance between two items by removing basis set superposition errors [28–29]. For more information about the counterpoise method, see section 2.7 in chapter 2.

### 5.2.1 Binding Energies on a Graphene Substrate

In this section, I calculate binding energies to find the optimum distance between the graphene substrate and different molecules as shown in Figures 5.1-5.4.

Figure 5.1 shows the binding energy as a function of the distance between the graphene sheet (Gr) and ZnTTP. The optimum distance (i.e., the minimum of the binding energy curve) is found to be approximately 4.0 Å and the optimum binding energy is 0.2 eV (single-molecule case). Figure 5.2 shows the binding energy as a function of the distance between the graphene sheet and **4/8** bilayer. In this case, the optimum distance (i.e., the minimum of the binding energy curve) is found to be approximately 4.0 Å, and the binding energy 0.15 eV (bilayer case). Similarly, Figure 5.3 shows the binding energy as a function of the distance between the graphene sheet and pyridyl anchor, where the optimum distance (i.e., the minimum of the binding energy curve) is found to be approximately 3.4 Å, and the binding energy 0.20 eV. I also calculated the optimum distance and binding energy between two graphene sheets as shown in Figure 5.4.

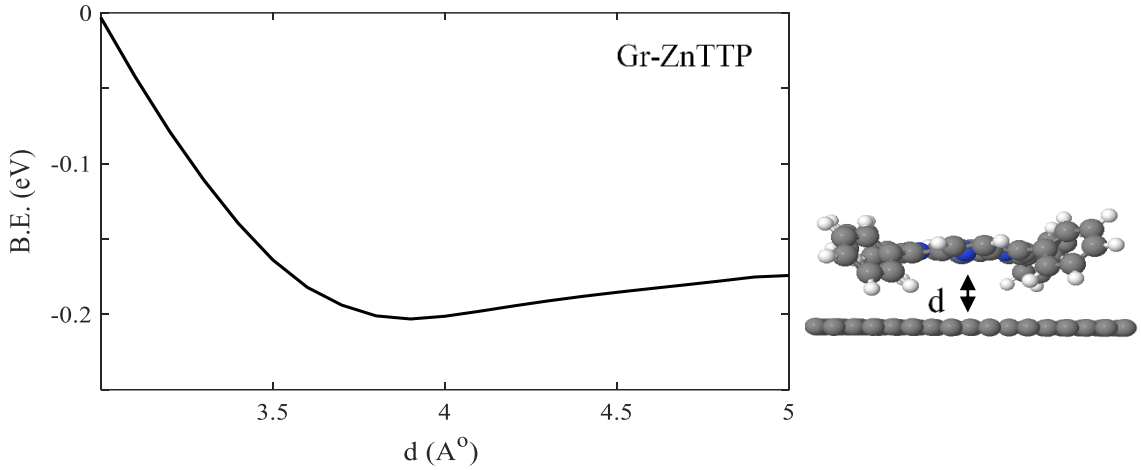


**Figure 5.2: Right panel:** represents the ZnTTP molecule binding to a graphene sheet. **Left panel**: Binding energy as a function of the optimum binding distance *d*, where *d* is found to be approximately 4.0 Å, and binding energy 0.2 eV, (single-molecule case).

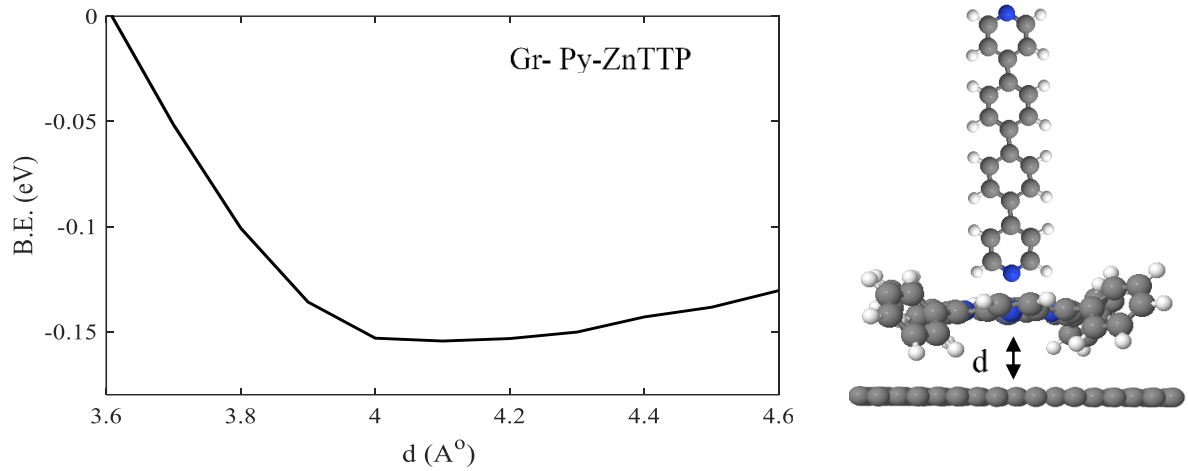


**Figure 5.3**: **Right panel**: represents bilayer **3** binding to a graphene sheet. **Left panel**: Binding energy as a function of the optimum binding distance $d$, where $d$ is found to be approximately 4.0 Å, and binding energy 0.15 eV, (bilayer case).

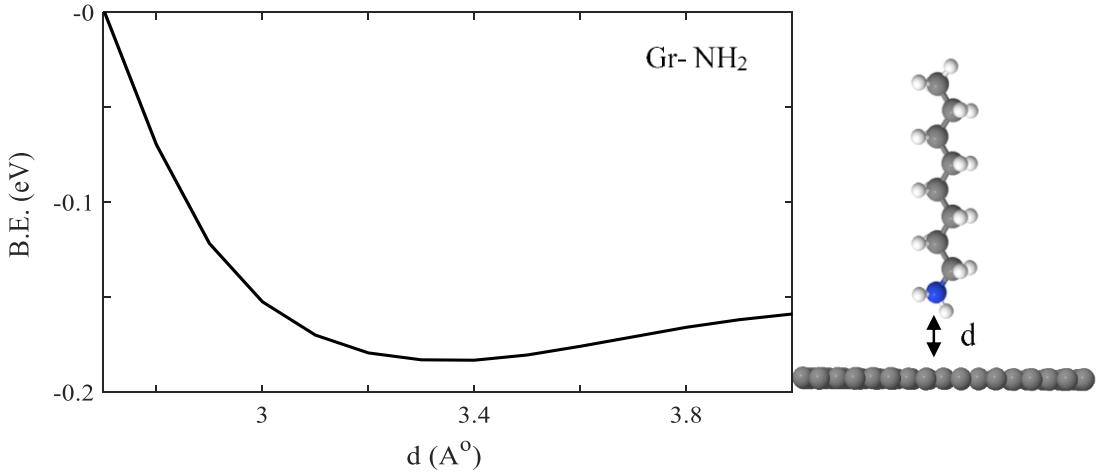


**Figure 5.4**: **Right panel:** represents molecule **1** binding to a graphene sheet. **Left panel**: Binding energy as a function of the optimum binding distance $d$, where $d$ is found to be approximately 3.4 Å, and binding energy B. E= 0.20 eV, (single-molecule case).

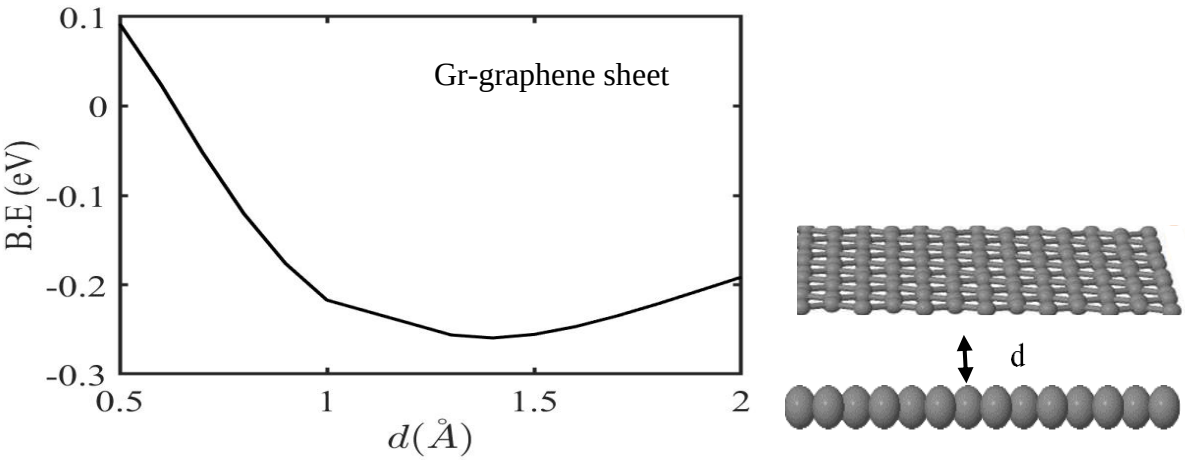


**Figure 5.5: Right panel:** represents molecule **5** binding to a graphene sheet. **Left panel**: Binding energy as a function of the optimum binding distance $d$, where $d$ is found to be approximately 1.4 Å, and binding energy B. E= 0.2 eV, (single-molecule case).

Table 5.1 represents the optimum separation distance and binding energy for four different anchor groups bound to a graphene electrode through either single-molecule or bilayer components. Figures 5.2-5.5 illustrate the binding energies for one end (specifically to a Gr sheet) of the asymmetric junction Au-M-Gr. The binding energies for the other end (Au), are already presented in chapter 4, (see Figures 4.15-4.18).

Table 5.1 also shows that these anchors bind more strongly to Au than the Gr sheet. This is expected as the stability of organic molecules on a gold substrate is reasonably higher than on graphene surface and my simulations predict the coupling to Au to be up 5 times stronger. Another reason for that is that the van der Waals interactions between organic molecules and graphene sheet are fairly week. My simulations here are well supported by the van der Waals interactions, for instance, ZnTTP binds to gold by 0.50 eV, whereas the same anchor binds to

graphene by 0.20 eV, and this suggests that ZnTTP is more likely to interact with a metallic surface than a non-metallic surface. One could notice that the direct carbon contact to Au surface is the strongest anchor among all the anchor-electrode contacts with binding energy of 1 eV.

**Table 5.1:** Summarizes all the binding energies and optimum distances calculations for mono/bilayers that bind to gold or graphene sheet. $d$ is the equilibrium distance and B.E is the corresponding minimum energy difference. (Au binding energy simulations were present in chapter 4).

| Contact point | $d$ (Å) | B.E (eV) |
|---|---|---|
| Gr-$NH_2$ | 3.4 | 0.20 |
| Gr-ZnTTP | 4.0 | 0.20 |
| Gr-bilayer | 4.0 | 0.15 |
| Gr-graphene | 1.4 | 0.2 |
| Au-$CH_2$ | 3.4 | 1.00 |
| Au-Py | 4.0 | 0.40 |
| Au-ZnTTP | 2.9 | 0.50 |
| ZnTTP-Py | 2.3 | 0.50 |

### 5.3 Optimised DFT Structures of Compounds in Their Junctions

Starting from the optimised structures and geometries for the compounds obtained as described in chapter 4 (Figures 4.1,4.2) I again employed the SIESTA code to calculate self-consistent optimised geometries, ground state Hamiltonians and overlap matrix elements. I then used the Gollum quantum transport code to calculate the transmission coefficient, and Seebeck coefficient S for graphene-molecule-gold junction. This section includes alkyl chains **1-3** and phenyl ring derivatives **6-8** with different anchor groups including pyridyl, $CH_2$, amine and large anchor such as ZnTTP**.** For more information about the studied components see chapter 4. These single molecules and bilayers are sandwiched between gold and a single layer graphene sheet (SLG).

#### 5.3.1 Gold- graphene (SLG) simulations of single-molecule Junctions

In this section, I repeat the same gold-gold simulations for the single-molecule junction involving A (**1, 2, 3**), B (**4** and **5**). However, the junctions here are asymmetric (i.e., Au-Gr). Figure 5.5 shows the studied molecules in gold and single layer graphene sheet (SLG) junctions.

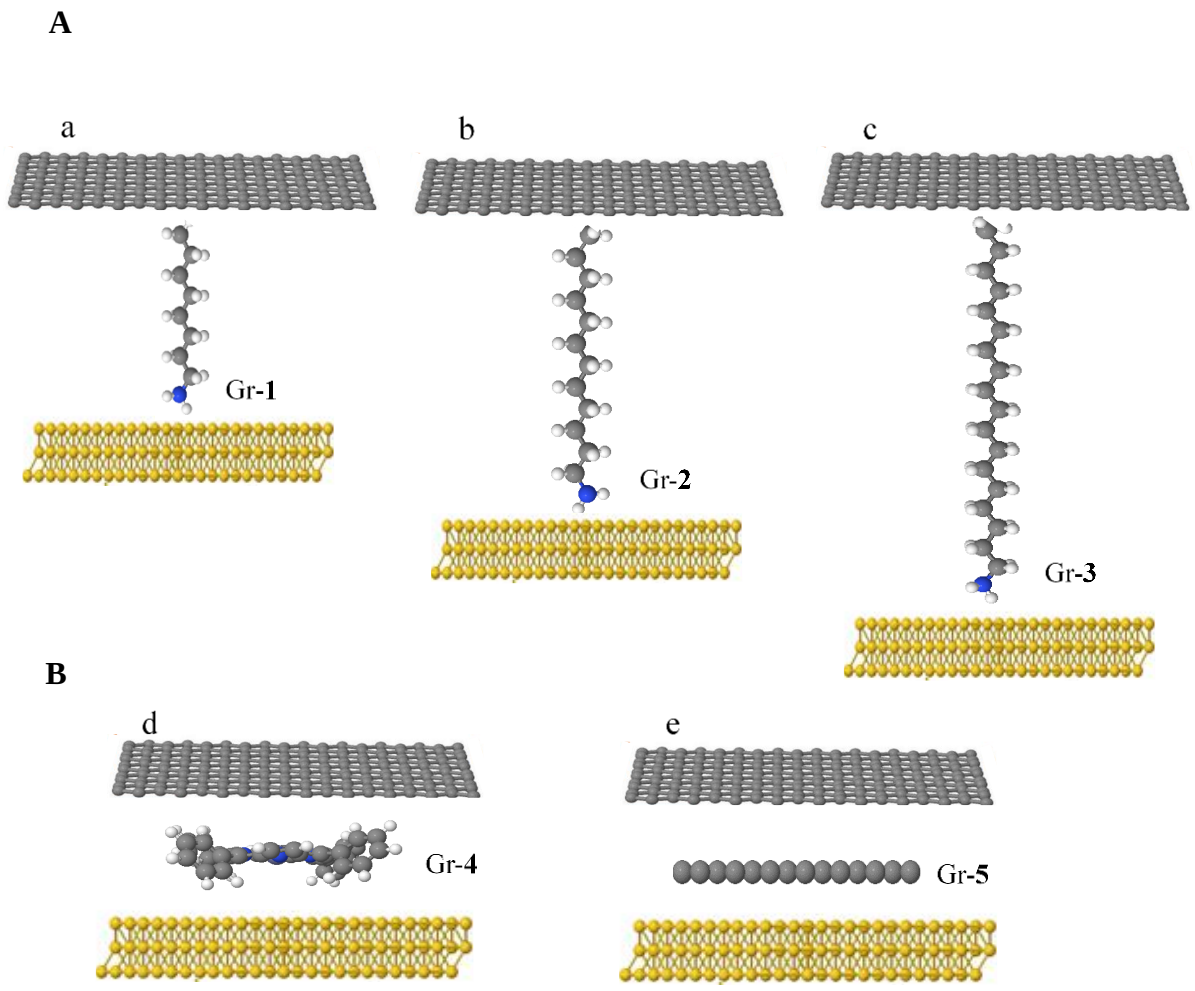


**Figure 5.6:** A schematic figure of the Au-mono-SLG junctions. Top contact is SLG electrode, and the bottom contact is Au electrode. A: **a-c** is alkyl chains Au/**1-3**/SLG single-molecule junctions. While B: **d-e** are ZnTPP and graphene sheet Au-**4**-SLG, and Au-**5**-SLG respectively.

### 5.3.2 Gold- Graphene Sheet (SLG) Simulation of Bilayer Structures

This section represents the bilayer structures **4/6, 4/7** and **4/8** attached to gold and a single layer graphene sheet (SLG).

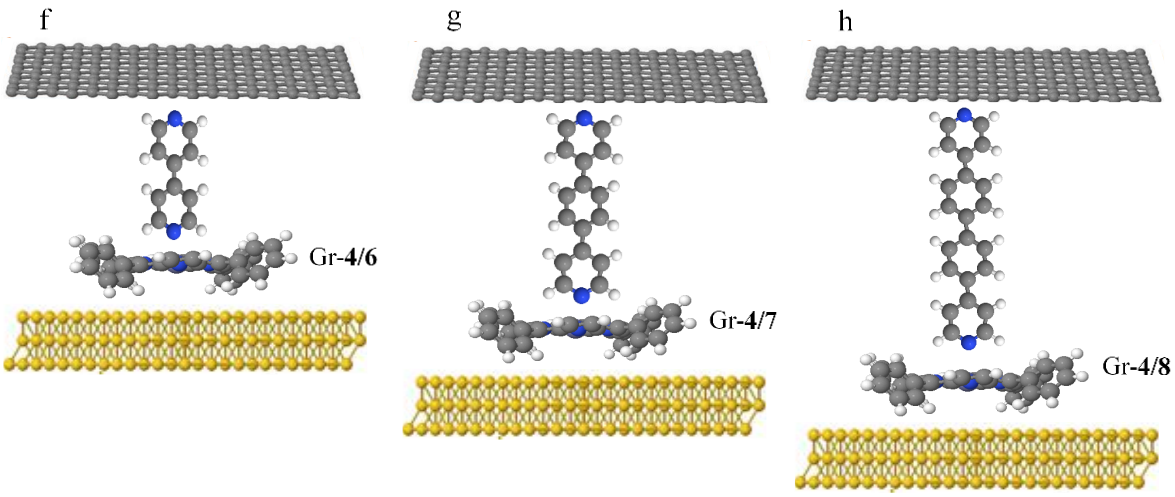


**Figure 5.7:** A schematic figure of the Au-bilayer-SLG junctions. Top contact is SLG electrode, and the bottom contact is Au electrode. **f**: Au-**4/6**-SLG, **g**: Au-**4/7**-SLG, **h**: Au-**4/8**-SLG bilayer junctions.

## 5.4 Transport Simulations

As is described in section 4.8 of chapter 4, to investigate the transmission coefficient, I started from the completely optimised gas-phase molecules and then constructed the junctions by attaching the molecules via different anchor groups to gold and SLG electrodes. Similar to the computations shown in chapter 4, the ground state Hamiltonian and optimised geometry of each compound were obtained using the density functional theory (DFT) code and combined with the Gollum transport code. The generalised gradient approximation (GGA) exchange correlation functional was used along with double zeta polarized (DZP) basis sets and the norm-conserving pseudo potentials. The real space grid was defined by a plane wave cut-off of 250 Ry. The geometry optimization was carried out to a force tolerance of 0.01 eV/Å. This

process was repeated for a unit cell with the molecule between two electrodes where the optimised distance between electrodes and the anchor groups are shown in Table 5.1. In what follows, I will investigate the charge transport properties for eight asymmetric junctions (gold-SLG electrodes) as shown in Figures 5.6-5.7.

### 5.4.1Transport Simulations of alkyl chains in Au-1-3- SLG and Au-5- SLG Junctions

The transmission coefficient curves *T(E)* were calculated for the single-molecule junctions using the Gollum transport code. The bottom panel in Figure 5.8 shows 3 transmission curves of the alkyl-chain junctions Au/**1-3**/SLG, in which the alkyl chains have different lengths (n=8, 12 and 18). It is clear from Figure 5.8 that as the chains get longer, their conductance become smaller, following a similar trend noted for Au-**1-3**-Au junctions. In addition, Fermi energy is predicted near the middle of the HOMO-LUMO gap. The actual values of the conductance for the alkyl chains are $\log_{10} G/G_0 =$ -3.0, -5.0, -7.0 respectively. On the other hand, the transmission coefficient of the Au-**5**-SLG junction, formed by inserting the graphene-like molecule between Au and SLG electrodes as shown in the bottom panel in Figure 5.10, shows that in this case, charge transfer is LUMO dominated, and the conductance is approximately $\log_{10} G/G_0 =$ -2.0.

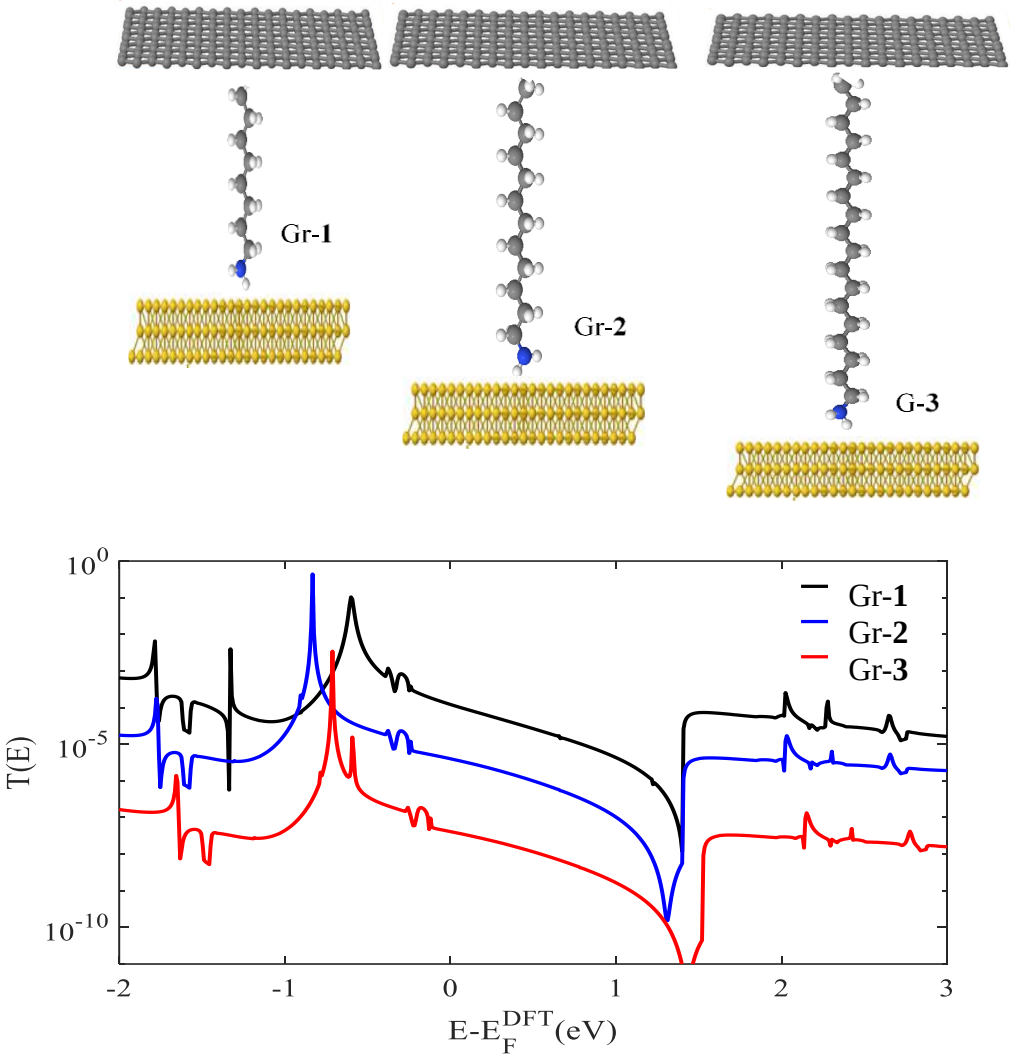


**Figure 5.8**: **Top panel**: Representation of alkyl chains single-molecule junctions. **Bottom panel**: transmission coefficients *T(E)* curves of Au-**1**-SLG junctions against electron energy E. Molecules **1-3,** black, blue and red curves respectively.

### 5.4.1.1. Transport simulations of alkyl chains terminated by methyl groups in Au-1-3-SLG.

The transmission coefficient curves *T(E)* were calculated for the alkyl chains terminated by methyl group as shown in the top panel of Figure 5.9. These curves exhibit a similar trend noted for Au-**1-3**-SLG junctions terminated by direct carbon, with a Fermi energy expected to be near the middle of the HOMO-LUMO gap. The actual values of the conductance for the alkyl chains

are $\log_{10} G/G_0$ = -3.0, -5.0, -7.0 respectively. Therefore, removing one of the hydrogen atoms from the anchor group of alkyl chains molecules does not significantly affect its conductance or trends. The conductance of a molecule depends on its overall structure and the arrangement of its electrons. If the molecule maintains its overall structure and essential electronic properties such as delocalized π-electrons or conjugation, then as shown by these results, the change in its conductance with length remains qualitatively the same, even after removing a hydrogen atom from the anchor group.

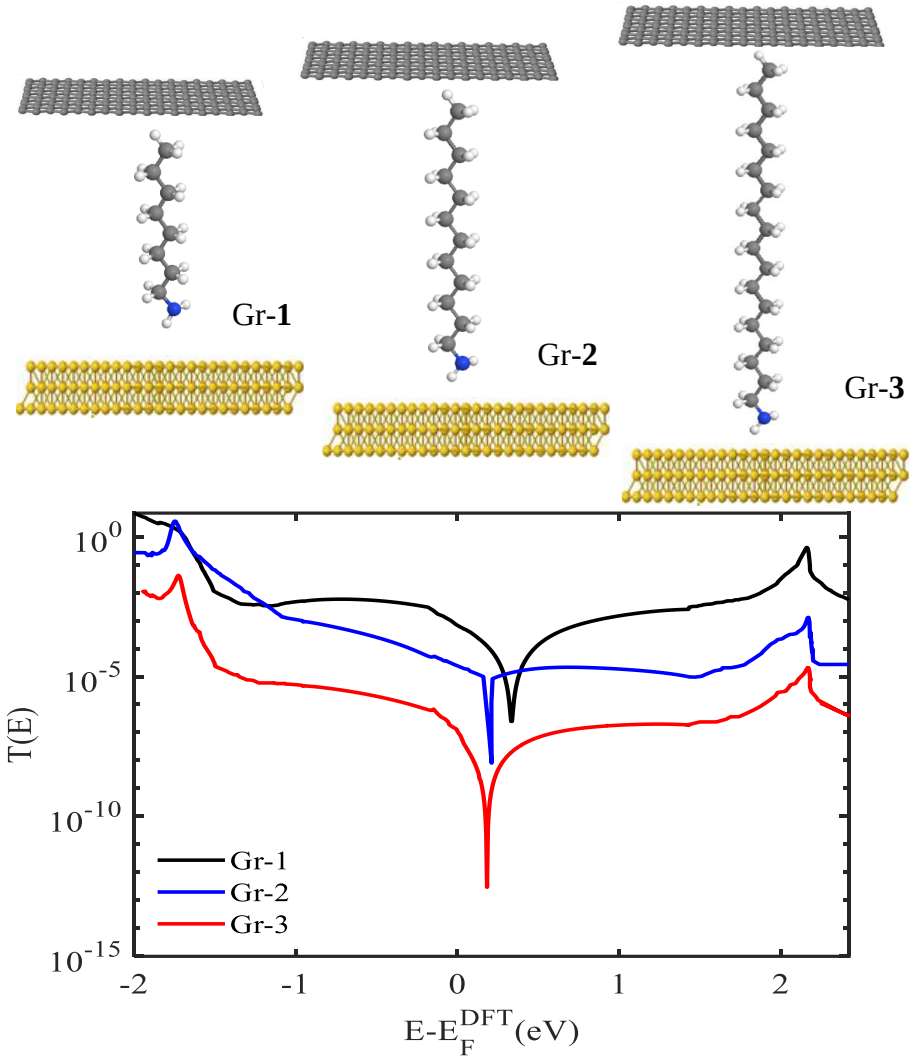


**Figure 5.9**: **Top panel**: Representation of alkyl chains terminated by methyl group single-molecule junctions. **Bottom panel**: transmission coefficients *T(E)* curves of Au-**1**-SLG junctions against electron energy E. Molecules **1-3,** black, blue, and red curves respectively.

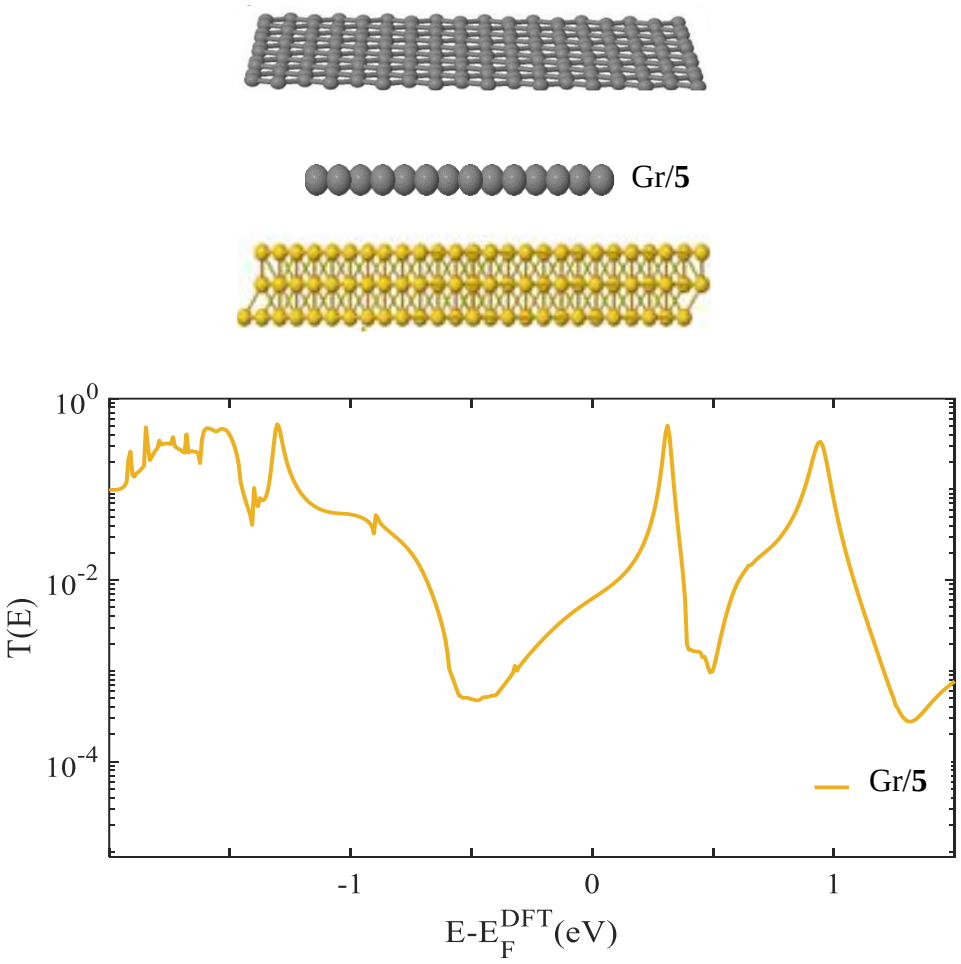


**Figure 5.10**: **Top panel:** Schematic illustrations of molecular junction for Au-**5**-SLG**. Bottom panel**: transmission coefficient $T(E)$ of molecule **5** as a function of energy.

### 5.4.2 Spin Polarised Transport Calculations of Single molecule/Bilayer Molecular Junctions

The application of electron spin for storage and processing is a current area of nanotechnology study. Inorganic materials are a component in some modern spintronic devices, and the use of organic materials in spintronics is already a significant research area in the scientific and engineering disciplines [30-31]. Double-stranded DNA (dsDNA) monolayers at room temperature were found to transmit spin-selective electrons, according to research by Gohler et al [32]. They stated that dsDNA length increases spin polarization, and they demonstrated effective spin filtering [33]. In a theoretical study, spin polarization and spin-dependent electron conductance on the helix symmetry were evaluated using the Green's function method. Here I shall carry out spin-dependent transport computations for the single molecule Zinc tetraphenyl porphyrin (ZnTPP), molecule **4** and then, I combine Porphyrin (ZnTPP) with the pyridine -based cores **6,7,8**, as shown in the top panel of Figures 5.9-5.12. The generalized gradient approximation (GGA) was used, along with the transport code Gollum for this calculation. The HOMO resonance occurs near the Fermi energy for all these junctions, showing that the charge transfer is HOMO dominated, which is completely opposite to the case where the same molecules are attached to the two gold electrodes (see section 4.4.5 in chapter 4 for more details). Spin up and spin down transmission coefficients for these junctions are slightly different. The conductance values are $\log_{10} G/G_0 =$ -4.0, -5.0, -7.0, and -10.0 respectively.

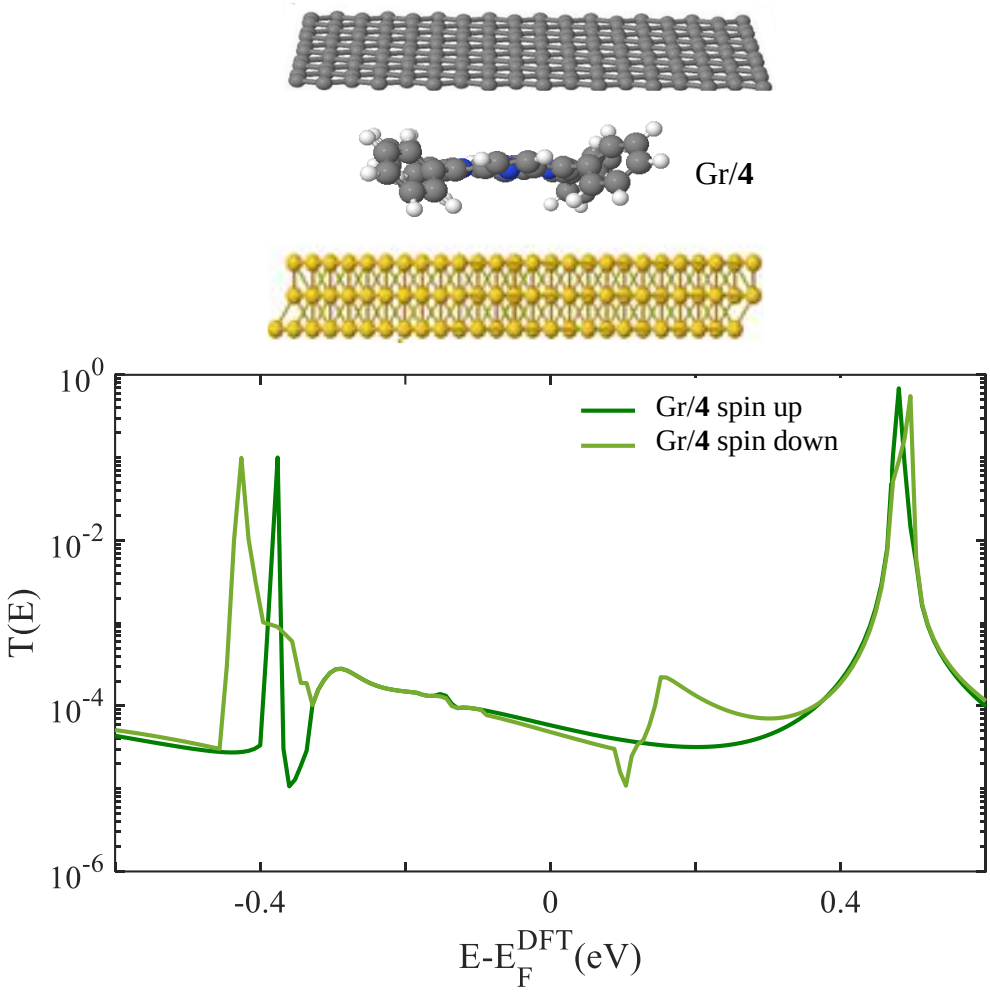


**Figure 5.11: Top panel:** Schematic illustrations of molecular junction for Au-**4**-SLG. **Bottom panel:** Spin-polarised transmission coefficients, $T(E) = \frac{T_{up}(E)+T_{down}(E)}{2}$, of Au-**4**-SLG junctions against electron energy E. Molecule **4,** dark and light green curves represent spin up and down curves respectively.

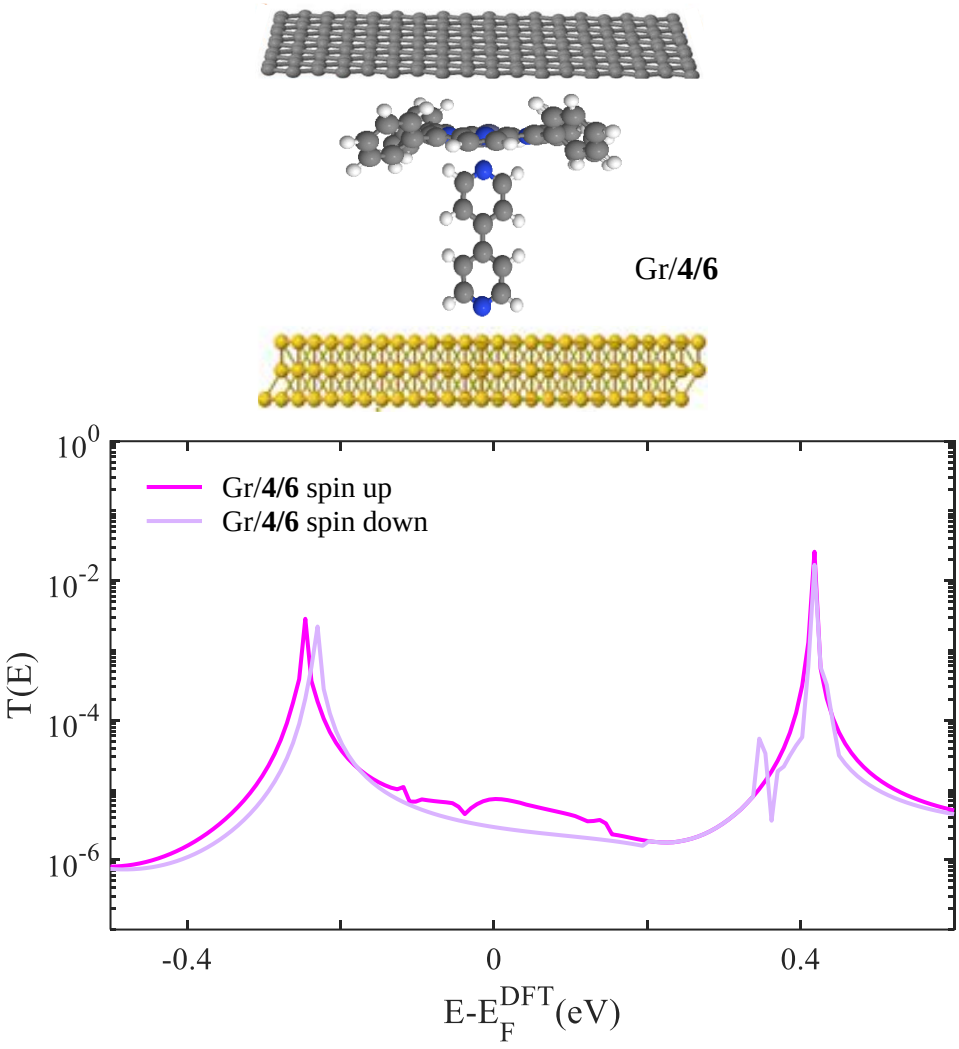


**Figure 5.12:** Top panel: Schematic illustrations of molecular junction for Au-4/6-SLG. Bottom panel: Spin-polarised transmission coefficients, $T(E) = \frac{T_{up}(E)+T_{down}(E)}{2}$, of Au-4/6-SLG junctions against electron energy E. bilayer 1, dark and light purple curves represent spin up and down curves respectively.

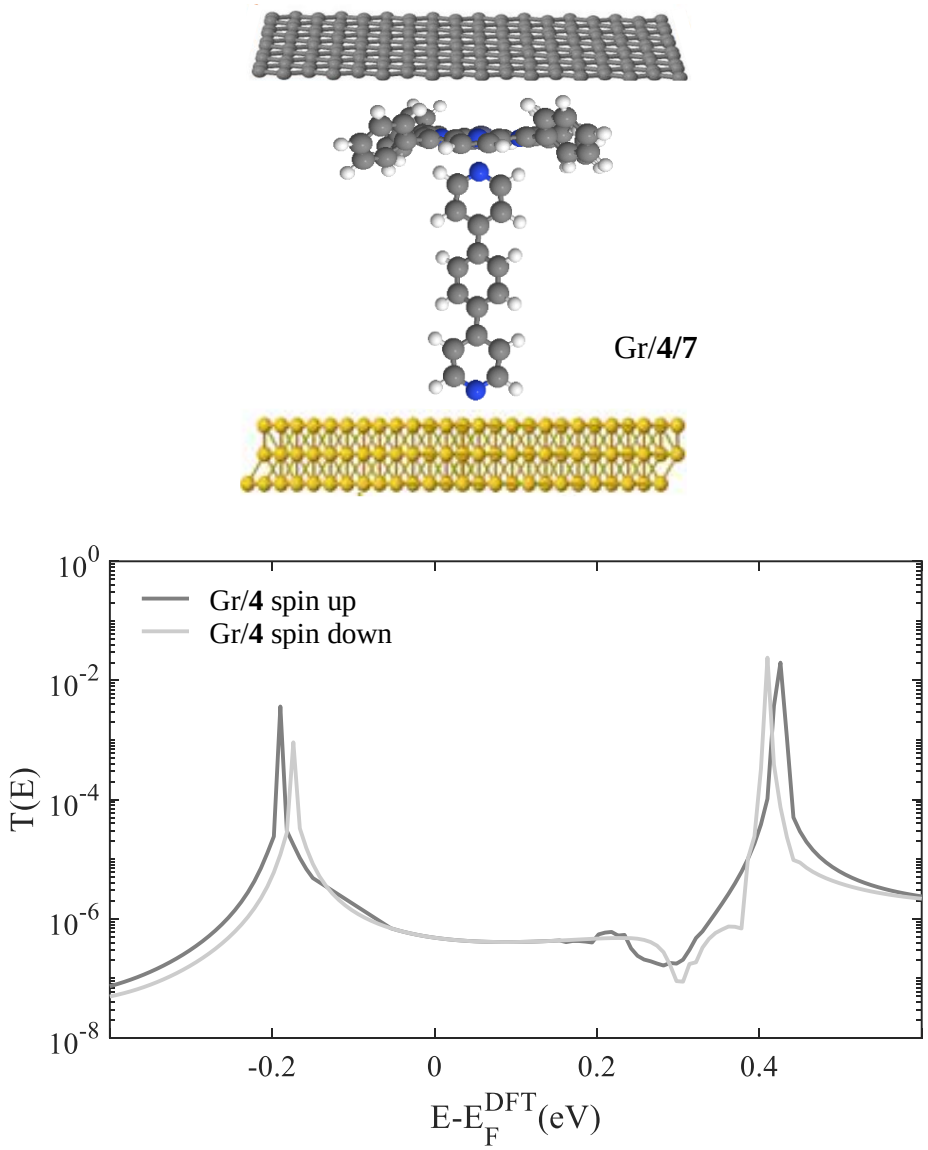


**Figure 5.13**: **Top panel**: Schematic illustrations of molecular junction for Au-**4/7**-SLG.

**Bottom panel** Spin-polarised transmission coefficients, $T(E) = \frac{T_{up}(E)+T_{down}(E)}{2}$, of Au-**4/7**-SLG junctions against electron energy E. bilayer **2,** dark and light grey curves represent spin up and down curves respectively.

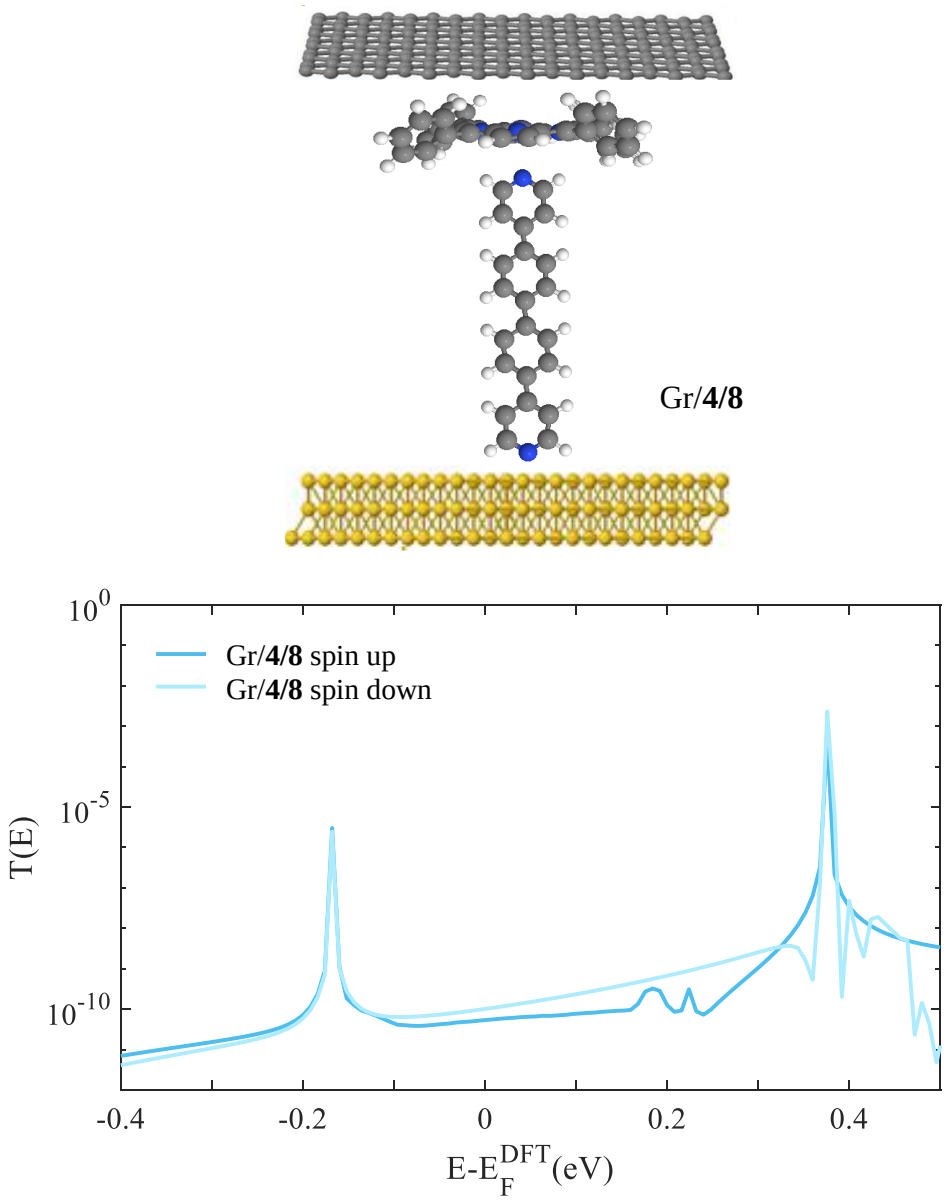


**Figure 5.14: Top panel**: Schematic illustrations of molecular junction for Au-**4/8**-SLG. **Bottom panel**: Spin-polarised transmission coefficients, $T(E) = \frac{T_{up}(E)+T_{down}(E)}{2}$, of Au-**4/8**-SLG junctions against electron energy E. bilayer **3,** dark and light blue curves represent spin up and down curves respectively.

## 5.5 Thermopower Simulations

Equation 4.5, as described in chapter 4, is used to determine the Seebeck coefficient for the eight junctions that are attached to the gold/ SLG electrodes. First, I shall calculate the single molecule then bilayer's Seebeck coefficients as shown in Figures 5.7-5.8. It is worth mentioning that, the sign and the magnitude of the Seebeck coefficient are determined by the transmission coefficient's slope. In other terms, whether the curve is HOMO or LUMO dominated.

### 5.5.1 Thermopower Simulation for Alkyl Chains and Graphene-like molecules in Au-SLG Junctions.

Figure 5.14 shows the Seebeck coefficients $S$ of alkyl chains evaluated at room temperature involving **1, 2, 3** where the $E_F$ is placed near to the HOMO resonances. The sign of $S$ found to be positive and the value of $S$ for the Au-**1**-SLG, Au-**2**-SLG, and Au-**3**-SLG junctions are 24, 16.5, and 17 μV/K respectively. On the other hand, Figure 5.14 shows the Seebeck coefficient $S$ of **5** to be negative at the DFT-predicted Fermi $E\text{-}E_F^{DFT}$=0 eV, because this molecule is LUMO dominated and the actual value for $S$ is -8.0 μV/K

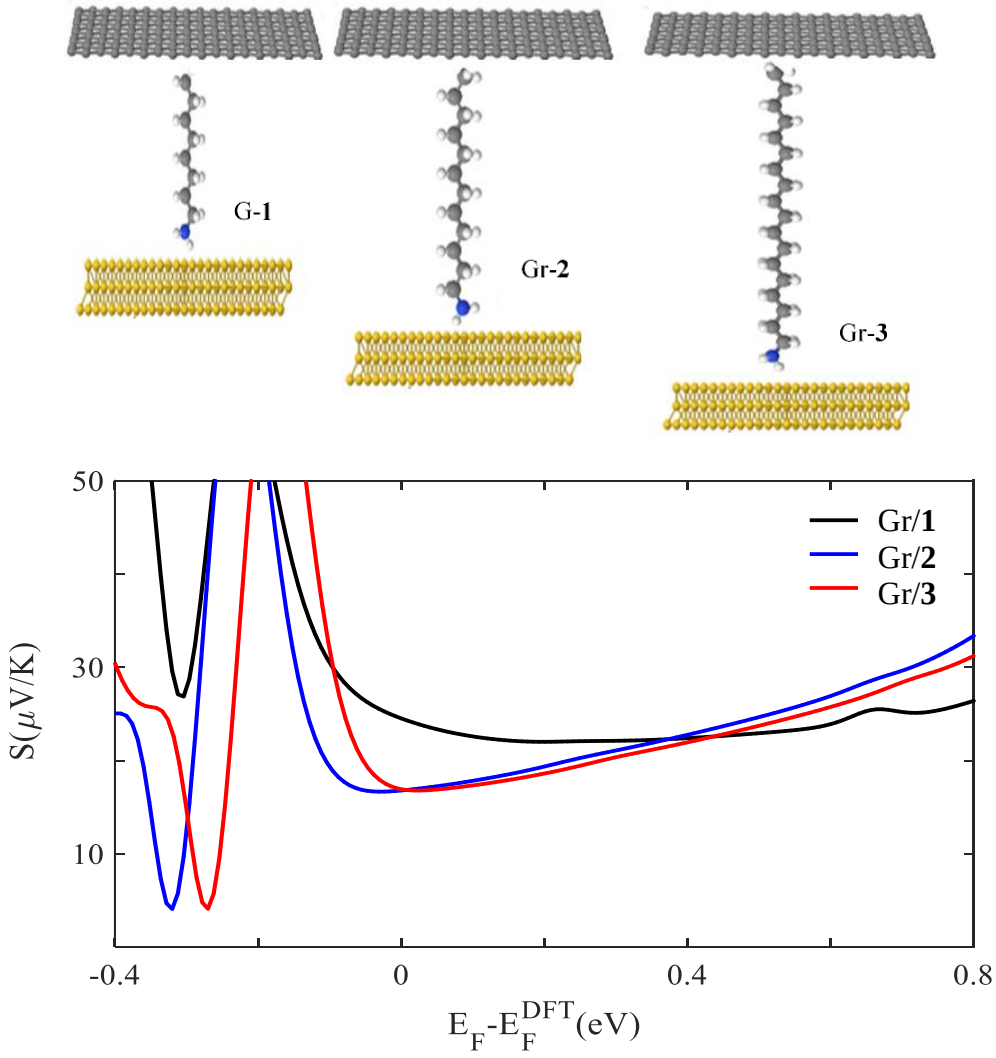


**Figure 5.15**: **Top panel**: Schematic illustrations of molecular junctions for the alkyl chain monolayers Au-**1**-SLG, Au-**2**-SLG, and Au-**3**-SLG. **Bottom panel**: Seebeck coefficient *S* as a function of Fermi energy of three alkyl chain. Seebeck coefficients of **1, 2** and **3,** black, blue and red curves respectively.

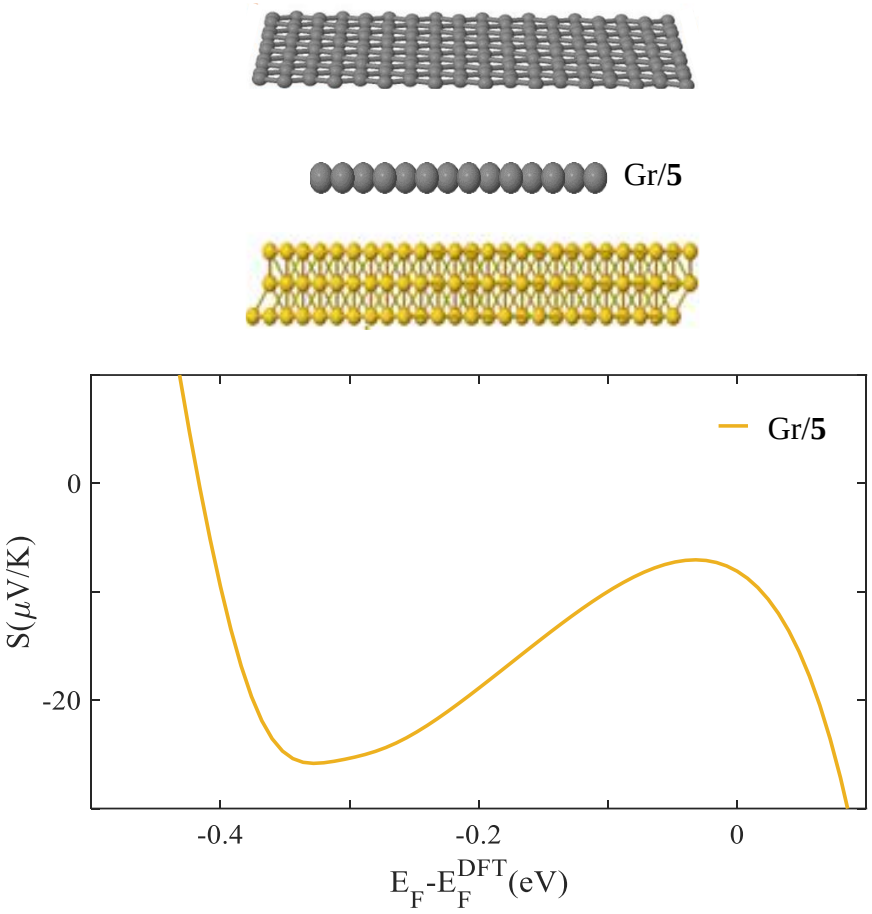


**Figure 5.16**: **Top panel**: Schematic illustrations of molecular junctions for the Au-**5**-SLG. **Bottom panel**: Seebeck coefficient S as a function of Fermi energy of graphene sheet. Seebeck coefficient of monolayer **5,** orange curve.

### 5.5.2 Spin-polarised Thermopower Calculations of Single-molecule/Bilayer Junctions

Due to a metal atom in the following molecules, spin polarised calculations are carried out in this section. The Seebeck value for mono/bilayer structures **4, 4/6, 4/7**, and **4/8** is found to be positive at the DFT-predicted Fermi levels $E\text{-}E_F^{DFT}$=0 eV, because these molecules are HOMO-dominated as shown in Figures 5.16-5.19. In this case, the spin up and spin down transmission curves are slightly different. The values of $S$ are 14 $\mu V/K$ for Au-**4**-SLG. While for the Au-**4/6**-SLG, Au-**4/7**-SLG, and Au-**4/8**-SLG are 70, 178 and 300 $\mu V/K$ spin up and spin down respectively.

.

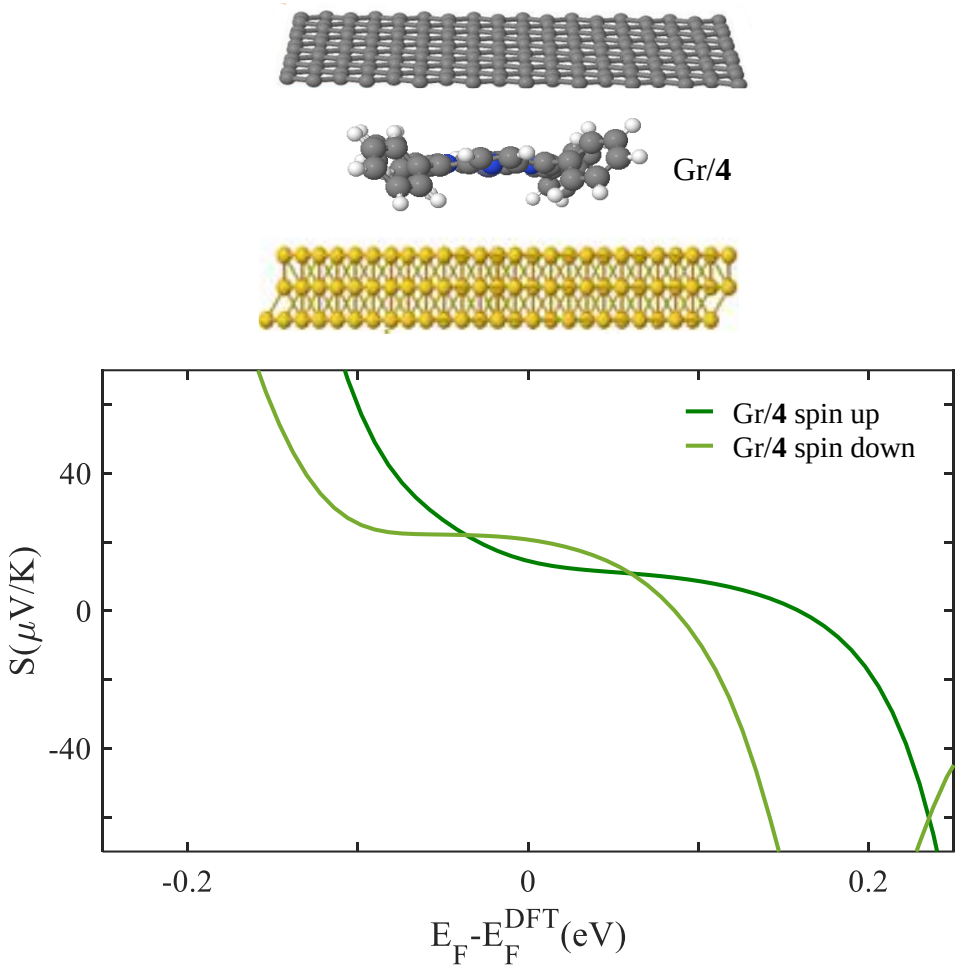


**Figure 5.17**: **Top panel**: Schematic illustrations of molecular junctions for the Au-**4**-SLG. **Bottom panel**: Seebeck coefficient S as a function of Fermi energy of ZnTTP. Seebeck coefficients of **4,** dark and light green curves represent the spin up and down.

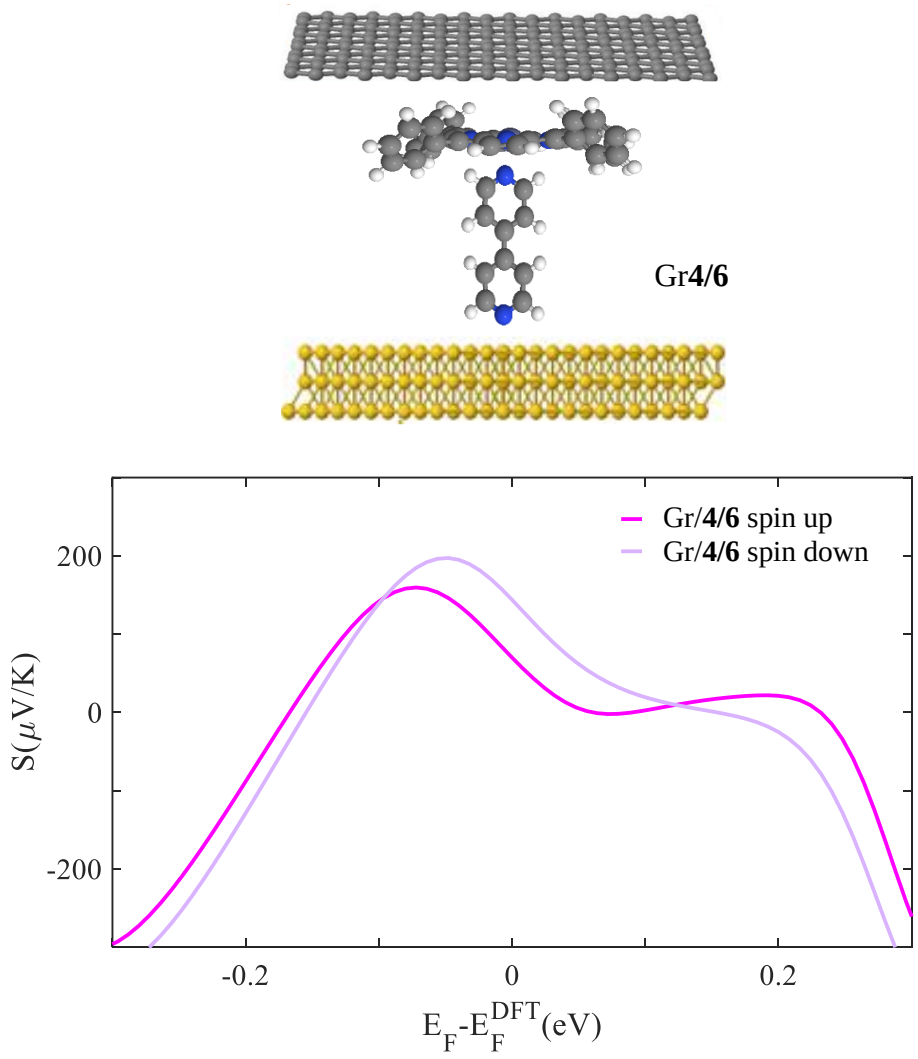


**Figure 5.18:** Top panel: Schematic illustrations of molecular junctions for the Au-4/6-SLG. Bottom panel Seebeck coefficient S as a function of Fermi energy of bilayer 1. Seebeck coefficients of bilayer 4/6, dark and light purple curves represent the spin up and down curves.

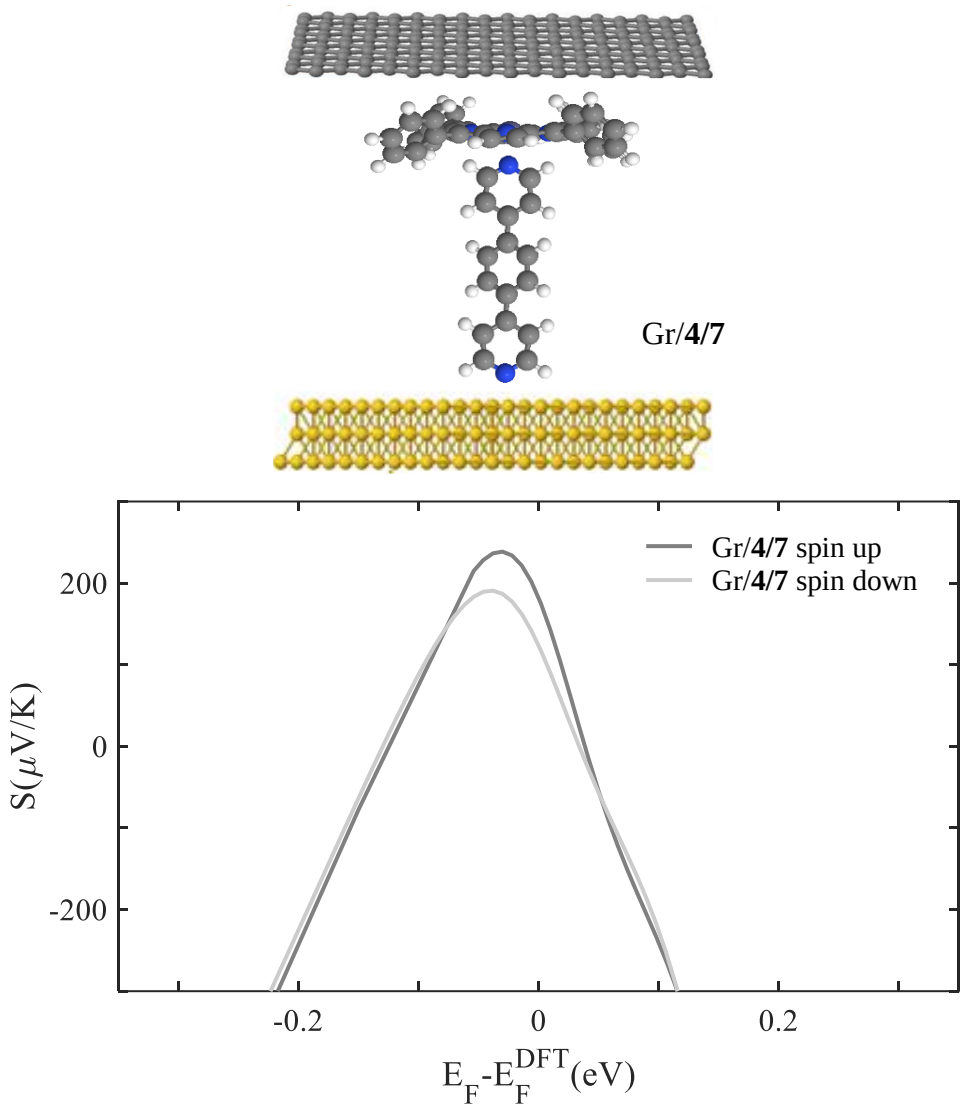


**Figure 5.19**: **Top panel**: Schematic illustrations of molecular junctions for the Au-**4/7**-SLG. **Bottom panel** Seebeck coefficient S as a function of Fermi energy of bilayer **2**. Seebeck coefficients of bilayer **4/7,** dark and light grey curves represent the spin up and down curves.

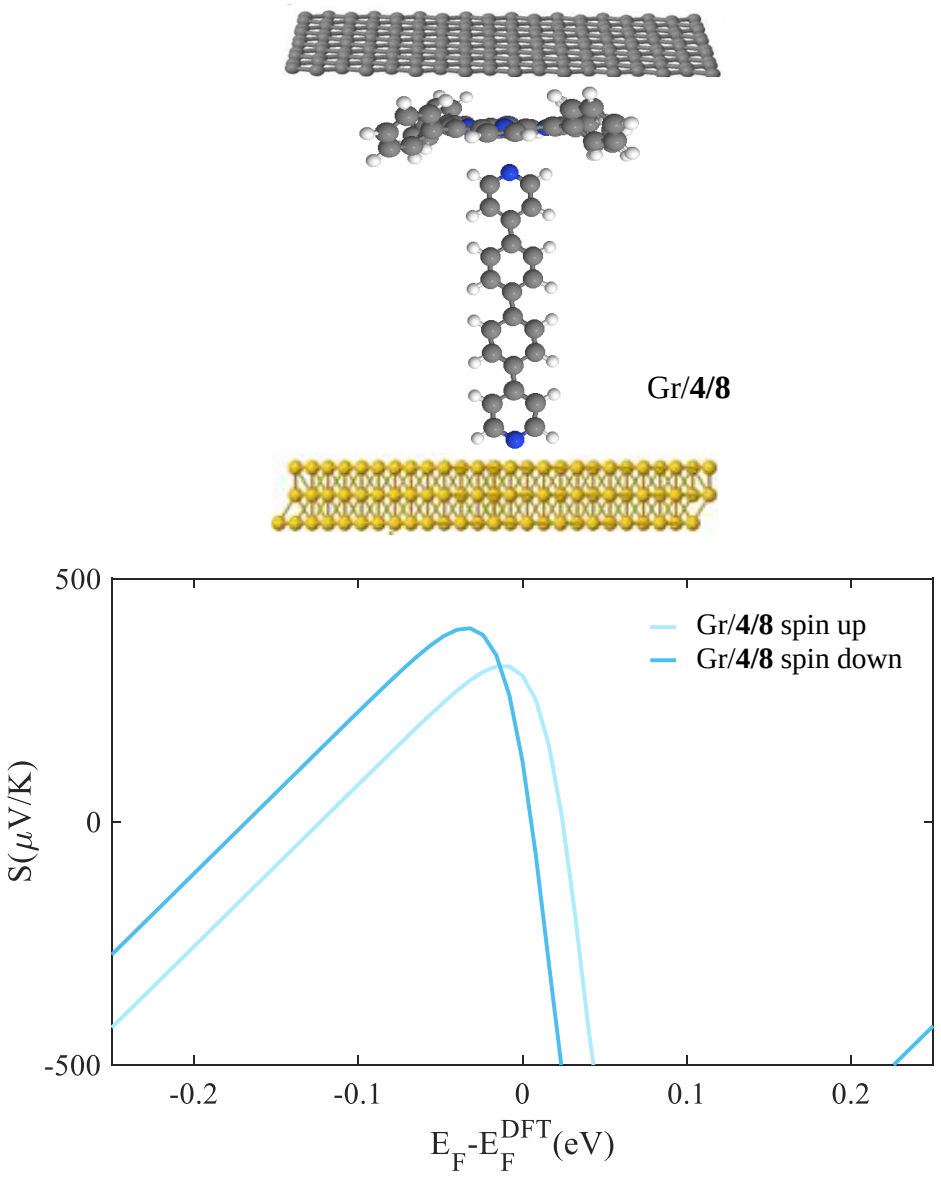


**Figure 5.20:** Top panel: Schematic illustrations of molecular junctions for the Au-4/8-SLG. Bottom panel Seebeck coefficient S as a function of Fermi energy of bilayer 3. Seebeck coefficients of bilayer 4/8, dark and light blue curves represent the spin up and down curves.

## 5.6 Experimental Section

In this research, the experiments employed a technique to create well-spaced arrays of oligo-phenyl wires on a single-layered (SL) graphene substrate [34]. Initially, zinc tetraphenyl porphyrin (ZnTPP, molecule 4 in Figure 1.5 (a) was utilized to form a thin molecular film on SL chemical-vapor-deposited (CVD) graphene on a copper substrate. The attachment of ZnTPP molecules to graphene occurred through π-π stacking interactions. Subsequently, conjugated pyridine backbone molecules (molecules 6, 7, and 8 in Figure 4.2 were deposited onto the ZnTPP layer via zinc-pyridine coordinative bonds. These backbones exhibited a perpendicular orientation to the substrate due to their lone pair geometry and were separated from each other by the large footprint of ZnTPP molecules. The measured results obtained from AFM were found to be in good agreement with the corresponding thickness values estimated using density functional theory (DFT). This concordance between experimental and theoretical approaches further validates the bilayer growth. Additionally, this study also examined a series of alkyl amine molecules known for forming high-quality self-assembled monolayers (SAMs) on graphene through non-covalent interactions as reported previously [35-36], for comparative analysis.

In this study, the electrical and thermoelectric properties of SAMs are investigated by building molecular junctions using eutectic Gallium Indium alloy (EGaIn) [37] serving as the upper electrode. EGaIn is a flexible liquid metal with non-Newtonian properties.

A cone-shaped tip was formed from EGaIn and maintained its structure by developing a native oxide outer layer (GaOx) of approximately 0.7 nanometres upon exposure to air [38-39]. Research has demonstrated that such tips can make non-destructive contact with SAMs [40] and create Cu/Gr/SAMs/GaOx/EGaIn junctions.

### 5.6.1 Experiment Results

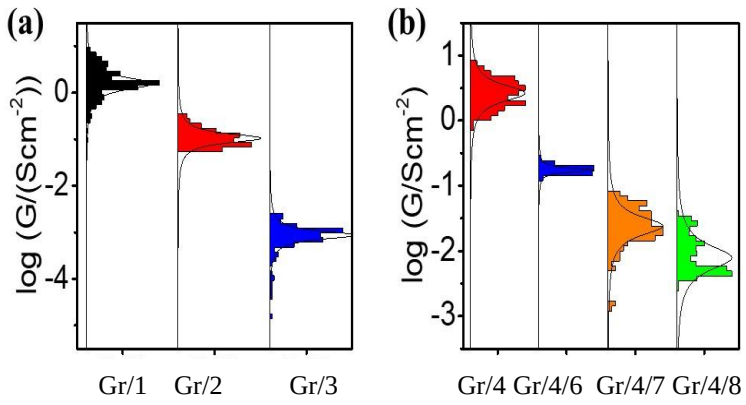


**Figure 5.21**: (**a**) G-V curve of Gr/SAMs/GaOx/EGaIn junction, SAMs molecule: **1**, **2** and **3**; (**b**) G-V curve of Gr/SAMs/GaOx/EGaIn junction, SAMs molecule: **4**, **4/6, 4/7** and **4/8** [42].

Figure 3(a) illustrates the statistical distribution of conductance (G) at zero bias, obtained using numerical differentiation for various alkyl linker junctions. As the quantity of CH2 units increases, the conductance value decreases exponentially.

The multi-component conjugated SAM-based junctions Gr/4/6, Gr/4/7, and Gr/4/8 were tested using electrical behaviour measurements. The statistical findings were derived from 80 J-V curves acquired on a minimum of two independent samples.

Figure 3(b) displays the corresponding numerical differential conductance at zero bias. The electric conductivity for the pyridine-based oligo-phenyl linkers (molecule 6, 7 and 8) was expected to be higher than the alkyl linkers (molecule 1, 2, and 3) with similar lengths, because the delocalized electrons in the π system facilitate the electron transport process which the electrical values DFT result.

The thermoelectric properties of SAMs were examined Using a modified EGaIn configuration that included a Peltier stage and two thermocouples for controlling and tracking the temperature difference (V).

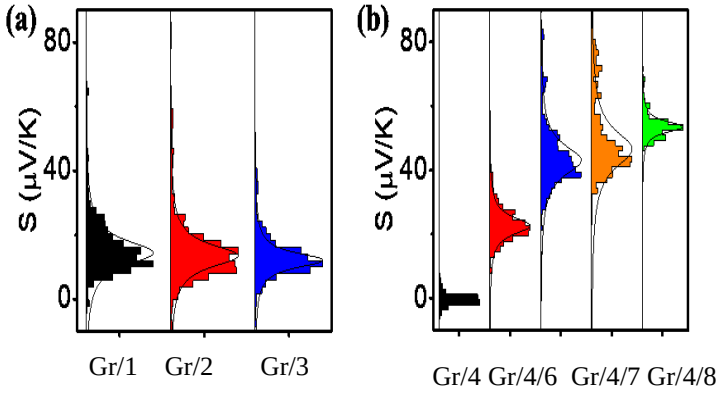


**Figure 5.22:** Thermoelectric properties of molecular junctions. (**a, b**) statistics of Seebeck coefficient for all measured junctions [42].

Figure (a) displays the measured Seebeck distributions of various chain length alkyl junctions on graphene surfaces. Each type of junction was measured on at least two independent samples prepared with the same recipe**.** Since the slopes of linear fits for all junctions were negative, the Seebeck coefficients of the junctions were positive. This indicates that the electrode Fermi level was placed closer to the molecular orbital HOMO resonance [41].

Figure 4 (b) shows the measured Seebeck distribution of all conjugated molecular junctions on graphene substrates using a first layer of ZnTPP (molecule 4) as a footprint. A ZnTPP layer adsorbed on graphene without the growth of a conjugated backbone (molecules 6-8) was determined to be 19 ± 4.4 μV/K, which is approximately two times higher than that observed. The Seebeck coefficients increased to 40 ± 8.4 μV/K (Gr/4/6), 47.5± 9.1 μV/K (Gr/4/7), and 51±9.2 μV/K (Gr/4/8). These values are about three times higher than those of alkyl linkers which agree with theoretical result.

## 5.7 Validating the DFT Simulations Against experimental Measurements.

My experimental collaborators at Cavendish Laboratory, University of Cambridge and Dalian Maritime University provided me with the Seebeck coefficient measurements for both single-molecule and bilayer junctions. In this section, I am going to validate my theoretical simulations against the experiment results. In chapter 4, I preformed my simulations on symmetric junctions (specifically gold-gold junctions), and calculated their conductance and thermopower. Here, I shall restrict the comparison to their thermopower only.

Table 5.1 shows the measured Seebeck coefficients for both single-molecule and bilayer structures (2$^{nd}$ column). The experimentalists informed me that their drain, and source are made of gold and the eutectic Gallium Indium alloy (EGaIn, 1$^{st}$ column). My first simulations on these structures were in gold-gold junctions and the predicted Seebeck coefficient values are presented in the 4$^{th}$ column. Regardless to the numbers of $S_{STM}$ and $S_{DFT}$ (2$^{nd}$ versus 4$^{th}$), one could see the sign of *S* is completely the opposite for the two sets of values. Since the sign is the opposite for the eight studied junctions, this suggests that EGaIn-Au cannot be equivalent to Au-Au junction as demonstrated in Table 5.1.

**Table 5.2.** Thermoelectric properties of the studied structures in symmetric junctions. Measured and predicted Seebeck coefficients experimental measurement, and DFT respectively. DFT simulations for Au-Au junctions and at the DFT-predicted Fermi ($E_{\mathrm{F}} - E_F^{DFT} = 0\ eV$). For more detail about Au-Au simulations see chapter 4.

| Junction | Experimental measurement $S\,(\mu V/K)$ | std $S\,(\mu V/K)$ | DFT $S\,(\mu V/K)$ Au-Au junction | Polarization state |
|---|---|---|---|---|
| EGaIn -**1**-Au | 16.5 | +/-8 | -0.5 | == |
| EGaIn -**2**-Au | 14.0 | +/-9.5 | -3.0 | == |
| EGaIn -**3**-Au | 13.5 | +/-8 | -1.6 | == |
| EGaIn -**4**-Au | -0.26 | +/-0.2 | 4.0 | == |
| EGaIn -**5**-Au | 11.0 | +/-4.4 | -8.0 | == |
| EGaIn -**4/6**-Au | 40.0 | +/-8.4 | -(225+227) | spin up, spin down |
| EGaIn -**4/7**-Au | 47.5 | +/-9.1 | -(223+247) | spin up, spin down |
| EGaIn -**4/8**-Au | 51.0 | +/-9.2 | -(236+238) | spin up, spin down |

As the first set of simulations failed against the experiments (chapter 4). I repeated the same simulations however, this time in asymmetric junction (i.e., gold-graphene), as shown in section 5.5. Table 5.2 summarizes the Seebeck results of the asymmetric junctions and compares them against experimental measurements.

By looking at the Seebeck coefficient signs in the 2nd and 4th columns, one could tell that Au-Gr simulations reproduced the experimental measurements for every single junction. As for the actual values,

DFT simulations successfully predict the experimental measurements trend. This comparison suggests that asymmetry plays a crucial role in the experiments and that the origin of the asymmetry (ie the choice of the asymmetric electrodes) may not be of primary importance. It should be noted an excellent agreement obtained between experimental measurements and DFT for the single-molecule junctions and less accurate for bilayers as the system is more complicated (i.e., multicomponent).

**Table 5.3.** Thermoelectric properties of the studied structures in asymmetric junctions. Measured and predicted Seebeck coefficients experimental measurements, and DFT respectively. DFT simulations for Au-Gr junctions and at the DFT-predicted Fermi ($E_{\mathrm{F}} - E_F^{DFT} = 0\ eV$). For more detail about Au-Gr simulations see section 5.5 above.

| Junction | Experimental measurements $S\,(\mu V/K)$ | std $S\,(\mu V/K)$ | DFT $S\,(\mu V/K)$ Au-Gr junction | Polarization state |
|---|---|---|---|---|
| EGaIn -**1**-Au | 16.5 | +/-8 | 24 | == |
| EGaIn -**2**-Au | 14.0 | +/-9.5 | 16.5 | == |
| EGaIn -**3**-Au | 13.5 | +/-8 | 17 | == |
| EGaIn - **4** -Au | -0.26 | +/-0.2 | -8 | == |
| EGaIn -**5**-Au | 11.0 | +/-4.4 | 14 | == |
| EGaIn -**4/6**-Au | 40.0 | +/-8.4 | 70 | spin up, spin down |
| EGaIn -**4/7**-Au | 47.5 | +/-9.1 | 178 | spin up, spin down |
| EGaIn -**4/8**-Au | 51.0 | +/-9.2 | 300 | spin up, spin down |

## 5.8. Conclusion

Overall, in this work I demonstrate a strategy of utilizing multi-component method to fabricate conjugated molecular backbone on graphene substrate separated with equal distance using ZnTPP as footprint and compare it with the amine based non-conjugated junctions with similar tunnelling length. For asymmetric single-molecule junctions, I found that the alkyl chains are a HOMO-dominated with positive $S$; while the junction formed from the graphene-like molecule is a LUMO-dominated with negative $S$. Secondly, I examined asymmetric bilayer junctions. I also have calculated the spin-polarised transmission coefficients and the Seebeck for these molecules, which were required as the junctions involve metallic atom (Zn). At the DFT-predicted Fermi energy ($E_{\mathrm{F}} - E_F^{DFT} = 0\ eV$), I showed that all junctions are HOMO-dominated with a positive $S$. Furthermore, the electron transport of the molecular junctions shows similar tunneling decay factors as other similar oligo-phenyl structures on metal substrates. The Seebeck coefficient of the multi-component junction was about 3 times higher than the alkyl-based molecules, with comparable thickness, and higher than the Seebeck of most reported molecular junctions (> 50 μV/K). This suggests a new way for achieving high thermoelectric performance molecular-scale junctions.

## 5.9 Bibliography


3. Phuangburee, T., Solonenko, D., Plainpan, N., Thamyongkit, P., Zahn, D. R., Unarunotai, S., … Leeladee, P. (2020). Surface modification of graphene oxide via noncovalent functionalization with porphyrins for selective photocatalytic oxidation of alcohols. New Journal of Chemistry, 44(20), 8264–8272. doi:10.1039/d0nj01141j
4. Winter, S., Weber, E., Eriksson, L., & Csöregh, I. (2006). New Coordination Polymer Networks based on copper (II) hexafluoroacetylacetonate and pyridine containing building blocks: Synthesis and structural study. New J. Chem., 30(12), 1808–1819. doi:10.1039/b604591j
5. Li, Q., Strange, M., Duchemin, I., Donadio, D., & Solomon, G. C. (2017). A strategy to suppress phonon transport in molecular junctions using π-stacked systems. The Journal of Physical Chemistry C, 121(13), 7175–7182. doi:10.1021/acs.jpcc.7b02005
6. Zhao, S., Chen, H., Qian, Q., Zhang, H., Yang, Y., & Hong, W. (2021a). Non-covalent interaction-based molecular electronics with graphene electrodes. Nano Research, 16(4), 5436–5446. doi:10.1007/s12274-021-3687-2
7. Cubukcu, E., Aydin, K., Ozbay, E., Foteinopoulou, S., & Soukoulis, C. M. (2003). Subwavelength resolution in a two-dimensional photonic-crystal-based superlens. Physical Review Letters, 91(20). doi:10.1103/physrevlett.91.207401
8. Lörtscher, E. (2013). Wiring molecules into circuits. Nature Nanotechnology, 8(6), 381–384. doi:10.1038/nnano.2013.105
9. Prins, F., Hayashi, T., de Vos van Steenwijk, B. J., Gao, B., Osorio, E. A., Muraki, K., & van der Zant, H. S. (2009). Room-temperature stability of PT nanogaps formed by self-breaking. Applied Physics Letters, 94(12). doi:10.1063/1.3109784

10. Seo, S., Hwang, E., Cho, Y., Lee, J., & Lee, H. (2017). Functional molecular junctions derived from double self-assembled monolayers. Angewandte Chemie International Edition, 56(40), 12122–12126. doi:10.1002/anie.201705518
11. Song, P., Guerin, S., Tan, S. J., Annadata, H. V., Yu, X., Scully, M., … Nijhuis, C. A. (2018). Molecular diodes: Stable molecular diodes based on π–π interactions of the molecular frontier orbitals with graphene electrodes (adv. mater. 10/2018). Advanced Materials, 30(10). doi:10.1002/adma.201870069
12. Long, B., Manning, M., Burke, M., Szafranek, B. N., Visimberga, G., Thompson, D., … Quinn, A. J. (2011). Non-covalent functionalization of graphene using self-assembly of alkane-amines. Advanced Functional Materials, 22(4), 717–725. doi:10.1002/adfm.201101956
13. Song, P., Sangeeth, C. S., Thompson, D., Du, W., Loh, K. P., & Nijhuis, C. A. (2015). Noncovalent self-assembled monolayers on graphene as a highly stable platform for Molecular Tunnel junctions. Advanced Materials, 28(4), 631–639. doi:10.1002/adma.201504207
14. Park, S., Kim, H. R., Kim, J., Hong, B., & Yoon, H. J. (2021). Enhanced thermopower of saturated molecules by noncovalent anchor-induced electron doping of single-layer graphene electrode. Advanced Materials, 33(41). doi:10.1002/adma.202103177
15. Son, J. Y., & Song, H. (2022). Investigation of intrinsic charge transport via alkyl thiol molecular electronic junctions with conductive probe atomic force microscopy. Journal of Materials Science: Materials in Electronics, 33(17), 13568–13573. doi:10.1007/s10854-022-08291-w

16. Wold, D. J., & Frisbie, C. D. (2001). Fabrication and characterization of metal−molecule−metal junctions by conducting Probe Atomic Force Microscopy. Journal of the American Chemical Society, 123(23), 5549–5556. doi:10.1021/ja0101532
17. Park, S., Cho, N., & Yoon, H. J. (2019). Two different length-dependent regimes in thermoelectric large-area junctions of n-alkanethiolates. Chemistry of Materials, 31(15), 5973–5980. doi:10.1021/acs.chemmater.9b02461
18. Cui, L., Miao, R., Jiang, C., Meyhofer, E., & Reddy, P. (2017). Perspective: Thermal and thermoelectric transport in molecular junctions. The Journal of Chemical Physics, 146(9). doi:10.1063/1.4976982
19. O'Driscoll, L. J., Wang, X., Jay, M., Batsanov, A. S., Sadeghi, H., Lambert, C. J., … Bryce, M. R. (2019). Carbazole-based tetrapodal anchor groups for gold surfaces: Synthesis and conductance properties. Angewandte Chemie International Edition, 59(2), 882–889. doi:10.1002/anie.201911652
20. Wei, Z., Wang, X., Borges, A., Santella, M., Li, T., Sørensen, J. K., … Laursen, B. W. (2014). Triazatriangulene as binding group for Molecular Electronics. Langmuir, 30(49), 14868–14876. doi:10.1021/la504056v
21. Schwarz, F., & Lörtscher, E. (2014). Break-junctions for investigating transport at the molecular scale. Journal of Physics: Condensed Matter, 26(47), 474201. doi:10.1088/0953-8984/26/47/474201
22. Kim, T., Vázquez, H., Hybertsen, M. S., & Venkataraman, L. (2013). Conductance of molecular junctions formed with silver electrodes. Nano Letters, 13(7), 3358–3364. doi:10.1021/nl401654s

23. García-Suárez, V. M., Rocha, A. R., Bailey, S. W., Lambert, C. J., Sanvito, S., & Ferrer, J. (2005). Single-channel conductance of. Physical Review B, 72(4). doi:10.1103/physrevb.72.045437
24. Cuevas, J. C., & Scheer, E. (2010a). Molecular electronics. World Scientific Series in Nanoscience and Nanotechnology. doi:10.1142/7434
25. Tan, Z., Zhang, D., Tian, H.-R., Wu, Q., Hou, S., Pi, J., … Hong, W. (2019). Atomically defined Angstrom-scale all-carbon junctions. Nature Communications, 10(1). doi:10.1038/s41467-019-09793-8
26. Zheng, X. H., Zhang, G. R., Zeng, Z., García-Suárez, V. M., & Lambert, C. J. (2009). Effects of antidots on the transport properties of graphene nanoribbons. Physical Review B, 80(7). doi:10.1103/physrevb.80.075413
27. Gehring, P., Sowa, J. K., Cremers, J., Wu, Q., Sadeghi, H., Sheng, Y., … Mol, J. A. (2017). Distinguishing lead and molecule states in graphene-based single-electron transistors. ACS Nano, 11(6), 5325–5331. doi:10.1021/acsnano.7b00570
28. Bailey, S., Visontai, D., Lambert, C. J., Bryce, M. R., Frampton, H., & Chappell, D. (2014). A study of planar anchor groups for graphene-based single-molecule electronics. The Journal of Chemical Physics, 140(5). doi:10.1063/1.4861941
29. Ashwell, G. J., Phillips, L. J., Robinson, B. J., Urasinska-Wojcik, B., Lambert, C. J., Grace, I. M., … Ray, S. (2010). Molecular bridging of silicon nanogaps. ACS Nano, 4(12), 7401–7406. doi:10.1021/nn102460z
30. Reddy, P., Jang, S.-Y., Segalman, R. A., & Majumdar, A. (2007). Thermoelectricity in molecular junctions. Science, 315(5818), 1568–1571. doi:10.1126/science.1137149
31. Bergfield, J. P., & Stafford, C. A. (2009). Thermoelectric signatures of coherent transport in single-molecule heterojunctions. Nano Letters, 9(8), 3072–3076. doi:10.1021/nl901554s

32. Li, Y.-S., & Wang, X.-F. (2018). Manipulation of the magnetoresistance effect in a double-helix DNA. Journal of Physics: Condensed Matter, 30(45), 455102. doi:10.1088/1361-648x/aae567
33. Xiong, Z. H., Wu, D., Valy Vardeny, Z., & Shi, J. (2004). Giant magnetoresistance in organic spin-valves. Nature, 427(6977), 821–824. doi:10.1038/nature02325
34. Göhler, B., Hamelbeck, V., Markus, T. Z., Kettner, M., Hanne, G. F., Vager, Z., … Zacharias, H. (2011a). Spin selectivity in electron transmission through self-assembled monolayers of double-stranded DNA. Science, 331(6019), 894–897. doi:10.1126/science.1199339
35. Göhler, B., Hamelbeck, V., Markus, T. Z., Kettner, M., Hanne, G. F., Vager, Z., … Zacharias, H. (2011a). Spin selectivity in electron transmission through self-assembled monolayers of double-stranded DNA. Science, 331(6019), 894–897. doi:10.1126/science.1199339
36. Ferreira, Q., Bragança, A. M., Alcácer, L., & Morgado, J. (2014). Conductance of well-defined porphyrin self-assembled molecular wires up to 14 nm in length. The Journal of Physical Chemistry C, 118(13), 7229–7234. doi:10.1021/jp501122n
37. Long, B., Manning, M., Burke, M., Szafranek, B. N., Visimberga, G., Thompson, D., … Quinn, A. J. (2011a). Non-covalent functionalization of graphene using self-assembly of alkane-amines. Advanced Functional Materials, 22(4), 717–725. doi:10.1002/adfm.201101956
38. Song, P., Sangeeth, C. S., Thompson, D., Du, W., Loh, K. P., & Nijhuis, C. A. (2015a). Noncovalent self-assembled monolayers on graphene as a highly stable platform for Molecular Tunnel junctions. Advanced Materials, 28(4), 631–639. doi:10.1002/adma.201504207

39. Chiechi, R. C., Weiss, E. A., Dickey, M. D., & Whitesides, G. M. (2007). Eutectic gallium–indium (egain): A Moldable Liquid Metal for electrical characterization of self-assembled monolayers. Angewandte Chemie International Edition, 47(1), 142–144. doi:10.1002/anie.200703642
40. Sangeeth, C. S., Wan, A., & Nijhuis, C. A. (2014). Equivalent circuits of a self-assembled monolayer-based tunnel junction determined by impedance spectroscopy. Journal of the American Chemical Society, 136(31), 11134–11144. doi:10.1021/ja505420c
41. Carlotti, M., Soni, S., Kumar, S., Ai, Y., Sauter, E., Zharnikov, M., & Chiechi, R. C. (2018). Two-terminal molecular memory through reversible switching of quantum interference features in tunneling junctions. Angewandte Chemie International Edition, 57(48), 15681–15685. doi:10.1002/anie.201807879
42. Nerngchamnong, N., Yuan, L., Qi, D.-C., Li, J., Thompson, D., & Nijhuis, C. A. (2013). The role of van der waals forces in the performance of molecular diodes. Nature Nanotechnology, 8(2), 113–118. doi:10.1038/nnano.2012.238
43. Ismael, A., Al-Jobory, A., Wang, X., Alshehab, A., Almutlg, A., Alshammari, M., … Lambert, C. (2020a). Molecular-scale thermoelectricity: As simple as ‘ABC.’ Nanoscale Advances, 2(11), 5329–5334. doi:10.1039/d0na00772b
44. Wang, X., Ismael, A., Alanazi, B., Al-Jobory, A., Wang, J., & Lambert, C. J. (2023). High seebeck coefficient from isolated oligo-phenyl arrays on single layered graphene via stepwise assembly. Journal of Materials Chemistry C, 11(42), 14652–14660. doi:10.1039/d3tc02842a

# Chapter 6

## Conclusion and Future Work

### 6.1 Conclusion

To increase the effectiveness of thermoelectric devices, this thesis concentrated on electron transport theory in molecular-scale quantum devices and experimental modeling to investigate the electronic structure of diverse molecules. Blocks perform other device functions when connected to metal electrodes and create a nanoscale circuit.

This thesis has presented a series of studies into the electronic and thermoelectric properties of molecular junctions from metallo-porphyrins and a large set of symmetric and asymmetric molecules.

Chapter 2 explains the fundamental ideas behind the DFT algorithm SIESTA, which is used for all calculations of electronic structure. In order to calculate their transport properties, I connected these isolated molecules to metallic or graphene electrodes after extracting the Hamiltonian of the isolated molecule and relaxing it.

Chapter 3 presents the underlying concepts about transport theory, including the Landaur formula, thermoelectric coefficients, and scattering theory, and the Gollum implementation of Green's function methods.

In Chapter 4, I presented a study of the electron transport properties of the single-molecule/bilayer molecular junctions, formed from Zinc Tetraphenyl Porphyrin (ZnTPP), small graphene-like molecules (Gr), three derivatives with pyridine backbones, and three alkyl-chain backbones terminated with asymmetric anchor groups: amine ($NH_2$), and a direct carbon ($CH_2$) bond. In the first step, I investigated their electronic structure properties by computing their molecular orbitals. I then computed their optimised geometries and binding energies to

find the optimum separation distance between the molecule and the gold electrode, Next, I computed their electrical and Seebeck properties and compared theoretical calculations to experimental data using an EGaIn top contact. The transmission coefficient and the Seebeck coefficient of studied molecules did not agree with the measurements, so in

Chapter 5, based on the same core molecules, junctions with asymmetric electrodes were studied. In these calculations, to model junctions with asymmetric electrodes, molecules were sandwiched between gold and a single-layer graphene sheet (SLG). First, I calculated the binding energy to find the optimum distance between the graphene substrate and different anchor groups such as ZnTTP, and $NH_2$. By examining asymmetric single-molecule/bilayer junctions, I obtained much better agreement with experiment. I found that the graphene-like molecule is LUMO-dominated with negative S, while the rest of the studied molecules are HOMO-dominated with positive S. The Seebeck coefficient of the multi-component junction was higher than the Seebeck of most reported molecular junctions (> 50 μV/K); These suggest a new approach to producing high thermoelectric performance materials based on asymmetry.

## 6.2 Future Work

In this thesis, I have highlighted the Seebeck coefficient and electrical conductivity for asymmetric alkyl chains, pyridine derivatives and Zinc Tetraphenyl Porphyrin (ZnTPP), which these molecules are sandwiched to gold/gold and gold/graphene electrodes. In future work, it is interesting to look at how calculations change when different metals like superconducting electrodes at low temperatures [1] platinum, palladium [2-3], and iron [4] are used in place of gold/graphene leads or combinations of electrode materials [5]. Furthermore, since the control of heat across solids and solid-molecule interfaces is of importance for the thermal management of nanoscale devices and for improving the performance of thermoelectric materials, it would be interesting to investigate the connectivity dependence of phonon transport [6-7]. Due to the possible uses in thermal devices, phonon transport parameters in three-terminal systems have recently attracted increased attention [8]. Therefore, it would be worthwhile to use techniques for calculating phonon transport via asymmetric-terminal systems in order to determine how much phonons contribute to thermal conductance. In addition, it may be beneficial to look into the spin transport in the presence of ferromagnetic electrodes and a combination of ferromagnetic and superconducting electrodes. In the latter, resonant transport [9] and novel interference effects [10] can also take place, associated with Andreev scattering at the superconducting boundary [11], which would be superposed onto single molecule interference features.

Finally, it would be interesting to explore the theoretical simulations when using different molecules such as anthracene molecules attached to a Porphyrin or graphene sheet.

## 6.3 Bibliography


1. Hui, V. C., & Lambert, C. J. (1993). Andreev scattering, universal conductance fluctuations and Phase Periodic Transport. Europhysics Letters (EPL), 23(3), 203–209. doi:10.1209/0295-5075/23/3/008
2. García-Suárez, V. M., Rocha, A. R., Bailey, S. W., Lambert, C. J., Sanvito, S., & Ferrer, J. (2005). Conductance oscillations in zigzag platinum chains Physical Review Letters, 95 256804. DOI: 10.1103/PhysRevLett.95.256804
3. Smit, R. H., Noat, Y., Untiedt, C., Lang, N. D., van Hemert, M. C., & van Ruitenbeek, J. M. (2002). Measurement of the conductance of a hydrogen molecule. Nature, 419(6910), 906–909. doi:10.1038/nature01103
4. García-Suárez, V. M., Newman, C. M., Lambert, C. J., Pruneda, J. M., & Ferrer, J. (2004). Optimized basis sets for the collinear and non-collinear phases of Iron. Journal of Physics: Condensed Matter, 16(30), 5453–5459. doi:10.1088/0953-8984/16/30/008
5. Zólyomi, V., Rusznyák, Kürti, J., & Lambert, C. J. (2010). First Principles Study of the binding of 4d and 5d transition metals to graphene. The Journal of Physical Chemistry C, 114(43), 18548–18552. doi:10.1021/jp107669b
6. Kambili, A., Fagas, G., Fal'ko, V. I., & Lambert, C. J. (1999). Phonon-mediated thermal conductance of mesoscopic wires with rough edges. Physical Review B, 60(23), 15593–15596. doi:10.1103/physrevb.60.15593

7. Fagas, G., Kozorezov, A. G., Lambert, C. J., Wigmore, J. K., Peacock, A., Poelaert, A., & den Hartog, R. (1999). Lattice Dynamics of a disordered solid-solid interface. Physical Review B, 60(9), 6459–6464. doi:10.1103/physrevb.60.6459
8. Zhang, L., Wang, J.-S., & Li, B. (2010). Ballistic thermal rectification in nanoscale three-terminal junctions. Physical Review B, 81(10). doi:10.1103/physrevb.81.100301
9. N.R. Claughton, M. Leadbeater, C.J. Lambert (1995). Theory of Andreev resonances in quantum dots. Journal of Physics: Condensed Matter 7 (46), 8757. DOI 10.1088/0953-8984/7/46/007
10. C.J. Lambert (1993). Quantum Interference from superconducting islands in a mesoscopic solid. J. Phys. Condens. Matter 5, 707. DOI 10.1088/0953-8984/5/6/007
11. C.J. Lambert, R Raimondi, V Sweeney, AF Volkov (1997). Boundary conditions for quasiclassical equations in the theory of superconductivity. Physical Review B 55 (9), 6015. DOI:https://doi.org/10.1103/PhysRevB.55.6015